TECHNISCHE UNIVERSITÄT WIEN

ATOMINSTITUT

DIPLOMARBEIT

Charakterisierung der Magnetfalle des CREScent Experiments

zur Erlangung des akademischen Grades

Diplom-Ingenieur

im Rahmen des Studiums

Masterstudium Technische Physik UE 066 461

eingereicht von **Daniel Paulitsch, BSc**

Matrikelnummer: 01427692

ausgeführt am Atominstitut
der Fakultät für Physik der Technischen Universität Wien
Juni 2023

unter der Anleitung von
Univ.Prof. Dipl.-Phys. Dr.rer.nat. Hartmut Abele,
Projektass. Dr.rer.nat. Irina Pradler und
Projektass. Dipl.-Ing. Andreas Doblhammer

Wien, 14.06.2023 _____ _____

(Unterschrift Verfasser) (Unterschrift Betreuer/in)

TECHNISCHE
UNIVERSITÄT
WIEN
Vienna University of Technology

ATOMINSTITUT

Master's Thesis

Magnetic Trap Characterization of the CREScent Experiment

Daniel Paulitsch, BSc
Matriculation Number: 01427692

carried out at the Atominstitut
of the Vienna University of Technology
June 2023

under the guidance of
Univ.Prof. Dipl.-Phys. Dr.rer.nat. Hartmut Abele,
Projektass. Dr.rer.nat. Irina Pradler and
Projektass. Dipl.-Ing. Andreas Doblhammer

Abstract

The CREScent experiment aims to provide a novel approach to electron spectroscopy based on a frequency measurement of the emitted electromagnetic radiation. The experiment operates on the principle that electrons gyrating in a uniform magnetic field emit cyclotron radiation, and the frequency of this radiation is proportional to the energy of the electron (30-600 keV). The technique is commonly known as Cyclotron Radiation Emission Spectroscopy (CRES). In order to measure the emitted electromagnetic radiation accurately the signal has to be of sufficient length (timescale of ms). To increase signal duration a magnetic trap which confines the electrons in the central region of high magnetic field was constructed.

The aim of this work was to characterize the effectiveness of this magnetic trap by measuring the number of electrons that escape the magnetic trap. A scintillation based measurement setup was used to detect the electrons. Measurements at different trap coil currents were taken. The results show that the magnetic trap was effective in confining electrons. Furthermore, a higher current in the trap coils and thus deeper magnetic trap confined more electrons. It was verified that at low enough electron/gamma energies, the energy/channel relationship of the scintillation based measurement setup is linear. It was also explored how the magnetic field influences the detector and the resulting spectrum was modeled.

Kurzfassung

Das CREScent-Experiment soll einen neuartigen Ansatz für die Elektronenspektroskopie bieten. Der Ansatz basiert auf einer Frequenzmessung der emittierten elektromagnetischen Strahlung. Das Experiment basiert auf dem Prinzip, dass Elektronen, die sich in einem uniformen Magnetfeld bewegen, Zyklotronstrahlung aussenden und die Frequenz dieser Strahlung proportional zur Energie des Elektrons (30–600 keV) ist. Die Methode ist allgemein bekannt als Cyclotron Radiation Emission Spectroscopy (CRES). Um die emittierte elektromagnetische Strahlung genau messen zu können, muss das Signal eine ausreichende zeitliche Länge haben (Größenordnung von ms). Um die Signaldauer zu verlängern, wurde eine Magnetfalle konstruiert, die die Elektronen im zentralen Bereich des starken Magnetfelds einschließt.

Ziel dieser Arbeit war es, die Wirksamkeit dieser Magnetfalle zu charakterisieren, indem die Anzahl der Elektronen gemessen wurde, die der Magnetfalle entkommen. Zum Nachweis der Elektronen wurde ein szintillationsbasierter Messaufbau verwendet. Es wurden Messungen bei verschiedenen Strömen in den Fallenspulen durchgeführt. Die Ergebnisse zeigen, dass die Magnetfalle die Elektronen effektiv einschließt. Darüber hinaus hält ein höherer Strom in den Fallenspulen und eine damit tiefere Magnetfalle mehr Elektronen fest. Es wurde verifiziert, dass bei ausreichend niedrigen Elektronen/Gammaenergien die Energie/Kanal-Beziehung des Szintillations basierten Messaufbaus linear ist. Außerdem wurde untersucht, wie das Magnetfeld den Detektor beeinflusst und das resultierende Spektrum wurde modelliert.

Contents

1 Introduction to CREScent

In recent experiments trying to measure electron energies from beta decay, the technique most commonly used were MAC-E-Filters (Magnetic Adiabatic Collimation combined with an Electrostatic Filter). These measure electron energy by first transforming the isotropically emitted electrons into a broad beam of electrons flying almost parallel to the magnetic field lines. The electrons start in a region of maximum magnetic field and then travel towards the minimum magnetic field region where they reach roughly longitudinal motion. Then only electrons that can pass an electrostatic barrier are reaccelerated and collimated onto a detector. MAC-E-Filters have a fundamental limit in energy resolution which is determined by the ratio of the maximum and minimum magnetic field regions.

$$\frac{\triangle E}{E} = \frac{B_{min}}{B_{max}} \tag{1}$$

This limit has more or less been reached in the ongoing KATRIN experiment which aims to give an upper limit on the mass of the neutrino. The experiment has a sensitivity of 0.20 eV at 90% confidence [1]. If the neutrino mass is much below 0.20 eV, it is difficult to envision any spectrometer based on the same construction (MAC-E) being able to access it [2].

The technique known as Cyclotron Radiation Emission Spectroscopy (CRES) has recently been proposed to measure the energies of charged electrons gyrating in a magnetic field [3]. It has the potential to go below the limit of classic MAC-E filter spectrometers. The method is non-destructive, it allows the electrons to remain in flight, with their kinetic energy remaining nearly unaffected. The exact dependence of the radiated frequency ω in relation to the magnetic field B, the electron mass m_e and the energy E_{kin} of the electron is presented in eq. (2),

$$\omega = \frac{e\ B}{\gamma\ m_e} = \frac{\omega_c}{\gamma} = \frac{\omega_c}{1 + \frac{E_{kin}}{mc^2}} \tag{2}$$

where e is the elementary charge, c is the speed of light, γ the electron Lorentz factor $\gamma = 1 + \frac{E_{kin}}{m_e c^2}$ and m is the mass of the particle. The radiated frequency is proportional to the magnetic field; therefore it is necessary to have a homogeneous and precisely measured magnetic field. All aspects of characterizing and homogenizing the magnetic field are discussed in [4].

1.1 CREScent Beta-frequency Experiment

The experiment which aims to measure these CRES-type events at the TU Wien Atominstitut is called CREScent which stands for Cyclotron Radiation Emission Spectroscopy type Cavity Electron eNergy deTector. The CREScent-Experiment is developed within the framework of the PERC-Collaboration. It is a proof-of-principle experiment and the long term goal of the experiment is to be incorporated into the proton and electron radiation channel (PERC) experiment as an electron spectrometer. The PERC experiment is designed for high-precision measurements of angular correlation coefficients of the neutron beta-decay [5]. It will serve as an intense and clean source of electrons and protons [6]. Obtaining more precise measurements of the decay products of neutron beta decay might shine light on new fundamental principles in particle physics.

CREScent operates on the principle that charged particles, when traveling within a static and uniform magnetic field, will travel in a spiral like path, also described as cyclotron motion. During this circular motion the electrons experience acceleration which results in the emission of electromagnetic radiation. This electromagnetic radiation is known as cyclotron or synchrotron radiation. For moderately relativistic particles the frequency of cyclotron radiation is directly proportional to the energy. The charged particles in the CREScent experiment are electrons that are emitted by the decay of conversion electron sources like for example ^{207}Bi or ^{109}Cd.

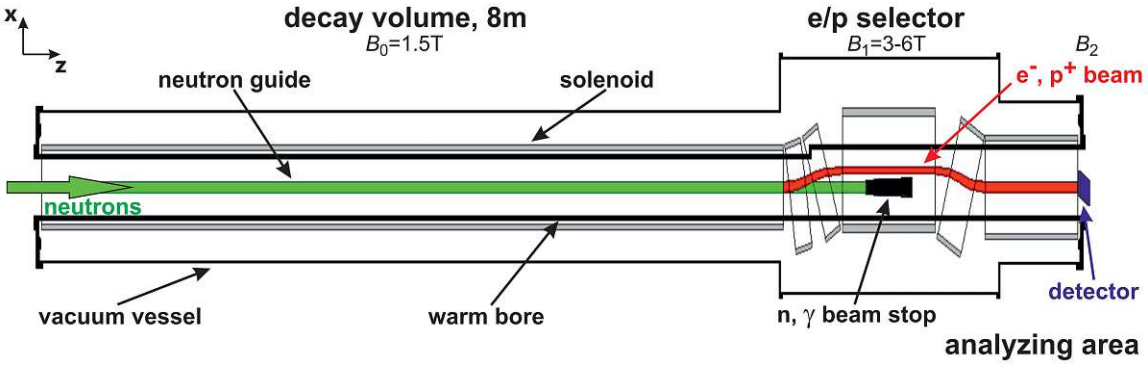

Figure 3: The PERC experiment. Cold neutrons (green) pass through the decay volume where a small fraction decays. The decay products (red) are guided by the magnetic field from the superconducting coils (gray) towards the detector (blue) [7]. PERC is being built in collaboration with the Universities of Heidelberg and Mainz, the Technical University of Munich, the Vienna University of Technology and the Institut Laue-Langevin, Grenoble.

1.1.1 Magnetic Trap

The Nyquist–Shannon sampling theorem states that in order to accurately determine the maximum frequency in a signal, a minimum sampling rate of two times the maximum frequency is necessary. The electron has to emit a long enough signal to accommodate enough samples. Furthermore, when signals are only slightly more intense than the background noise, it is easier to differentiate the signal from the noise if the signal is longer. To measure any emitted electromagnetic radiation by the electrons it is necessary to have a signal of detectable length (in the order of ms). A longer observation time leads to an increased frequency resolution and thus the energy resolution increases [8].

To achieve a longer signal, two magnetic mirrors forming a magnetic trap are utilized. The resulting magnetic field can be seen in fig. 1. Essentially it consists of two additional axial humps in the magnetic field. The trap confines the electrons in the central region of high magnetic field, allowing for a longer residing time in the magnetic field. Confining electrons with an electric field trap is not practical since it would introduce a position-dependent component to the electron energy [9]. A purely magnetic trap which is also known as no work trap is used. Within a purely magnetic field the force is always perpendicular to the electron velocity, therefore the kinetic energy cannot change. The magnetic mirror effect is only dependent on the depth of the trap and the pitch angle, not on the mass or velocity of the charged particle.

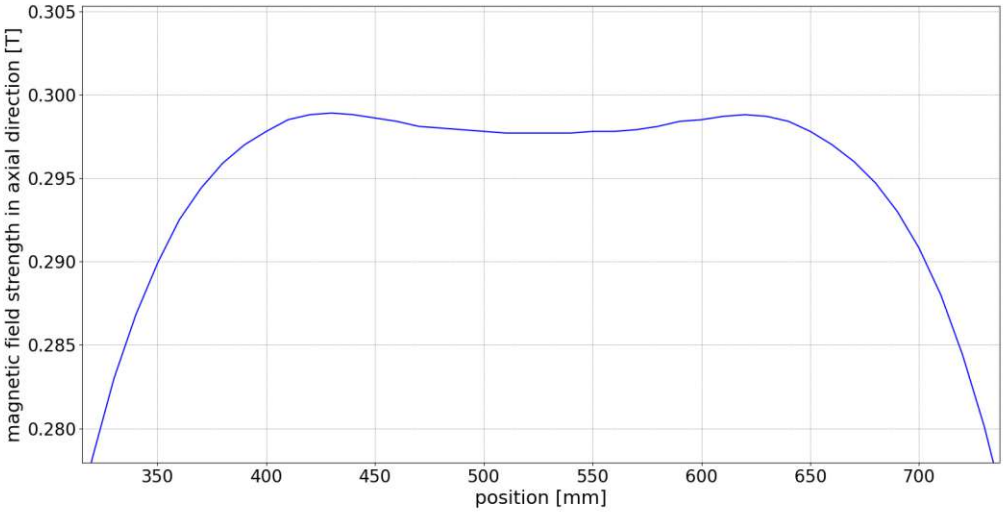

Figure 1: The axial magnetic field component in the bore of the superconducting 4.7 T magnet, measured with a Bell 6010 Hall Effect Gaussmeter. The position axis denotes the position along the z-axis. This measurement was taken at the xy-position in the very center. The trap has a depth of 1.2 mT at a background field of 297.7 mT. The trap field coils are positioned 20.5 cm apart. The background field weakens considerably outside the trapping volume.

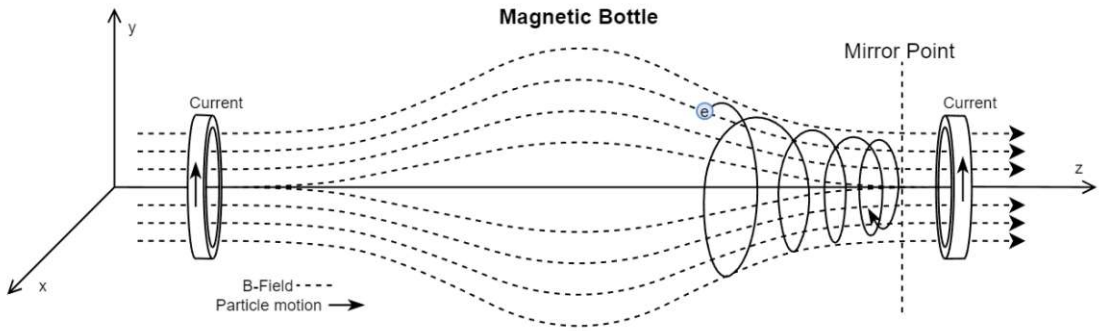

Figure 2: A depiction of the magnetic field lines within a magnetic bottle trap and the path that particles follow. As particles reach the mirror point, their longitudinal velocity is reversed and they are reflected. [10]

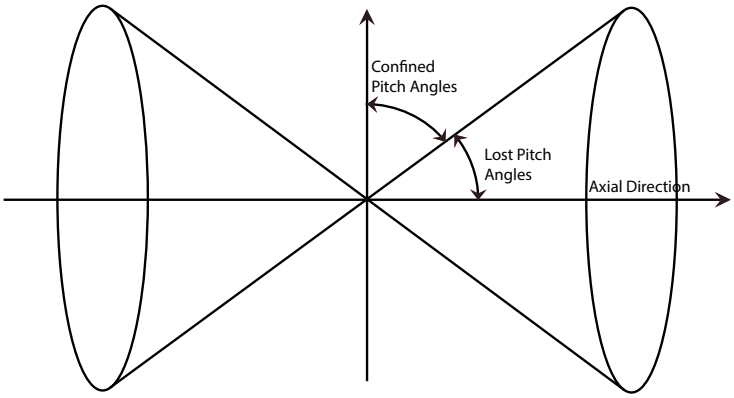

Figure 3: Every charged particle that is inside the cone of the lost pitch angles is not confined. Only electrons that have for example (at a field strength of 297.7 mT and a trap depth of 1.2 mT) a pitch angle greater than 86.37 degrees in the center will be confined by the trap.

When charged particles travel in a magnetic field the path is determined by the Lorentz force. Charged particles in a magnetic field will follow a spiral-like path, given that the particle has orthogonal velocity vector components in relation to the magnetic field vector. If a gyrating particle enters a stronger field region, it will lose longitudinal momentum which is transferred into its transverse momentum. If the magnetic field increase is strong enough, the particle moves back into the weaker field region. This deflection does not result in energy loss as the magnetic field does not perform any work. Alternatively the fact that charged particles are reflected on a magnetic mirror can be derived from the conservation of magnetic moment and kinetic energy. Electrons are only confined within the magnetic mirror if they have a pitch angle greater than a certain value.

1.1.2 Pitch Angle

If an isotropically emitting point source in the magnetic field is assumed, some electrons will have a velocity vector parallel to the axial magnetic field. These electrons will fly straight without being trapped or influenced by any magnetic field. The other extremum would be that there is no axial component of the electron velocity, in this case the electron trajectory will be a circle. A pitch angle θ can be defined to describe the behavior of the electrons between these two extremes. The pitch angle is the angle between the local magnetic field and the velocity vector. Since the system is symmetric, only pitch angles between zero degrees and 90 degrees are considered. Equation (3) gives a boundary for the minimum pitch angle θ of charged particles still confined in the magnetic bottle depending on the trap depth ΔB and the maximum magnetic field B_{max}.

$$\theta \geq \arcsin\left(\sqrt{1 - \frac{\Delta B}{B_{max}}}\right) \tag{3}$$

Since the position and velocity vector change over time, the pitch angle also changes. For confined electrons the pitch angle is 90 degrees at the turnaround points. At a field strength of 297.7 mT and a trap depth of 1.2 mT as seen in figure 1, charged particles with a pitch angle greater than 86.37 degrees in the center will be confined by the trap. The trap depth depends on the position within the xy-plane, as can be seen in fig. 42, the trap field increases with increasing radius. As a first approximation the electrons start from a centered point source and have a gyration radius of less than 1 cm. Therefore the approximation of using the central trap fields seems valid. In fig. 4 the magnetic field along the center is used to show the pitch angle as it changes with a varying magnetic field. It can be seen that only initial pitch angles above 86 degrees reach a pitch angle of 90 degrees. The trap field in the measurement from fig. 4 is slightly stronger on the left side. This means a particle with an initial pitch angle of 86 degrees is reflected at the left but it can pass the right trap field.

Another important parameter of the gyrating electrons is their radius of gyration. The relativistic Larmor radius r_g is given in eq. (4),

$$r_g = \frac{\gamma\, m\, c\, \sin(\theta)}{e\, B} \tag{4}$$

where e is the elementary charge, c is the speed of light, B is the magnetic field, θ is the pitch angle, γ the electron Lorentz factor $\gamma = 1 + \frac{E_{kin}}{m_e c^2}$ and m is the mass of the particle.

1.1.3 Pitch Angle in Relation to the Magnetic Field

The kinetic energy of a particle in a magnetic field can be decomposed into a parallel and a perpendicular component. The term on the left in eq. (5) represents the full kinetic energy the middle term is the parallel and the right term the perpendicular energy.

$$\frac{p_0^2}{2\ m_e} = \frac{p_0^2\ (cos(\theta))^2}{2\ m_e} + \mu\ B \tag{5}$$

p_0 stands for the initial momentum, m_e the electron mass, θ the pitch angle, B the magnetic field in axial direction and μ is the equivalent magnetic moment of the electron.

$$\mu = \frac{p_0^2\ (sin(\theta_{initial}))^2}{2\ m_e\ B} \tag{6}$$

The electron equivalent magnetic moment μ is a constant of motion in cases where the change in magnetic field direction is slow compared to the cyclotron frequency.

Using μ as a constant eq. (5) can be transformed to eq. (7) leading to the pitch angle θ in dependence of the magnetic field B.

$$\theta = arccos\left(\sqrt{1 - \frac{2\ m\ \mu\ B}{p_0^2}}\right) \tag{7}$$

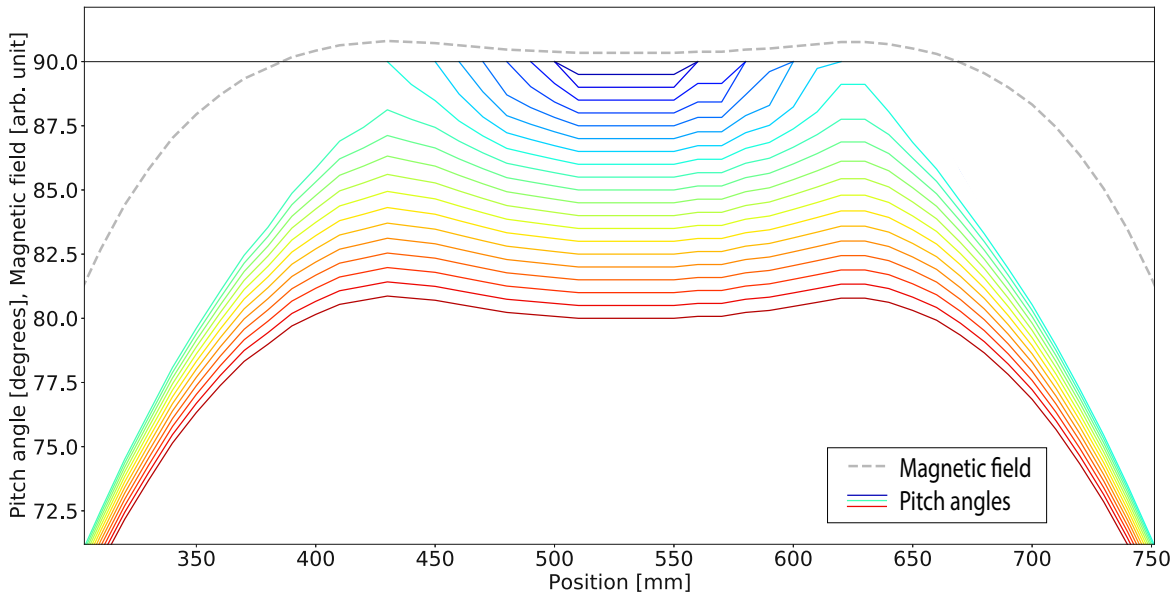

Figure 4: The pitch angle depending on the position in the magnetic field. 21 different starting pitch angles from 80 to 89.5 degrees of 482 keV electrons are shown. The evolution of a pitch angle depending on a measured magnetic field can be seen. If a particle reaches a pitch angle of 90 degrees it has no velocity in axial direction and is reflected. The magnetic field has a strength of 0.2151 T in the center and a trap field of 1.2 mT. The profile of the magnetic field is indicated by the gray dotted line. It was measured with a Bell 6010 Hall Effect Gaussmeter. The resolution limitations of Bell 6010 Hall Effect Gaussmeter and the fact that in axial direction a measurement was taken once, every centimeter results in the choppy pitch angle lines, especially at higher pitch angles. The formulas and relations used for the creation of this plot are mentioned in section 1.1.3.

1.1.4 The Emitted Electromagnetic Radiation

Electrons with an axial velocity vector component will travel between the two trap coils. They experience a higher field at the turnaround points, this results in a time-varying cyclotron frequency. Furthermore, the axial oscillation introduces a Doppler shift, this contribution is greater than the modulation experienced through the time-varying magnetic field. The frequency spectrum of the emitted radiation has multiple peaks (a comb structure). The central peak has the highest energy, the multiple side peaks have lower energy and may not always be detectable. The axial frequency can be obtained from the distance between peaks. The axial frequency or the related pitch angle is needed to determine the parallel and perpendicular energy component of the emitting particle. The complete description of the expected Cyclotron Radiation Emission can be seen in [9].

As the electrons emit electromagnetic radiation, the principle of energy conservation demands that the kinetic energy of the electrons decreases correspondingly. This increases the cyclotron frequency which can be seen in fig. 5. Whenever an electron scatters with a residual gas molecule in the chamber, the decrease of kinetic energy leads to a discontinuity in the cyclotron frequency. An example of the frequency over time can also be seen in fig. 5.

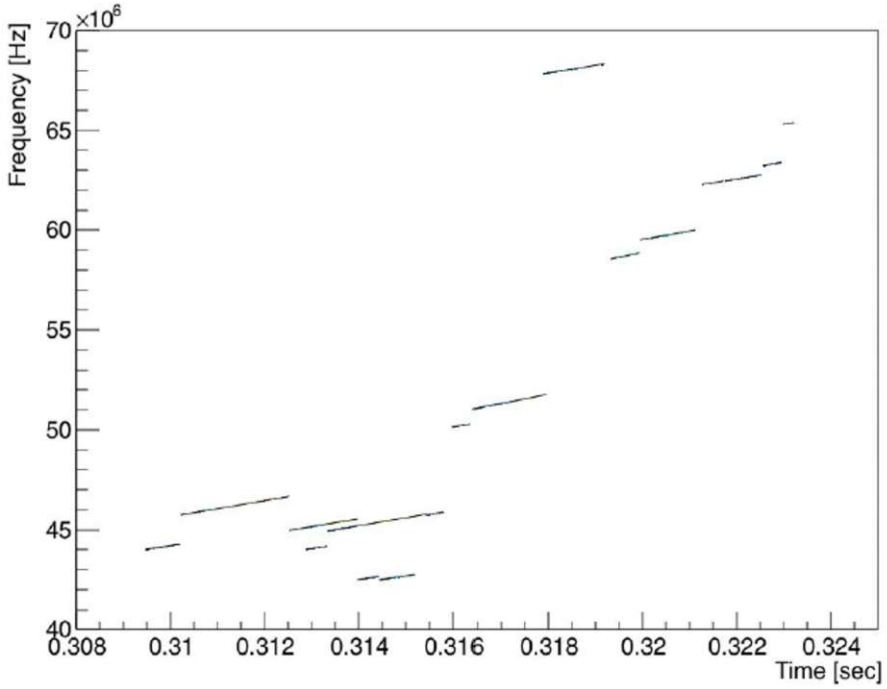

Figure 5: The measured frequency of multiple electrons over time. Each discontinuity in the cyclotron frequency corresponds to an interaction with a gas molecule. The gradual increase of the frequency is due to emission of electromagnetic radiation and energy conservation. Multiple electrons are measured whenever multiple lines are present at the same time [11].

1.1.5 The Power Emitted by a Gyrating Charged Particle

The power emitted by a gyrating charged particle P is given by eq. (8),

$$P = \frac{e^4}{6\,\pi\,\epsilon_0\,m^2\,c} B^2(\sin(\theta))^2(\gamma^2 - 1) \tag{8}$$

where ϵ_0 is the vacuum permittivity and θ is the pitch angle from eq. (3). For a 482 keV electron (see section 5.3) gyrating orthogonally in a 1T magnetic field, the emitted power would be $4.396\text{x}10^{-14}$ W or -103.5 dBm. This very weak signal is far below the minimal received wireless network power of -80 dBm (802.11 variants) signal power.

The emitted radiation causes a constant energy loss and thus frequency shift which has to be taken into account. For the given electron after for example one millisecond the energy loss would reduce the energy by 0.274 keV, the frequency of the electron would shift from 14.419 GHz to 14.424 GHz. In other words, the radiated frequency of the electron in question increases by 0.3984 MHz in the first millisecond. The power emitted by an electron is large enough to be detectable but not so large as to rapidly change the electron frequency [3].

2 Beta Decay and Free Neutron Decay

Beta decay is a nuclear decay process in which a nucleus undergoes a transformation by changing the number of protons or neutrons it contains. It is broadly categorized into two types: beta-minus (β^-) decay and beta-plus (β^+) decay. It is an example of the weak interaction, one of the four fundamental forces of nature. Beta decay occurs in nuclei that contain excess neutrons or protons, allowing them to achieve greater stability by transforming into a more balanced configuration.

In β^- decay, a neutron within the nucleus is converted into a proton, an electron, and an electron antineutrino. Charge and lepton number are conserved. This process can be represented by the following equation:

$$n \rightarrow p + e^- + \bar{\nu}_e$$

Here, n represents the neutron, p denotes the proton, $e-$ stands for the beta particle (electron), and $\bar{\nu}_e$ represents the electron antineutrino. The detailed process can be illustrated via a Feynman diagram in it a down quark is transformed to an up quark by a W boson, the W boson goes over to an electron and a $\bar{\nu}_e$. The free neutron decay is a specific instance of β^- decay it occurs when an isolated, unbound neutron not influenced by the strong nuclear force decays into a proton, an electron, and an $\bar{\nu}_e$.

β^+ decay, on the other hand, involves the conversion of a proton into a neutron, a positron, and an electron neutrino. The equation for β^+ decay is as follows:

$$p \rightarrow n + e^+ + \nu_e$$

In this equation ν_e denotes the electron neutrino. Electron capture is an alternative decay mode for isotopes that can decay via positron emission. If the energy difference between the parent atom and the daughter atom is less than 1.022 MeV, positron emission is not possible and thus electron capture is the sole decay mode.

2.1 Beta Decay Spectrum

The characteristic beta decay spectrum is briefly mentioned, fig. 6 is included to clarify the shape of this spectrum.

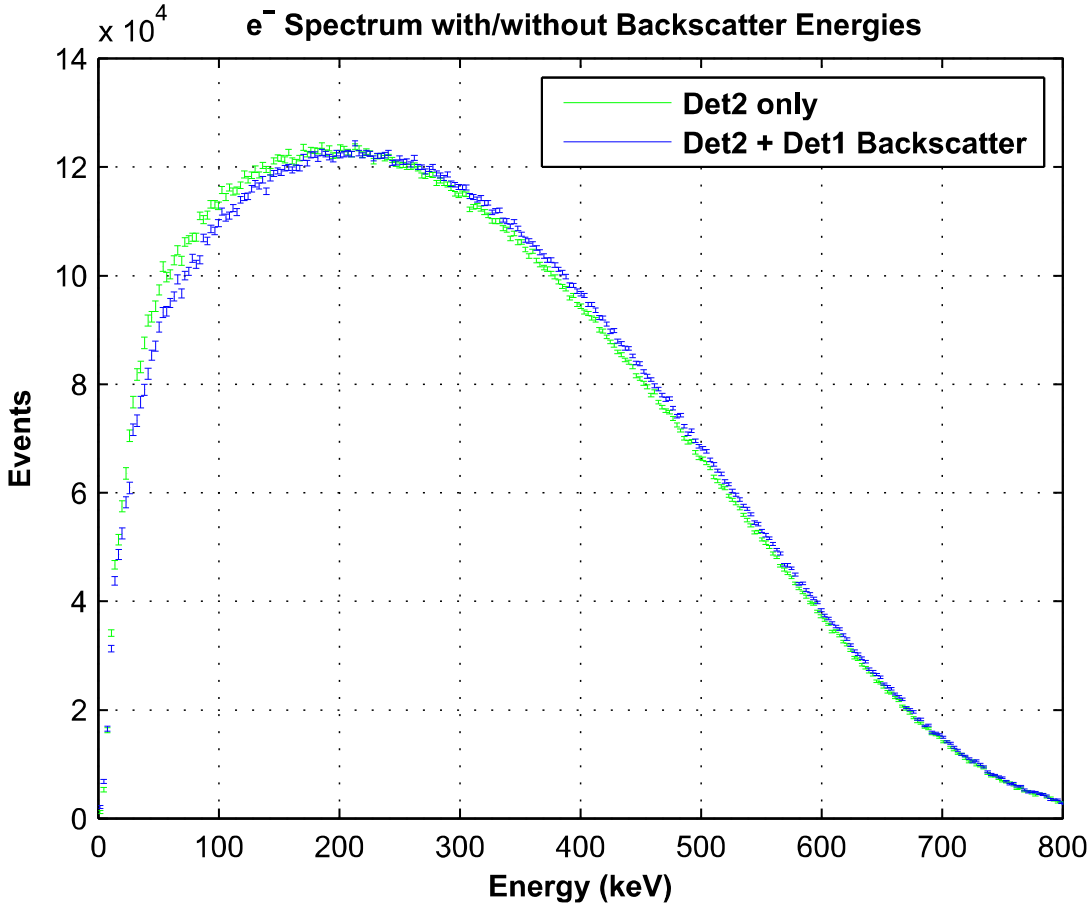

Figure 6: Example of a the β^- spectrum. This spectrum is a spectrum of the free neutron decay it was measured by the PERKEO III spectrometer (image from [12]). PERKEO III has a symmetric layout an electron can be backscattered from one detector and then be measured by the other detector. The green electron energy spectrum is measured by a single detector. The blue spectrum includes the backscatter energy contribution from the other detector.

3 Interactions of Ionizing Particles with Matter

When selecting a detector for ionizing radiation it is essential to be able to absorb energies up to the maximum relevant energy. If the goal is to measure the spectrum knowledge of the absorption mechanisms is necessary for the interpretation of a recorded spectra. In this work the two relevant types of ionizing radiation are beta particles and high energy photons up to 500 keV.

3.0.1 Interaction of Electrons and Positrons with Matter

High energy electrons or positrons interact with matter in multiple ways. The relative contributions of all processes are summarized in fig. 7.

Bremsstrahlung and ionization are the main contributions, excitation and Cerenkov Radiation are very minor contributions. A high velocity positron interacts in much the same way to an electron, however once it comes to rest and encounters an electron it annihilates to photons.

Inelastic scattering events can be divided into two categories: ionization and excitation. Ionization is the process in which a relativistic electron or charged particle interacts with a neutral atom and strips away an electron resulting in a positive ion and a secondary electron. The secondary electron has a kinetic energy of usually less than 100 eV. If the secondary electron has an energy high enough to ionize additional atoms it is referred to as a delta ray. For electrons large energy transfers to atomic electrons (binding energy can be neglected) are termed Møller scattering. For positrons the process is termed Bhabha scattering.

Excitation is a process in which a relativistic electron or charged particle interacts with an electron bound to an atom. Energy is transferred to the electron lifting it into a higher energy state - a higher shell. As opposed to ionization not enough energy is transferred to dissociate the electron from the atom. The process primarily occurs farther away from the main electron trajectory.

A low energy positron annihilates to two photons when meeting an electron. The process must satisfy a number of conservation laws like conservation of energy, momentum, charge and lepton number. Conservation of energy and momentum demand that two or more photons are created. The most probable end result is two photons each having an energy of 511 keV which is the rest mass of an electron or positron. In a reference frame without momentum before annihilation the two resulting photons would have opposite directions. An additional unlikely decay chain of positron electron annihilation can also produce one or more neutrino antineutrino pairs, however this is extremely unlikely (10^4 times less likely).

For higher energy electrons (in the range of 10 MeV) energy loss via bremsstrahlung begins to dominate over excitation/ionization. Bremsstrahlung arises from the principle that accelerating charges emit electromagnetic radiation. When an electron is deflected in the electric field from e.g. an atomic nucleus it experiences acceleration and thus emits electromagnetic radiation. Obeying conservation of energy, the lost kinetic energy is the energy of the photon. Bremsstrahlung photons can have arbitrary energy up to the energy of the incident particle. In matter the range of high energy electrons is largely a function of electron density per unit volume. To a lesser degree the range is a function of the atomic number.

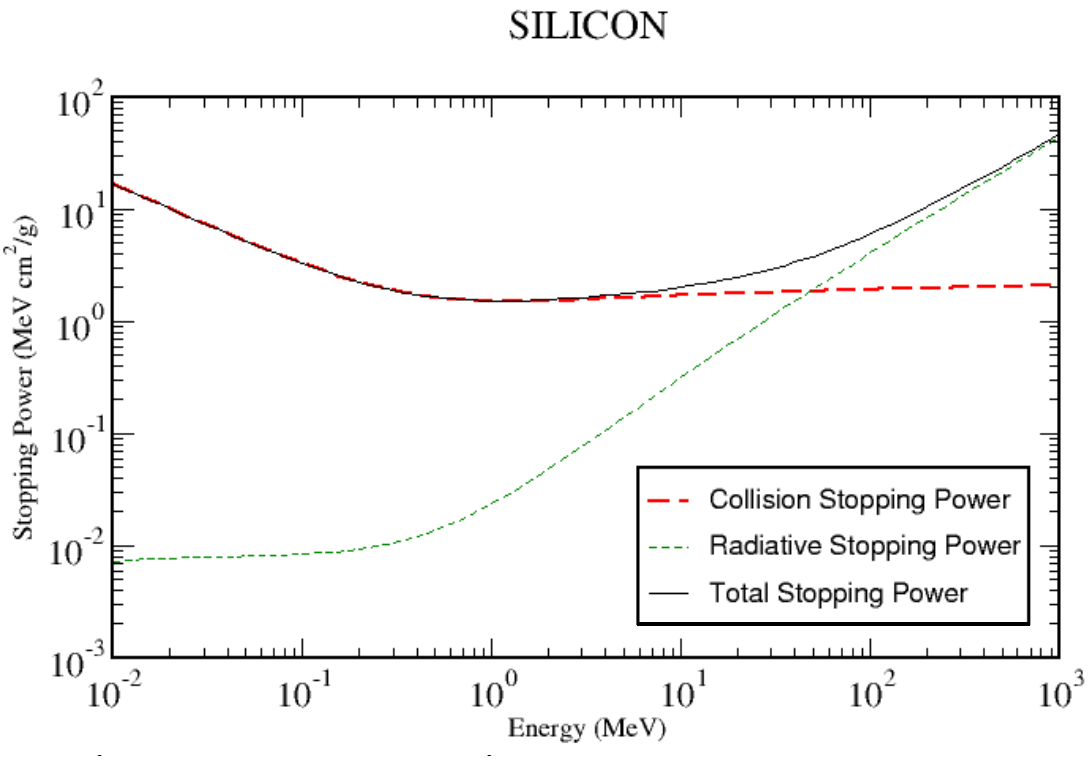

Figure 7: The stopping power of silicon it is numerically equal to the loss of energy per unit path length. The collision stopping power is the average rate of energy loss per unit path length, due to Coulomb collisions that result in the ionization and excitation of atoms. The radiative stopping power is the average rate of energy loss per unit path length due to collisions with atoms and atomic electrons in which bremsstrahlung quanta are emitted. And the total stopping power is the sum of the other two [13].

3.0.2 Electrons in Scintillation Crystals

Beta particles do not travel in straight lines when passing through matter as seen in fig. 8. Which means a beta particle may leave the detector.

To show the behaviors of electrons interacting with scintillation crystals like BGO and YSO simulations using the program CASINO Monte Carlo Software were created [14]. Casino is a program for the Monte Carlo simulation of electron trajectories in solids specifically created for for field emission scanning electron microscope at energies of (0.1 to 30) keV. Simulating higher energies is also possible. The electrons in the simulations are mono energetic and in a Gaussian-shaped beam with a radius of 10 nm (99.9% of the total distribution) and strike at a defined angle relative to the surface. CASINO groups the effects of inelastic scattering into a continuous energy loss function. This and all further assumptions and simplifications used by CASINO are described in [14].

The backscattering coefficient is defined as the ratio of electrons that leave the crystal (with an energy greater than 50 eV) to the total number of the incident electrons. At perpendicular incidence and for 975 keV electrons YSO has a backscattering coefficient of 0.108. The backscattering coefficient depends on the density of a material. The denser BGO has a higher backscattering coefficient of 0.25 at 975 keV and perpendicular incidence.

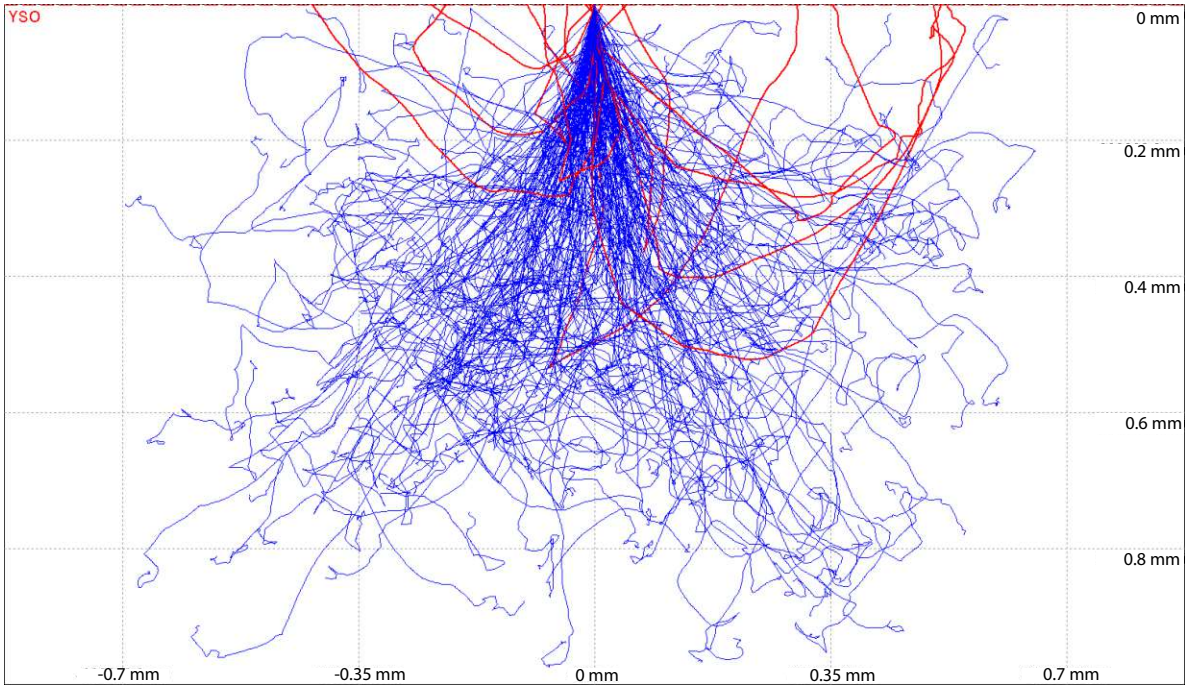

Figure 8: The paths of 200 electrons with an energy of 975 keV in YSO. As explained in section 3.0.1 the electrons travel in an erratic course. The red lines are paths of electrons that left the crystal - that backscattered. A track ends either at the minimum energy of 50 eV or after leaving the crystal. It can be seen that very few electrons travel below depths of 0.8 mm.

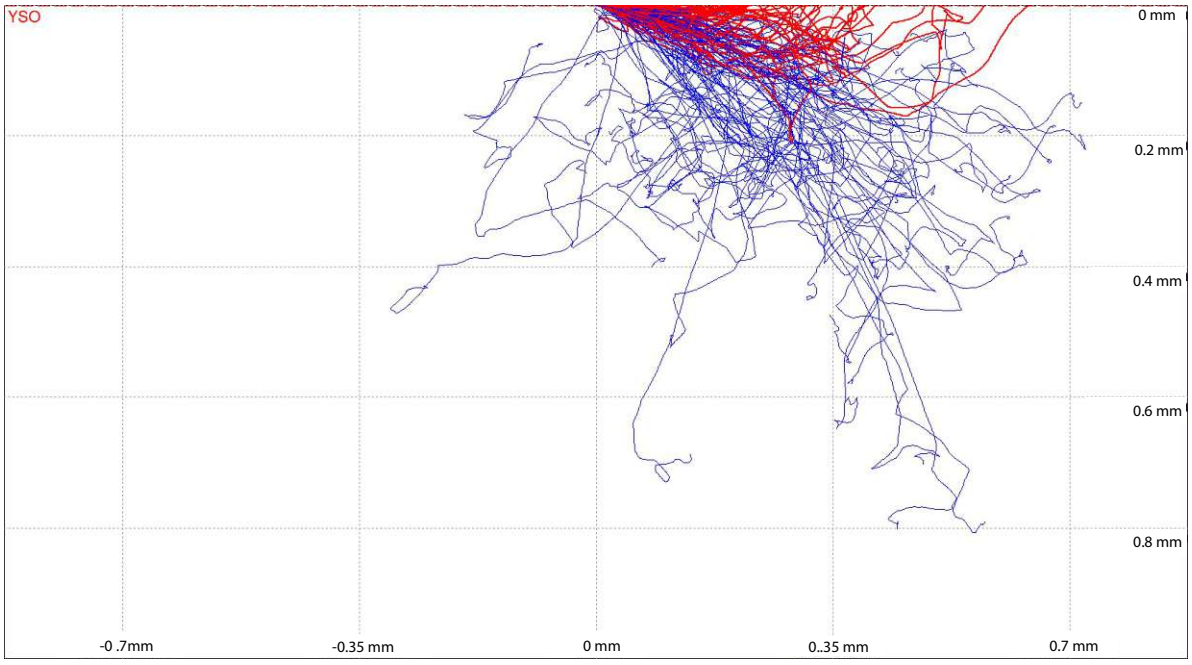

Figure 9: Again the paths of 200 electrons with an energy of 975 keV in YSO. The difference to the previous image is that the electrons enter the crystal at a shallow angle. The red lines are paths of electrons that left the crystal - that backscattered. A track ends either at the minimum energy of 50 eV or after leaving the crystal. It can be seen that a significantly higher fraction of the electrons leaves the crystal.

3.0.3 Interactions of Photons with Matter

Beta radiation is absorbed more easily than gamma radiation. Therefore, the limiting factor when choosing a suitable detector was the absorption of gamma radiation. When beta particles interact with matter they emit high energy photons as explained in the previous chapter. The interaction of gamma rays with matter can be attributed to three major effects.

- Photoelectric absorption
- Compton scattering
- Pair production

Each contribution varies with energy and the atomic number of the matter [15]. The total cross section at a specific energy is then the sum of all three contributions at that photon energy. The attenuation coefficient describes to what extent the radiant flux is reduced or attenuated as incoming flux passes through a specific material. A narrow beam of mono-energetic photons with an incident intensity I_0 and exiting intensity I traverses a layer of material with mass thickness x (defined as the mass per unit area) and density ρ. This process can be described by an exponential attenuation law eq. (9).

$$\frac{I}{I_0} = \exp\left(-\frac{\mu}{\rho}x\right) \tag{9}$$

eq. (9) can be rewritten as eq. (10).

$$\frac{\mu}{\rho} = \frac{ln\left(\frac{I}{I_0}\right)}{x} \tag{10}$$

$\frac{\mu}{\rho}$ is then the mass attenuation coefficient. The total cross section per atom σ_{tot} is related to the mass attenuation coefficient via eq. (11),

$$\frac{\mu}{\rho} = \frac{\sigma_{tot}}{uA} \tag{11}$$

where u is the atomic mass unit and A is the relative atomic mass.

The photoelectric effect is the absorption of the photon by an electron. The photo-electron will have a kinetic energy equal to the energy of the incident photon minus the binding energy of the original electron. Below energies of 50 keV it is the dominant effect, the photoelectric effect is stronger for low energies and its contribution declines steadily towards higher energies. The magnitude of the effect also depends on the atomic number, with higher atomic numbers increasing the effect. If the energy of the photon matches the energy of an electron binding energy, the interaction cross section increases. If the energy of a photon is smaller than any available electron shell transition, it cannot interact. These binding energies lead to sharp discontinuities (absorption edges) in the plot of the cross section over energy as seen in fig. 10.

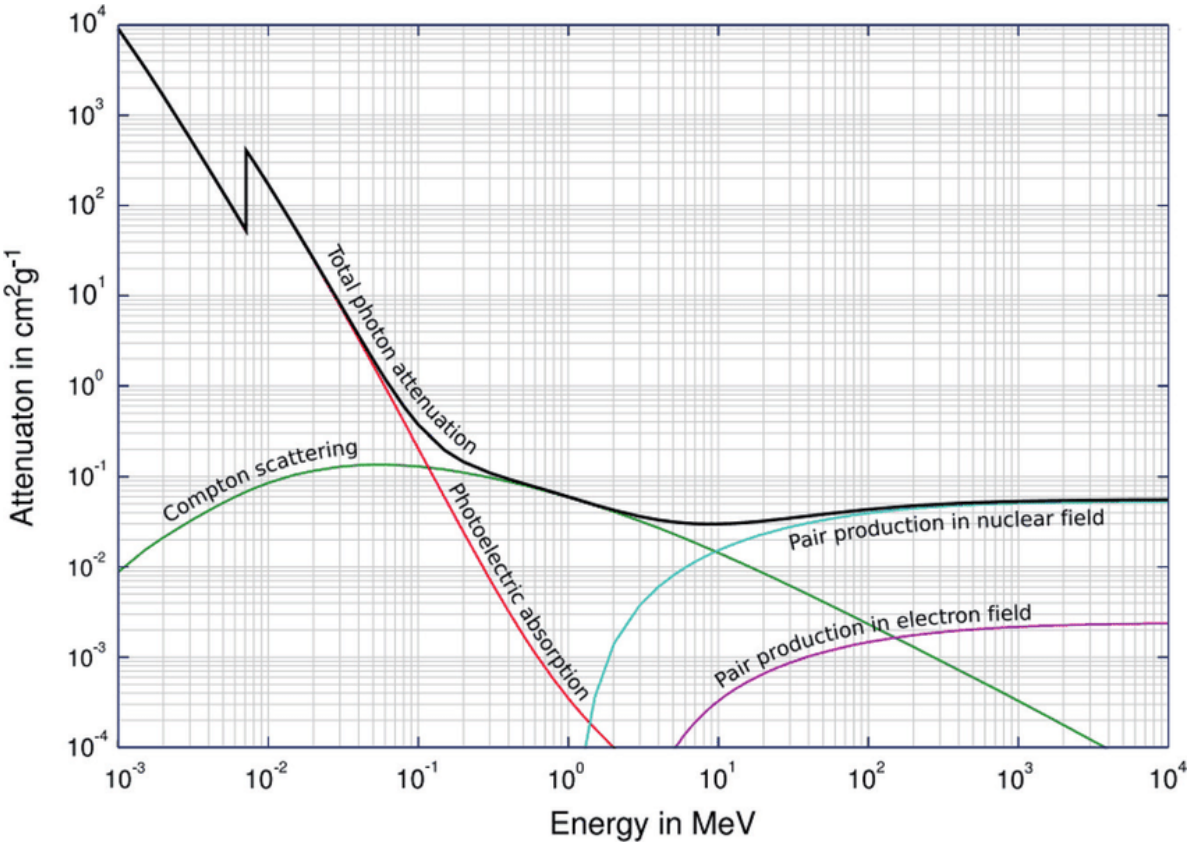

Figure 10: The different interaction mechanisms and their contributions to the overall attenuation over energy. This plot is not for any specific element and the exact curve varies considerably for different elements especially the absorption edges [16].

The Compton effect is the interaction and transfer of energy between a free electron and an incoming photon. As opposed to the photoelectric effect not the whole energy of the photon is transferred to the electron. The fraction of the original energy that isn't transferred to the electron is carried away by a new lower energy photon which has a separate direction. In essence the photon scatters inelastically on the electron, hence the term Compton scattering. Compton scattering has a maximum contribution at intermediate energy levels 100 keV to 10 MeV. Since the photon energies are much higher than the binding energies of the electrons, the electrons can be assumed to be quasi-free. To further point out the differences between the photoelectric effect: the photoelectric effect is the complete transfer of the photon energy onto a bound electron. The Compton effect is the partial transfer of energy to a quasi-free electron. The angle of deflection for the outgoing photon ϕ depends on the energy exchanged during the interaction. The exact relation is written in eq. (12), with E' being the energy of the energy after the interaction, E the energy before interaction, m_e the electron mass and c the speed of light.

$$\frac{1}{E'} - \frac{1}{E} = \frac{1}{m_e c^2}(1 - cos\phi) \tag{12}$$

This relation leads to prominent features in the spectrum, mainly the Compton edge. It is an abrupt drop in the spectrum. A Compton edge is the maximum energy loss experienced by a photon during a Compton scattering event.

Pair production is the creation of a particle antiparticle pair by a photon. An electron positron pair is the lightest particle antiparticle combination and therefore requires the least amount of energy. For this process to happen the energy of the initial photon must exceed the energy of the combined mass of electron and positron 1.02 MeV. Conservation of energy and conservation of momentum are the primary constraints of the interaction. Energy conservation dictates the minimum energy, energies higher than the minimum energy are accounted for in the kinetic energy of the particles involved. Besides energy and momentum, electric charge, lepton number and angular momentum also have to be conserved. If the energy of the photon is high enough it is also possible to produce pairs of heavier particles. Pair production cannot fulfill conservation of momentum in free space. Because of that the process can only occur in proximity of an atomic nucleus. This atomic nucleus also receives some momentum during the interaction. The contribution of pair production to the overall absorption coefficient rises with energy from the initial minimum energy jump. At energies of 10 MeV pair production is the dominant method of interaction. If the process happens in the field of an electron instead of a nucleus it is called triplet production. For this process to happen the photon energy needs to be at least 2.04 MeV. In pair production the nucleus inherits minimal energy during an interaction. The low mass of an electron compared to a nucleus means the electron gets imparted a significant energy during triplet production. The contributions of triplet production are minimal and usually neglected.

Besides these three modes of interaction there is also Thomson scattering. Thomson scattering is the elastic scattering of photons by a free electron. It can be seen as the low energy limit of Compton scattering. The overall contribution of this effect is minor and only present at low energies.

4 Introduction to the used Detectors and SiPMs

4.1 Silicon Surface Barrier Detectors

Of all the interactions listed in section 3.0.3 and section 3.0.1, excitation/ionization processes or creation of electron-hole pairs is what is ultimately detected in a semiconductor detector [17]. A semiconductor detector can be seen as a solid-state ionization chamber. Simplified - it is a reverse biased diode. When a bias voltage is applied via the two electrodes to a silicon crystal with an n–p junction, the excess electrons are drawn in one direction and the holes in the opposite direction. This creates a depletion layer between the two that is nonconducting. This depletion region is where interactions are detected. The depletion region should be thicker than the penetration range of the particles being detected. The thickness of the depletion region depends on the applied bias voltage, with higher voltages leading to thicker depletion regions. If ionizing radiation is absorbed in the depletion layer, it creates numerous electron-hole pairs. The energy needed to lift an electron from the valence band into the conduction band (-to create a single electron-hole pair) is 3.62 eV in silicon at room temperature. This value is higher than the band gap of silicon (1.115 eV) since silicon is an indirect band gap semiconductor. The 3.62 eV are lower than for example the 30 eV required for typical gas filled detectors. Thus for a given amount of deposited energy more charge carriers are created in silicon leading to better energy resolution in silicon. Along the track of the primary ionizing particle a plasma tube of electrons and holes with concentrations of ($10^{15} - 10^{17}$ per cm^3) is created. The trick is to collect the charge carriers before they recombine. A high purity semiconductor material is needed. Electron-hole pairs that are created migrate/drift in the electric field applied via the electrodes. The electrodes lose charge proportional to the amount of holes/electrons created by the interaction. This collected charge is detected and proportional to the deposited energy of a detected particle or photon. The electrode contacts may be thin metal layers (usually Au and Al) called surface barriers in the case of Surface Barrier Detectors. The two planar parallel electrodes act as a capacitor and therefore have the capacitance of the corresponding parallel-plate capacitor - affecting the behavior of the pulse shape. The electrodes also absorb some of the energy without generating a charge - degrading the energy resolution. It is thus better to manufacture the conducting layer as thin as possible (typical 40 $\mu g/cm^2 \widehat{=}$ 20 nm).

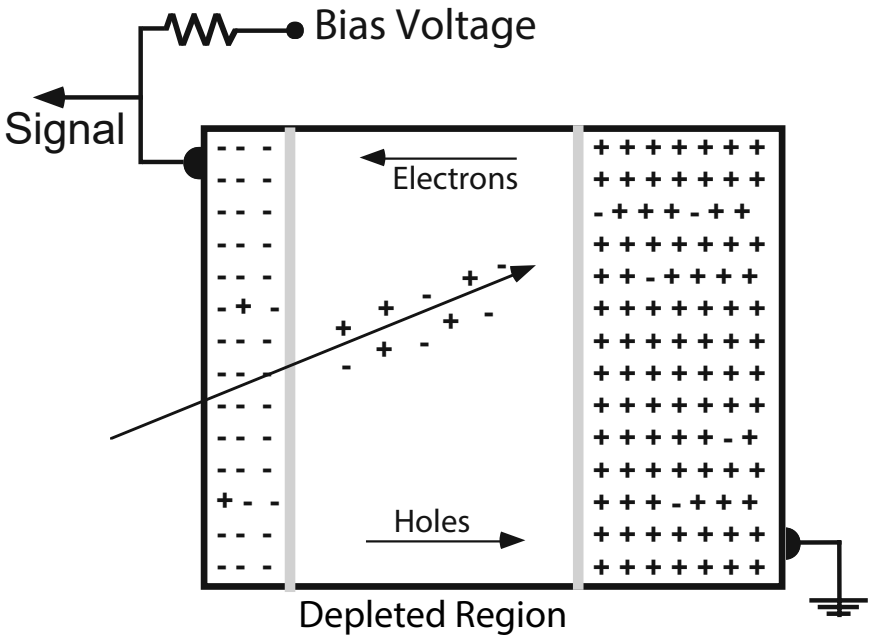

Figure 11: The bias voltage creates a depleted region. β or γ radiation will create electron-hole pairs in this region. The electrons and holes are collected to provide the signal. Image adapted from [18]

4.1.1 Pulse Counting

In semiconductor detectors the energy necessary to form a single electron-hole pair is essentially independent of the energy of the incoming particle, instead it depends on the detector material. The number of electron-hole pairs ultimately formed is thus directly proportional to the energy of the stopped particle. While the signal from the semiconductor detector is a charge pulse, most detectors immediately convert the current to a voltage drop over a resistor. Regardless of the detector the output from the preamplifier is usually a voltage pulse [19]. The shape of this pulse can be characterized by two parameters: the pulse rise time and the decay time of the charge (time constant). The shape of a typical pulse or the parameters of the pulse are important when evaluating the pulse energy and distinguishing it from noise.

The pulse rise time associated with an ionizing event is a function of the mass, energy, range of the ionizing particle, the detector parameters (depletion depth, electric-field strength, diode series resistance and sensitive area) and the characteristics of the associated electronics [20]. A simple way of classifying a pulse is to set a voltage discriminator level, pulses crossing this level are classified as a pulse, everything else is rejected as noise. More advanced digital signal processing methods sample the voltage at regular intervals and look at the difference between a train of subsequent voltage measurements. When assigning an energy to a pulse there are two challenges. Noise may have a higher amplitude than an actual pulse and it is not possible to measure pulses below a certain energy. Another problem especially at higher count rates are simultaneous pulses. It is not possible to extract the energy of the individual particles. For a energy spectrum pulses consisting of multiple events have to be discarded. When the individual particles enter the detector at not exactly the same time, then these pulses can be identified from the deviated pulse shape by more advanced counting methods. The time it takes to restore proper measuring conditions is called the dead time (see fig. 12). During this interval

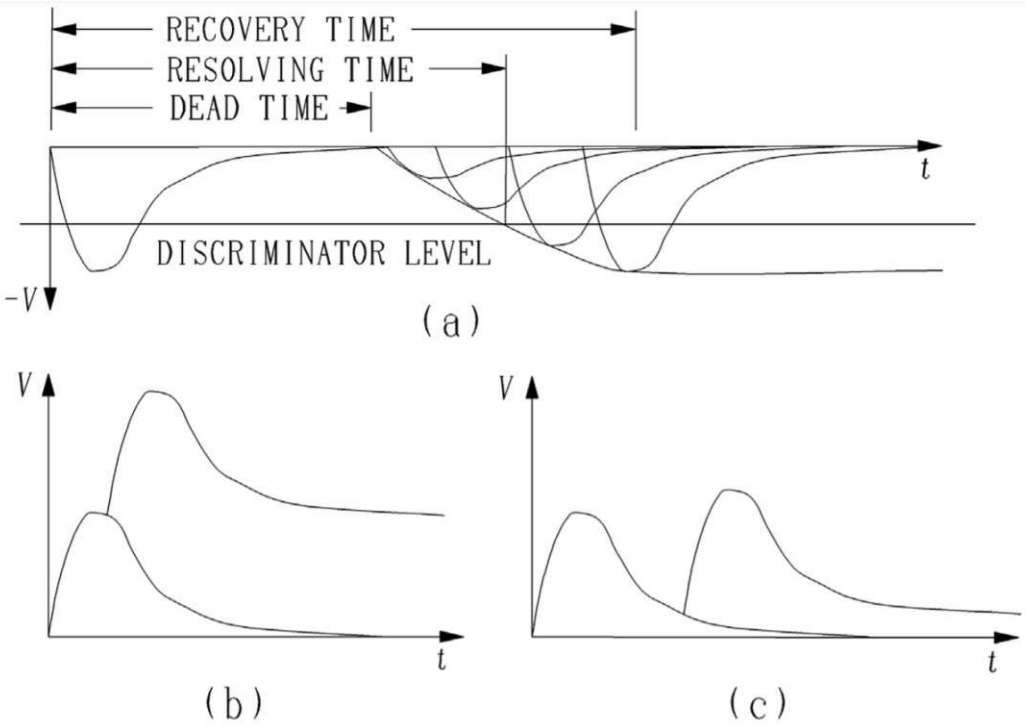

Figure 12: (a) Dead time and other timing in a discriminator based detector. (b) peak pile-up and (c) tail pile-up [19].

the detector cannot collect new charge. The time needed to separate two events is referred to as resolving time. After the recovery time the system is able to fully capture the individual energies of two events. Since radioactive decay is a statistical random process even for relatively low count rates a certain percentage of events will occur within the resolving time of the system and distort the true count rate.

4.2 Scintillation Detectors

In simplest terms a scintillator is a material that emits light (in the range of the visible spectrum) when crossed by ionizing radiation. The scintillation mechanism differs between organic and inorganic crystalline scintillators. In this work only inorganic scintillators were used and the following description applies to inorganic scintillators. The whole process can be divided into three consecutive sub-processes, which are in order: absorption/conversion, migration and luminescence [21]. Initially in conversion ionizing radiation lifts electrons from the valence band into the conduction band thereby creating electron-hole pairs. Electrons in the lower valence band are essentially bound to lattice sites. Electrons in the conduction band and vacancies or holes can move freely. In the transportation phase electrons and holes migrate across the scintillator. They may get repeatedly trapped at defects. These defects or trapping levels are allowed energy levels in the otherwise forbidden gap created by point defects impurities and surfaces/interfaces. By being repeatedly trapped at defects migrating charges are slowed down.

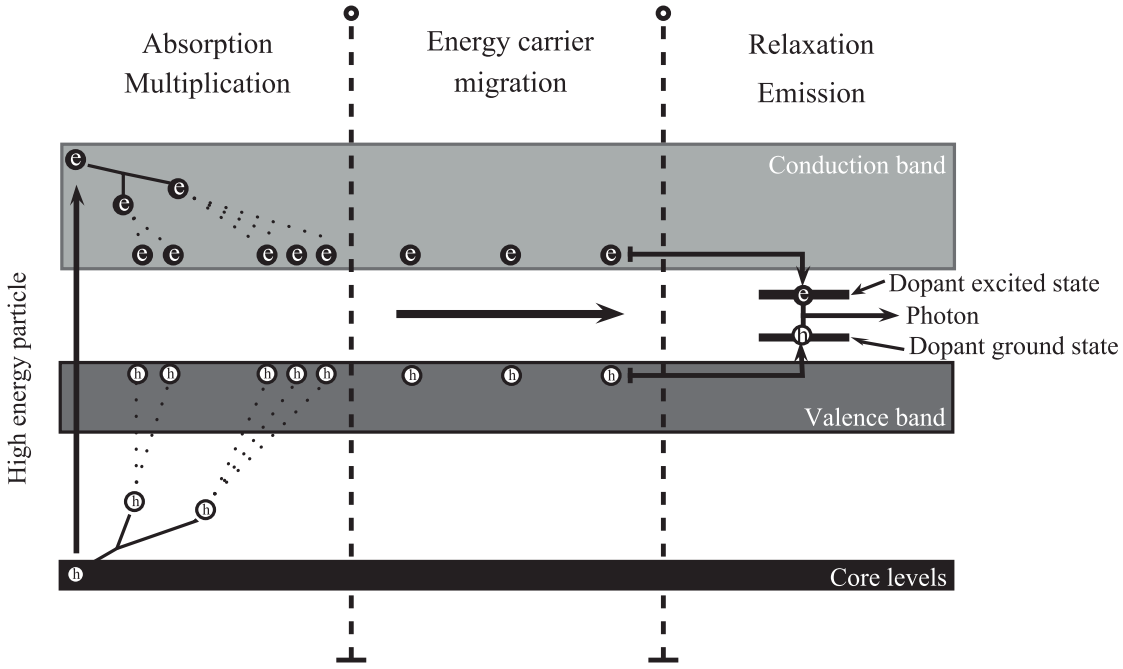

Figure 13: The basic scheme of the various stages in inorganic scintillators. Image adapted from [22]

In the final stage an electron and a hole are trapped at a luminescence center where they radiatively recombine and emit scintillation light. In most pure scintillation crystals, the emission of light via recombination is inefficient [23]. Also, the wide bandgap results in high energy photons outside the visible range which may be undesirable [23]. Trace amounts of impurities are added to the crystal to give useful light output and wavelength. These added impurities are called activators or dopants, they create special sites in the crystal lattice which have a modified bandgap structure. The local activator bandgap structure offers energy bands in the otherwise forbidden region through which electrons can combine with holes. These activator sites are called de-excitation sites, luminescence centers or recombination centers. Their bandgap structure determines the wavelength of the released light.

Photons emitted at activator sites have lower energy than the bandgap energy of the rest of the crystal, thus preventing light absorption by the bulk crystal. The lower energy of photons emitted via activators is in the visible range allowing easy detection by silicon photomultipliers.

Not all scintillators require the addition of an activator, BGO see section 5.2.1 is a notable exception. Once an electron meets a hole at the activator site, the time to transit to the ground state depends on the nature of the transition. An allowed transition will de-excite almost immediately under emission of a photon with half lives in the order of 50 to 500 ns. This half-life determines the time characteristics of the light output since transport time, the time it takes the electrons to migrate to an activator site is much shorter. If the excited state at the impurity site happens to have a forbidden transition to the ground state the de-excitation takes a longer time. This results in an afterglow or background light in some scintillators. Not all created electron-hole pairs emit light. They can also lose their energy through unwanted non-radiative recombination.

The temperature dependence of inorganic scintillators is primarily governed by thermal quenching. With increasing temperature thermal quenching reduces the scintillation light yield. It occurs because the temperature increase promotes non-radiative transitions, such as phonon emission, which reduce the number of excited electrons that would otherwise recombine at the luminescent center and contribute to the scintillation light output [24].

The very first scintillation light pulses were observed with the naked eye. A much better way is to use photo multiplayer tubes, a photodiode or a silicon photomultiplier (SiPM). In this work a silicon photomultiplier was used. The SiPM converts the light into a voltage pulse which can be processed much like the pulses from semiconductor detectors.

4.3 Silicon Photomultipliers

Silicon photomultipliers (SiPMs) are a type of photodetector that is used to detect the low levels of light emitted by scintillation crystals. A SiPM consists of a matrix of many small-sized sensitive elements called micro-cells. All micro cells are usually connected in parallel. The output signal of the SiPM is a current pulse that is proportional to the number of photons detected. Each micro-cell is a Geiger-Mode avalanche photo-diode (GM-APD) that operates beyond the breakdown voltage and integrates a resistor for passive quenching.

Three phases of a micro cell can be defined: quiescent state, discharge phase and recovery phase. During the quiescent state the bias voltage is present and the micro cell stays in this state unless a photon is absorbed (or a dark event occurs). During the quiescent state no current flows. If a photon gets absorbed it generates an electron-hole pair. The discharge phase starts when an electron-hole pair triggers an avalanche multiplication. The bias voltage (Vbias) decreases until charge carriers cannot gain enough energy to generate further charge carriers. It decreases until the breakdown voltage is reached. The avalanche of electrons and holes is detected as an electrical pulse. The exponential avalanche growth needs to be stopped at a suitable moment so that the detector can register the next event. Passively quenched devices use a series resistance to decouple the diode from the bias supply and reduce the electric field, stopping the avalanche growth. Once the avalanche process stops the microcell enters the recovery phase and the microcell can charge back up to the full bias voltage.

If an avalanche discharge in a microcell is triggered, the consequence is a current pulse with the total amount of charge Q flowing through the terminals of the SiPM. The gain of an SiPM sensor is defined as the amount of charge created for each detected photon it is a function of microcell size and overvoltage. It is defined as a ratio of Q and the fundamental charge $e = 1.6{\cdot}10^{-19}C$[1]. Typical gain values are in the range of $10^5{-}10^7$. The breakdown voltage (Vbd) is the minimum reverse bias voltage that can trigger a self-sustaining avalanche multiplication in GM-APDs. It is important to note that even though Vbd is the minimum bias required for obtaining output pulses, the detection efficiency and gain of SiPMs are still zero at Vbias=Vbd. Only when Vbias is greater than Vbd are output current pulses observed. The additional voltage beyond the breakdown voltage is called the overvoltage. The breakdown voltage depends on the characteristics of the p/n junction and it has a strong temperature dependence. The gain, noise and photon detection efficiency depend on the overvoltage. Increasing overvoltage results in higher gain, more noise and increasing but eventually plateauing photon detection efficiency. The photon detection efficiency is the percentage of photons arriving on the SiPM surface that are detected.

SiPMs exhibit noise in the form of random output current pulses even when there is no incident light. This is due to the fact that in the semiconductor there is a non-zero probability for carriers (electrons and holes) to be generated by thermal fluctuation. Additionally, SiPMs have a limited dynamic range due to the saturation of a high enough fraction of the APDs at high photon fluxes.

[1] C stands for the coulomb, the unit of electric charge

4.3.1 SiPM Saturation

The charge output of a SiPM in response to an instantaneous light pulse can be approximated by eq. (13)[25]. In eq. (13) all photons of a pulse arrive at the same time.

$$Q = qM\left(1 - \exp\left(\frac{-N_{ph}\ PDE}{M}\right)\right) \tag{13}$$

In eq. (13) Q is the instantaneous charge output, q is the charge from one microcell, M is the number of microcells, N_{ph} is the number of photons and PDE is the photon detection efficiency.

If the light pulse is longer than the recovery time the situation changes [26]. After the duration of a recovery time $t_{recovery}$ a microcell returns to its sensitive state.

$$Q_{eff} = qM\frac{t_{pulse}}{t_{recovery}}\left(1 - \exp\left(\frac{-N_{ph}\ PDE\ t_{recovery}}{M\ t_{pulse}}\right)\right) \tag{14}$$

Q_{eff} is the charge output of the SiPM and t_{pulse} is the time length of the pulse. The recovery time of a typical SiPM is in the same range as the scintillation decay time of YSO. The scintillation decay time is defined as the time required for scintillation emission to decrease to e^{-1} of its maximum. A response of a standard SiPM and YSO is shown in fig. 14.

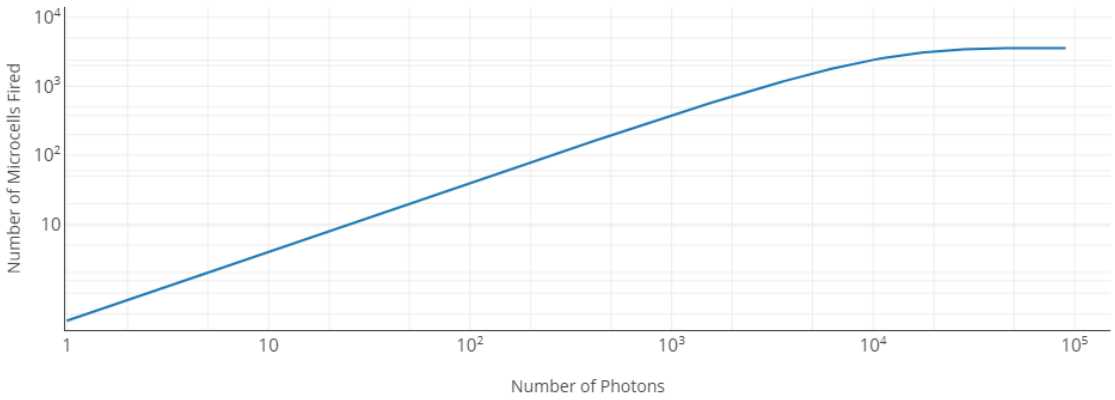

Figure 14: The number of activated microcells in relation the number of incident photons. Both axes use a logarithmic scale [26].

5 Experimental Setup and Methods

5.1 Experimental Design of CREScent

The experiment consists of a vacuum cavity with an inner diameter of 100 mm and an inner length of 900 mm. This vacuum chamber is located inside the bore of a 4.7-tesla superconducting horizontal bore magnet by Magnex Scientific which provides the background magnetic field. Eight shim coils integrated within the bore of the magnet were available to homogenize the field. Around the cavity are the two normally conducting coils generating the trap field. The two trap field coils are 205 mm apart and consist of 15 windings with a current of 10 A resulting in an additional 1.2 mT trap field. At a field strength of 1 T and an additional trap field of 1.2 mT, the resulting axial field resembling a bathtub shape (fig. 17) will confine electrons with a pitch angle greater than 88.01 degrees[2]. The vacuum inside the cavity is generated using an Alcatel cfv100 turbomolecular pump capable of reaching 10^{-6} mbar measured at the pump inlet. The emitted cyclotron radiation is picked up by a specifically designed RF coupler and fed into a vector spectrum analyzer. In the first phase of the experiment the electrons are provided by a ^{207}Bi conversion electron source. The ^{207}Bi source consists of a thin carbon fiber wire with ^{207}Bi adsorbed onto the center of the wire. The carbon fiber wire is stretched across the center so that ^{207}Bi is suspended in the middle of the chamber.

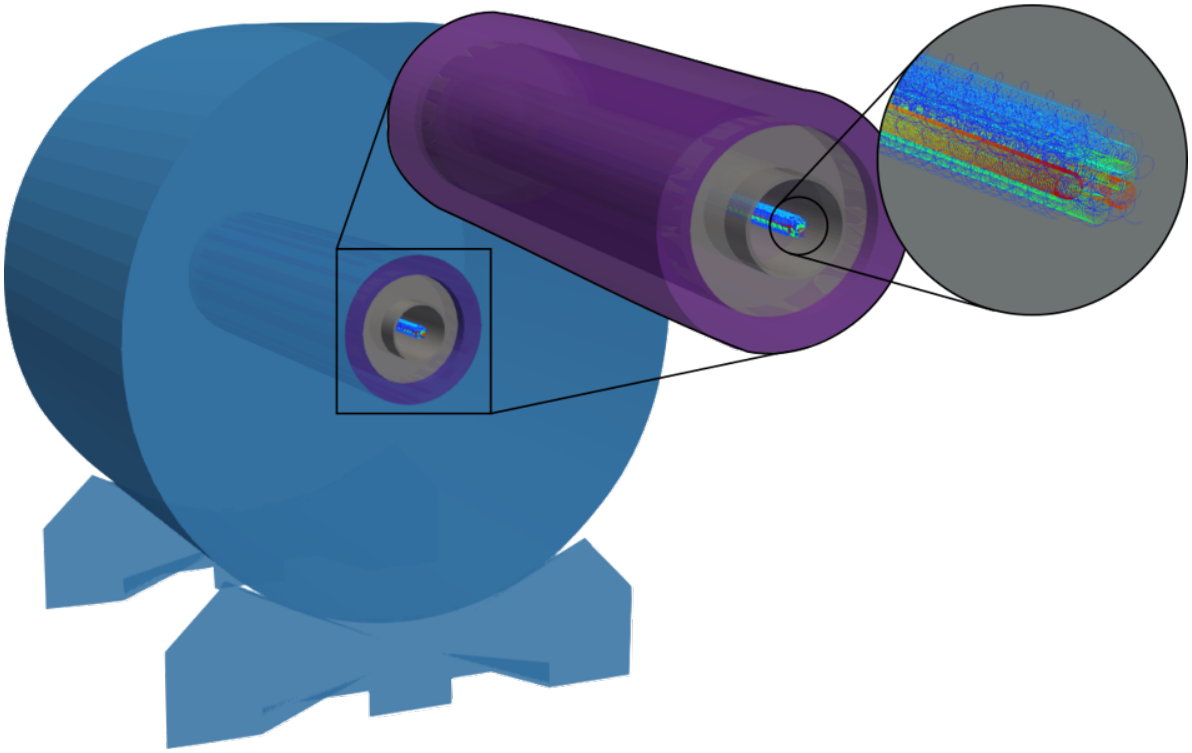

Figure 15: The 4.7-tesla superconducting horizontal bore magnet by Magnex Scientific [27]. In the magnified view the paths of gyrating electrons can be seen.

[2]calculated using eq. (3)

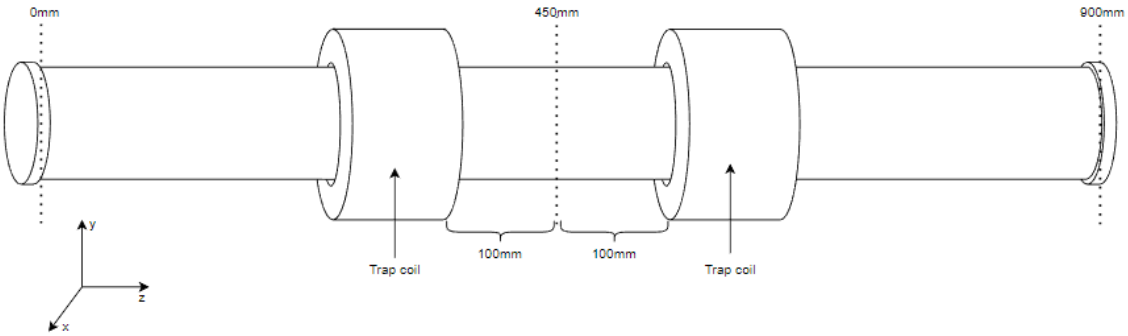

Figure 16: The vacuum cavity and the coils for the trap field. The vacuum port is located on one end of the tube, on the other end the RF coupler is located [10].

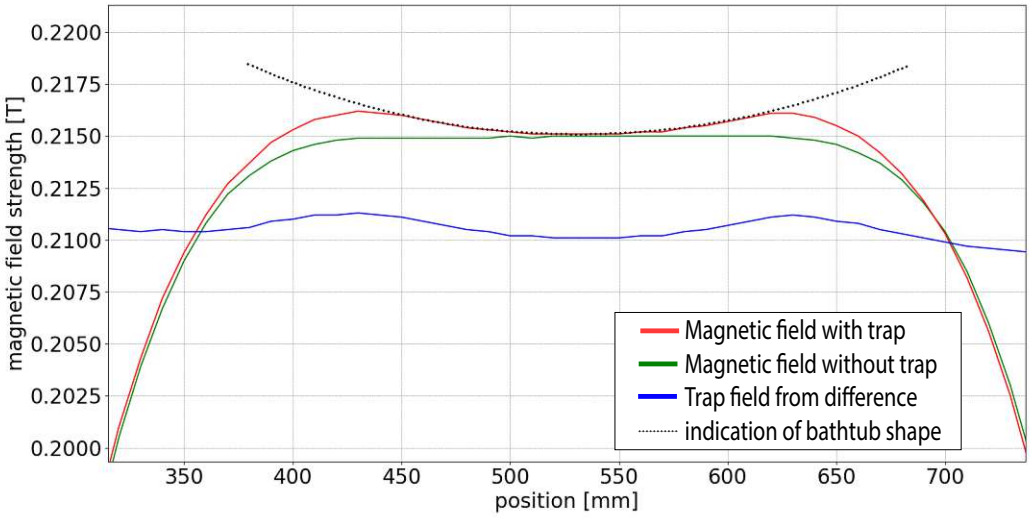

Figure 17: The black dotted line highlights the bathtub shape of the trap field. The red and green lines represent the axial magnetic field with trap field on and off. The blue line is the difference between the trap on and off measurements plus an offset of 210 mT. The blue line represents the isolated trap field.

5.2 Detector Setup

To detect the emitted electrons and gamma photons different types of detectors were tested and used. The detectors can be divided into two categories silicon surface barrier detectors and scintillation based detectors. A description of the surface barrier detector setup can be seen in appendix A.3. A scintillation detector setup was ultimately used for the measurement of the effectiveness of the magnetic trap. The scintillation detector setup is described in the following section.

5.2.1 Scintillation Detector Setup

Two different scintillation crystals were used: Bismuth Germanate ($Bi_4Ge_3O_{12}$, BGO) and Yttrium Orthosilicate doped with Cerium (Y_2SiO_5:Ce, YSO). Their properties are listed in table 1. BGO has a high atomic number and density. Thus, it is able to absorb higher energy photons. It is non-hygroscopic and mechanically strong. It has a long decay time compared to YSO which is often undesired but did not result in any problems since the count rates of all measured samples were relatively low. The poor light output of BGO meant that the electric signal had to be amplified a lot which has disadvantages. BGO is intrinsically radioactive which means the scintillator detects itself, resulting in very minor background counts[3]. YSO compared to BGO has a high light output (three times as much) which is the main advantage of YSO over BGO, YSO is also non-hygroscopic and mechanically strong. Yttrium, silicon and oxygen do not have unstable isotopes, so there are no intrinsic background counts.

Scintillator Crystal	Density $[\frac{g}{cm^3}]$	Luminosity [photons /MeV]	Decay Time [ns]	Energy Resolution [% fwhm 662 keV peak]	Emission maximum [nm]
YSO Y_2SiO_5	4.45	23400 [28]	42 [29]	9.4 [30]	420
BGO $Bi_4Ge_3O_{12}$	7.13	7610 [31]	300 [32]	9.05 [33]	480

Table 1: Important parameters for each crystal. The energy resolution is defined by the full width at half the maximum of the peak and it is specified as the FWHM energy width as a percentage of the energy of the peak. In this case the energy resolution is listed for a 662 keV peak (^{137}Cs). The decay time is defined as the time required for the scintillation light intensity to decrease to e^{-1} of its maximum. Most scintillators have more than one decay time, here the effective average decay time is listed. Scintillation crystals produce a spectrum of light, under emission maximum the intensity maximum of this spectrum is listed.

The YSO crystal had dimensions of (20 x 4 x 4) mm^3, all sides were polished. The whole BGO crystal had dimensions of (20 x 6 x 5) mm^3 and the two (20 x 5) mm^3 sides were polished, the other sides were rough. The BGO crystal did not consist of one single piece, instead it consisted of two pieces that were glued together lengthwise. In order to collect as many scintillation photons as possible the crystals were wrapped in Polytetrafluoroethylene (PTFE, "Teflon") tape. A window of approximately (5 x 5) mm was kept clear of Teflon

[3]This effect is completely negligible in this work.

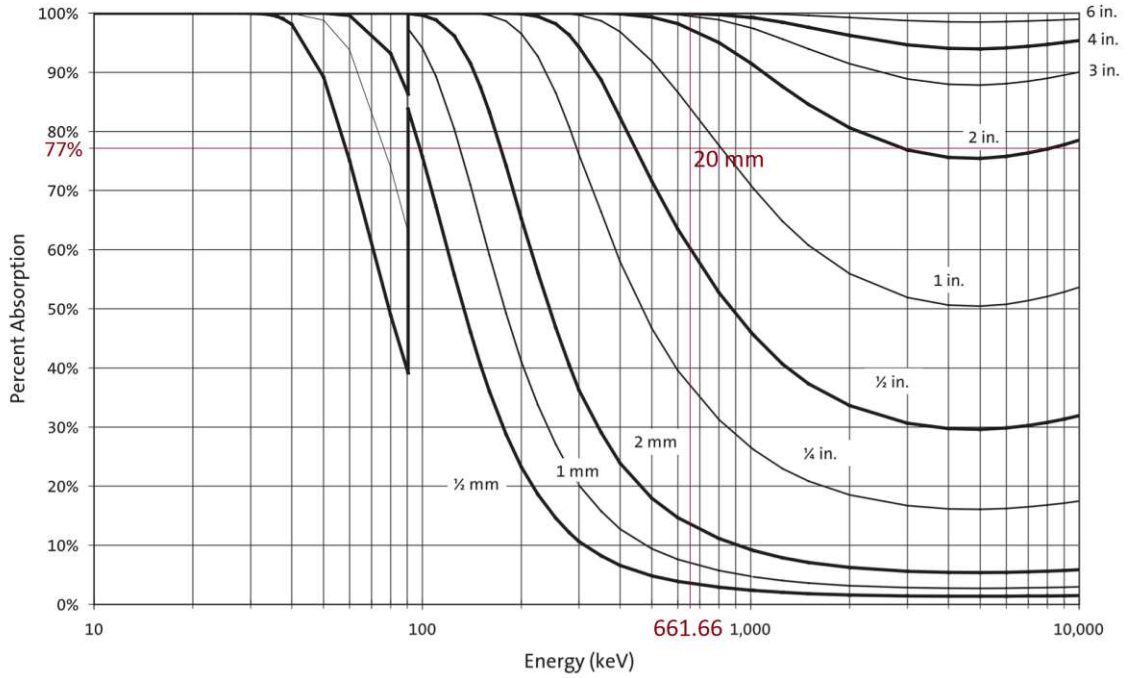

Figure 18: Gamma absorption efficiency graph for BGO. 77% of 661 keV photons are absorbed when traversing 20 mm of BGO crystal [34]. 661 keV is used as an example because it is the energy of ^{137}Cs, a convenient calibration source. 20 mm of YSO would would absorb about 46% of all 661 keV photons.

to allow the unhindered entry of electrons. To transmit the light from the crystal to the silicon photomultiplier optical silicone grease was applied between BGO and the SiPM. The YSO crystal was permanently glued to the SiPM on one of the (4 x 4) mm faces. On some measurements the YSO crystal was encased in a lead and brass shield. This shield had a 4 mm diameter circular entry path allowing only a narrow beam of radiation to reach the detector, essentially a collimator. All measurements were performed either in the total darkness inside the vacuum chamber or the scintillator was otherwise shielded from light. For measurements inside the vacuum chamber a vacuum feedthrough between the SiPM and the preamplifier was used. For temperature measurements a Pt100 type resistance thermometer was used which was attached to the side of the crystal. The preamplifier has a fixed amplification of three and allows adjusting the current passing through the SiPM. It combines a preamplifier and an amplifier inside of the same board. The preamplifier also provides the bias voltage. It was provided by the Stefan Meyer Institute for Subatomic Physics of the Austrian Academy of Sciences (see appendix B).

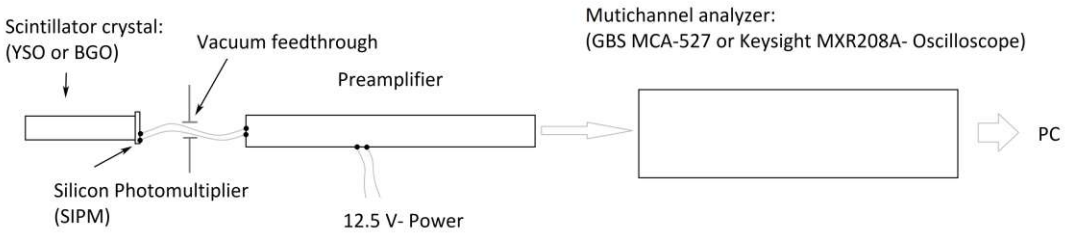

Figure 19: The signal chain for the scintillation setup. Depending on the measurement there was a vacuum feedthrough between preamplifier and SiPM. The preamplifier had its own 12.5 V power source and fixed 3x amplification. The vacuum feedthrough is mentioned because the associated longer cable length has the potential to degrade the signal, however no change in signal was observed.

The signal from the preamplifier was picked up by either a GBS MCA-527 Multichannel analyzer or a MXR208A oscilloscope. The GBS MCA-527 samples the input signal from the preamplifier with a 14-bit analog to digital converter at a rate of 10^6 samples per second equating to one voltage measurement every 100 ns. This device is specifically designed for gamma spectroscopy and is capable of digital signal processing, amplification, pile up rejection and has 16384 energy channels. The other device used to capture the pulses was the Keysight MXR208A oscilloscope. It was able to create a histogram of all pulses and capture each pulse in a higher fidelity. The MXR208 oscilloscope has only 8192 voltage channels. On certain measurements a Tektronix TDS 2024C oscilloscope was used. To minimize a potential influence of the magnetic field on the electronics, the preamplifier and the multichannel analyzer were placed at distances with a magnetic field of 5 mT or lower.

5.3 β and γ Sources

To characterize all the different detectors multiple sources were available. The sources can be organized into three groups: gamma sources, closed beta sources and the two open ^{207}Bi sources. The beta sources are listed in the following table 2. These nuclides have a continuous electron spectrum. All β sources are sealed between two thin polymer foils. The gamma sources listed in table 3 are molded into the center of a 3 mm thick block of plastic.

Nuclide	Activity [Becquerel]	β Endpoint Energy [keV]
^{14}C	3951	156.48 [35]
^{90}Sr	4357	545.9 [36]
^{36}Cl	4297	709.5 [37]

Table 2: The beta sources. ^{90}Sr decays to ^{90}Y which is also a beta emitter with an endpoint energy of 2274 keV. The overall spectrum of the ^{90}Sr source is the superposition of both contributions. ^{14}C shows just the characteristic beta spectrum (see section 2.1).

Nuclide	Activity [Becquerel]	Energy peaks of interest [keV]
^{137}Cs	24730	661.66
^{133}Ba	7350	81.0, 356.02
^{60}Co	1680	1173.2, 1332.5
^{152}Eu	10210	121.78, 344.28, 778.9, 964.08, 1089.7
^{22}Na	50	511.0, 1274.5
^{210}Pb	85170	46.54, 671.45
^{226}Ra	55680	many from 186.1 to 2447.9
^{241}Am	36390	59.54
^{198}Au	-	411.80

Table 3: Gamma sources, the activity was measured on January 2 2018. ^{198}Au has a half-life of 2.69 days and the activity was not determined. All the sources are encased in the center of a 3 mm thick plastic disc (except ^{198}Au). If a source emits beta particles, they would be absorbed by the 1.5 mm plastic. A detailed decay scheme of each source can be seen in appendix A.5.

The main ^{207}Bi source consists of a thin carbon fiber wire with ^{207}Bi adsorbed onto the center, it can be seen in fig. 20. All the ^{207}Bi is localized at the very center of the carbon fiber wire. The carbon fiber wire is tensioned and protected by a plastic holder. The plastic holder is also shaped in a way that allows it to be positioned inside the vacuum chamber. The ^{207}Bi needs to be suspended radially in the very center of the magnetic field and it should also be centered axially between the two magnetic mirrors. Whatever holds the source in the middle should absorb or attenuate as few electrons as possible. As the electrons move between the two magnetic mirrors they have the possibility to collide with the carbon fiber wire on every pas. A thin carbon fiber wire offers few opportunities for interaction and was therefore chosen as the support for the bismuth. The source has an activity of around 9 kBq. A second unsealed ^{207}Bi source is adsorbed on the surface of a piece of aluminum foil and has a comparable activity.

^{207}Bi decays via electron capture (or to a lesser extent, positron emission) to ^{207}Pb with a half-life of 31.55 years. It emits internal conversion electrons at energies of 481.7 keV and 975.7 keV with probabilities of 1.54 percent and 7.11 percent respectively. Besides these, other conversion electrons, Auger electrons, X-ray photons and γ photons are also emitted from the decay. Since ^{207}Bi is more relevant to the characterization of the trap a list of most energies is given in table 4. A decay scheme can be seen in fig. 68.

Type	Energy [keV]	Intensity [%]
Auger-L	5.2 - 15.7	53.8 (14)
Auger-K	56.0 - 88.0	2.8 (3)
ce-K-1	481.7	1.52 (2)
ce-L-1	553.8 - 557.7	0.440 (6)
ce-M-1	565.8 - 567.2	0.15 (2)
ce-K-2	809.8	0.003 (1)
ce-K-3	975.7	7.03 (13)
ce-L-3	1047 - 1051	1.84 (5)
ce-M-3	1059 - 1061	0.54 (7)
ce-K-4	1682	0.02 (1)
β+max	806.5	0.012 (2)
β+av	383.4	
X-ray L Σ	9.18 - 15.8	33.2 (14)
X-ray Kα Σ	74.2	58.19 (24)
X-ray Kβ Σ	84.4 - 87.6	16.22 (25)
γ	328.11	0.00076 (8)
γAnnihilation	511.0	0.0024 (4)
γ	569.70	97.76 (3)
γ	897.8	0.131 (6)
γ	1063.7	74.58 (49)
γ	1442.2	0.131 (2)
γ	1770.2	6.87 (3)

Table 4: Gammas, X-rays and betas emitted during the ^{207}Bi decay without any magnetic field [38]. Under intensity the number of photons per 100 disintegrations is listed. The number in brackets denotes the uncertainty (1-sigma). "ce" stands for conversion electron and the additional letter denotes the shell the electron had occupied prior to the ejection. Σ signifies weighted mean energies and intensities.

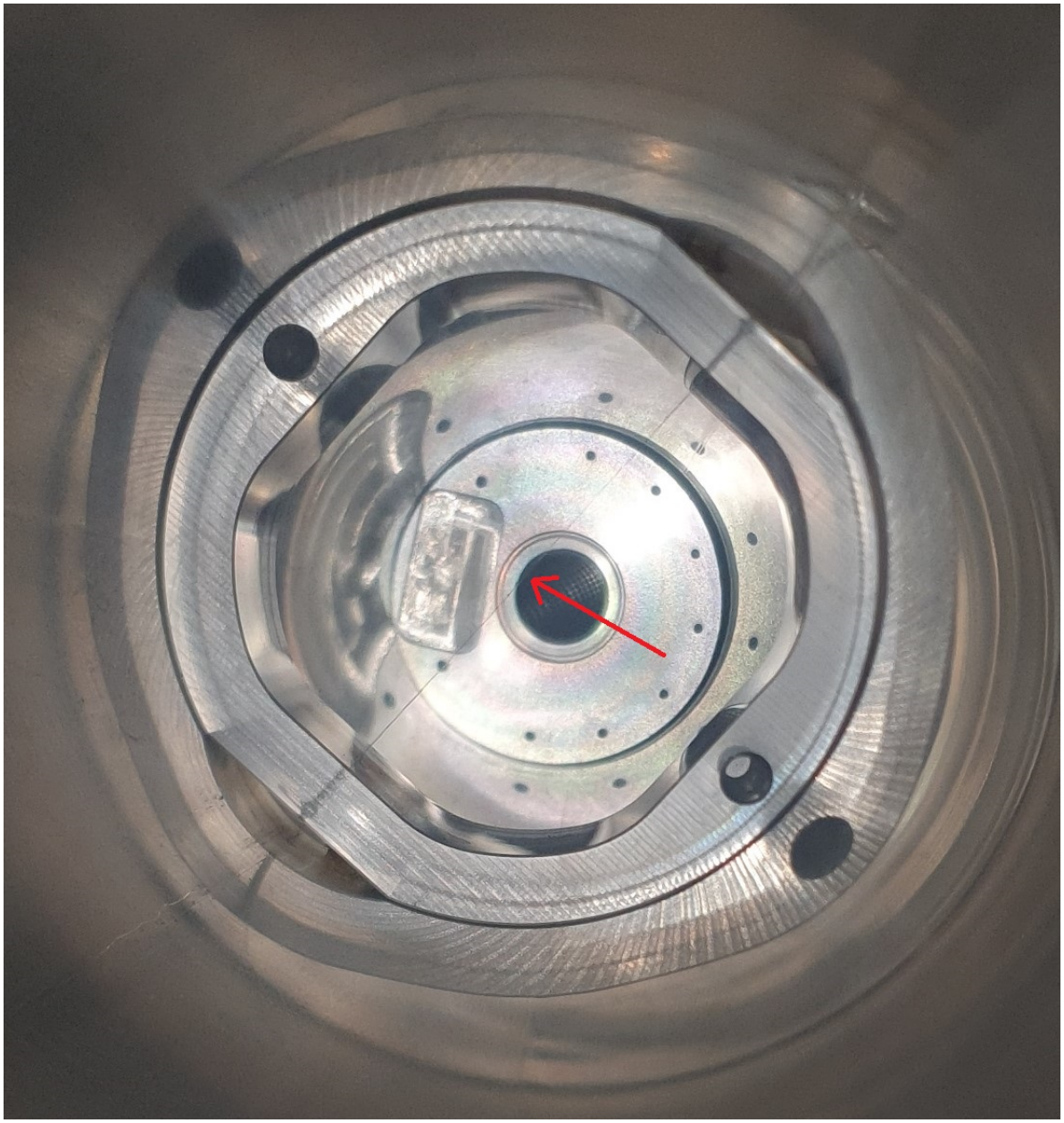

Figure 20: The open ^{207}Bi source in the vacuum cavity. The red arrow indicates the position of the adsorbed ^{207}Bi on the thin carbon fiber wire. The vacuum port can be seen in the background.

5.3.1 Assessment of Countrates

To estimate the measured countrate *cps*, equation eq. (15) can be used.

$$cps = \frac{A\,r^2}{4\,D_e^2} = \frac{A\,s}{4\pi\,D_e^2} \tag{15}$$

Equation (15) assumes an isotropically emitting point source of activity A in [Bq], D_e is the distance of the detector edge to the source, r is the radius of a circular detector and s is the detector surface area.

Equation (15) is an approximation valid only for large D_e compared to r. Equation (16) is accurate irrespective of the distance of source to detector. D_c is defined as the distance of the center of the detector to the point source. The detector surface is arranged perpendicular to an imaginary line connecting source and detector center.

$$cps = \frac{A}{2}\left(1 - \frac{D_c}{\sqrt{D_c^2 + r^2}}\right) \tag{16}$$

6 Measurements and Experimental Results

6.1 Scintillation Measurement Setup

Scintillation crystals are available in different densities and in large sizes. Therefore, for absorbing high energy photons scintillation detectors are a good choice. The crystals and equipment used in this work are listed in section 5.2.1 .

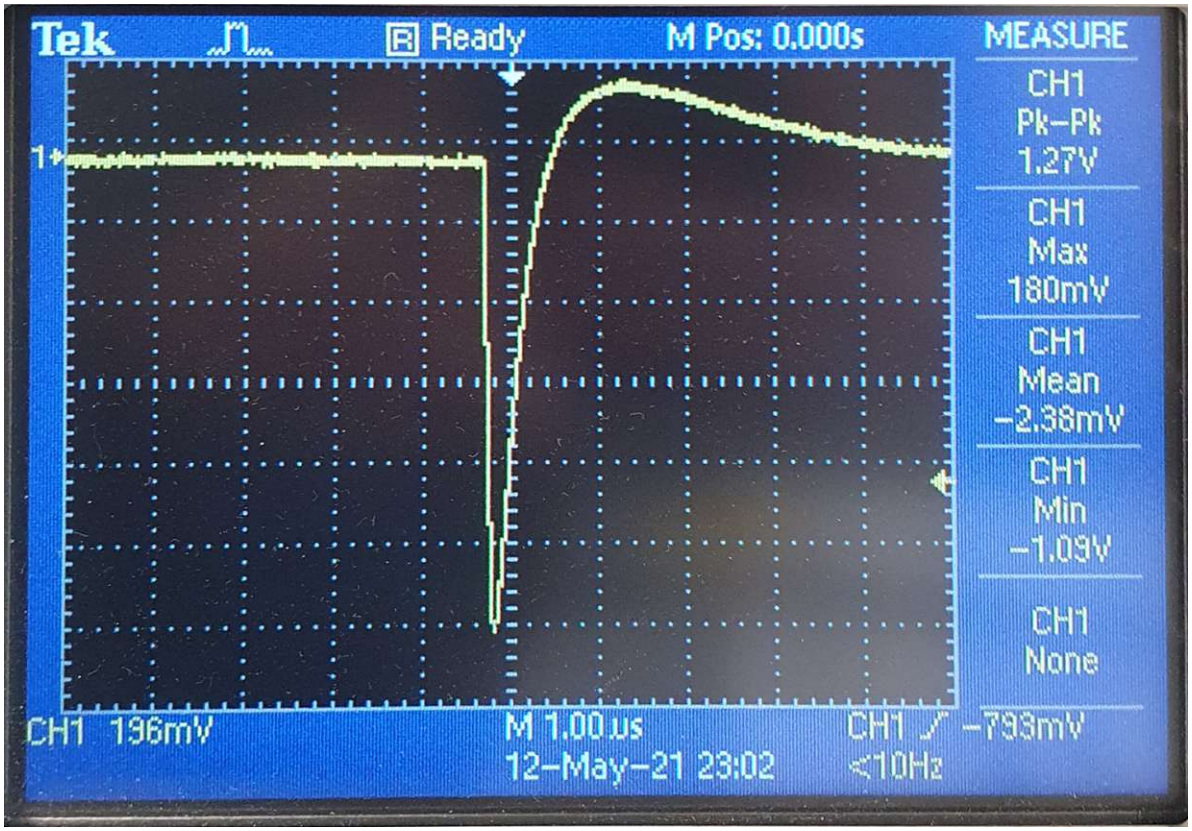

Figure 21: A single pulse from a YSO crystal, measured with a Tektronix TDS 2024C oscilloscope. This pulse has a minimum of 1.09 V and overshoots by 180 mV the overall lowest to highest point being 1.27 V. The horizontal axis denotes time in a 1 μs wide grid. The calibration from chapter section 6.3.2 reveals that this pulse has an energy of 262 keV. Details about pulse shape can be seen in section 4.1.1

In order for the multichannel analyzer to measure the amplitude of a pulse as accurate as possible a multitude of settings can be adjusted. All the following settings apply to the GBS MCA-527 Multichannel analyzer. The MXR208A oscilloscope was not specifically designed for gamma/beta spectroscopy and did not have many of these settings.

Among the most important is the boundary between noise and a real pulse (threshold level). Compared to the semiconductor detectors, the used scintillation detectors had a lower level of noise in relation to signal in other words a higher/better signal to noise ratio. A higher threshold will reduce the low energy noise of a spectrum. A threshold setting of 20 times the root mean square noise level was used for most scintillation measurements. A measurement of the background noise can be seen in fig. 22. The background noise consists of low amplitude

electronic noise that is easily rejected via a higher threshold level. Natural background radiation and cosmic muons did not contribute any meaningful noise. This insignificant noise especially compared to the count rates of a sample (the noise amounts to 0.23 percent of all recorded pulses) means that all scintillation spectra are shown without subtracting the background noise, unlike the surface barrier detector spectra.

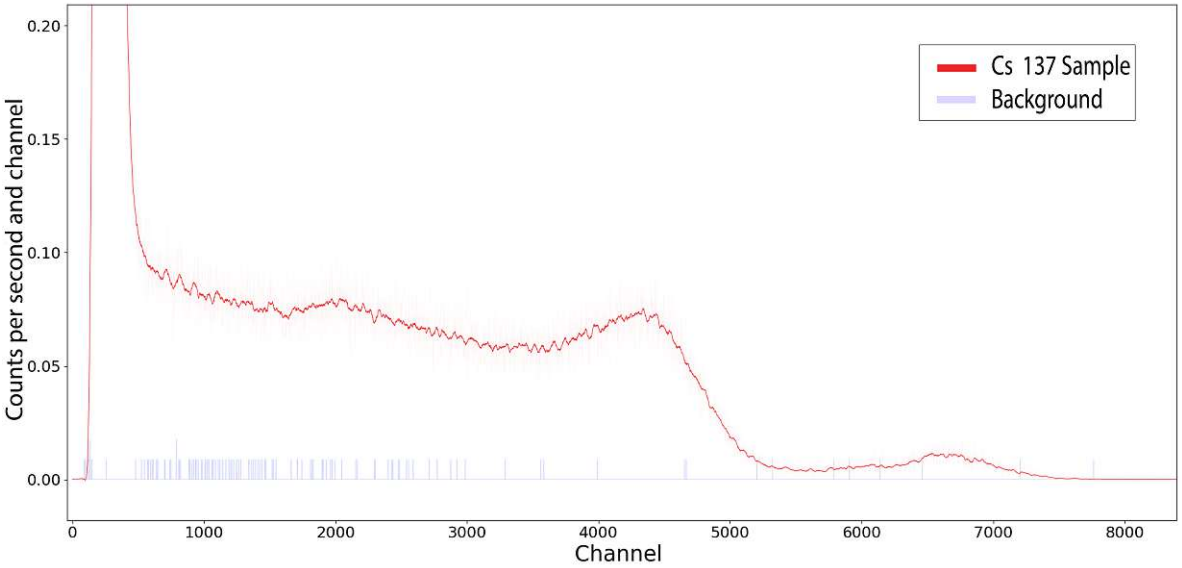

Figure 22: A comparison of the background and a signal. The signal spectrum (red) is ^{137}Cs measured with the MCA. The barely visible blue/gray spectrum is the background noise measured with the same MCA, settings and setup but without a source. Both spectra are normalized to the same measurement time. The full energy peak at channel 6700 and the Compton edge at channel 4040 are visible. The measurement was made with BGO, no energy calibration was made for BGO. The channel number is shown instead of the energy.

Different crystals have varying light output and the preamplifier provided a fixed 3x amplification. Therefore, a scintillator specific additional amplification was used on the MCA. For YSO a coarse gain of 10 and a fine gain of 0.5 was used for most measurements. For BGO a coarse gain of 100 and a fine gain of 0.5 was used for most measurements. Additionally, the maximum 16384 energy channels were used. At the MCA the signal is digitized first. Then this digital signal is processed by two filters: first a short trigger filter is applied continuously to the incoming signal to detect a voltage step. Of all the available trigger filters the filter termed "1,0,-2,0,1" offered a good compromise between time resolution and sensitivity. It was used on all scintillation measurements unless something else is mentioned. The choice of trigger filter manifests itself in the ability to recognize closely following pulses and in the lowest recognized energy. A typical pulse shape can be seen in fig. 21.

Only if a pulse is found a spectroscopic filter evaluating a wider region around the voltage step is applied. When digitizing a signal, amplitude noise and timing jitter affect each discrete voltage sample. To minimize these errors the spectroscopic filter averages multiple voltage samples before and after the voltage step. On the MCA527 the number of these averaged samples and the corresponding time is termed the shaping time. Measurements using BGO and YSO were recorded with shaping times of 0.2 μs.

Timing jitter is the deviation from true periodicity of a periodic signal in relation to a reference clock signal. A rapidly changing signal cannot be digitized accurately, if for example the value changes by 20% within 100 ns and the timing jitter is also in this order it may cause a significant error of also 20%. To omit samples taken during rapidly changing signals a setting called flattop time is used and it should be adapted to the rise or fall time of the signal. A flattop time of 0.4 μs was used on all measurements unless otherwise noted.

Pulses that follow each other too closely cannot be evaluated properly. Pile-up rejection prevents the spectroscopic filter to be applied to these events. Pile-up rejection was used on all measurements. Another critical parameter affecting a measurement was the current across the SiPM. All measurements were made with a current of 1.2 μA.

Besides these mentioned settings/adjustments there are many more. However, if a setting/adjustment makes no impact on the final spectrum it is not mentioned in the previous paragraphs. There are also influences not easily adjustable like the stability of the voltage and the temperature. The influence of the temperature is described in section 6.3.1.

6.2 Silicon Surface Barrier Detector Setup

Generally, semiconductor detectors have a better energy resolution than scintillation detectors. However the semiconductor measurement setup had several flaws. Semiconductor detectors only measure the deposited energy in a relatively thin depletion zone. This depletion zone is adequate to absorb beta radiation but not enough for gamma radiation. Silicon detectors cannot have a depletion zone thicker than a few millimeters, whereas germanium detectors can have a depletion zone of centimeters. These detectors however require liquid nitrogen cooling.

The bias voltage was not known. To determine it, the bias voltage was increased over subsequent measurements until the spectrum matched the expected spectrum. The silicon thickness was also not known for any detector. This means higher energy electrons were either not completely absorbed in the sensitive region or left the detector entirely on the backside. The maximum depth reached by different electron energies is simulated and can be seen in fig. 23. In fig. 23 the surface layer coating was 20 nm gold. Some detectors had an aluminum coating and the exact thickness of the surface coating was not known but 20 nm is a typical value. If the depth or thickness of the depleted layer is less than the maximum depth reached by the electrons the spectrum will be distorted. If the thickness of the entire silicon detector is less than the maximum depth reached by electrons the electrons can leave the detector at the back. In fig. 23 it can be seen that the electrons reach deep within the detector; the energy absorption in the first 20 nm of gold is minimal.

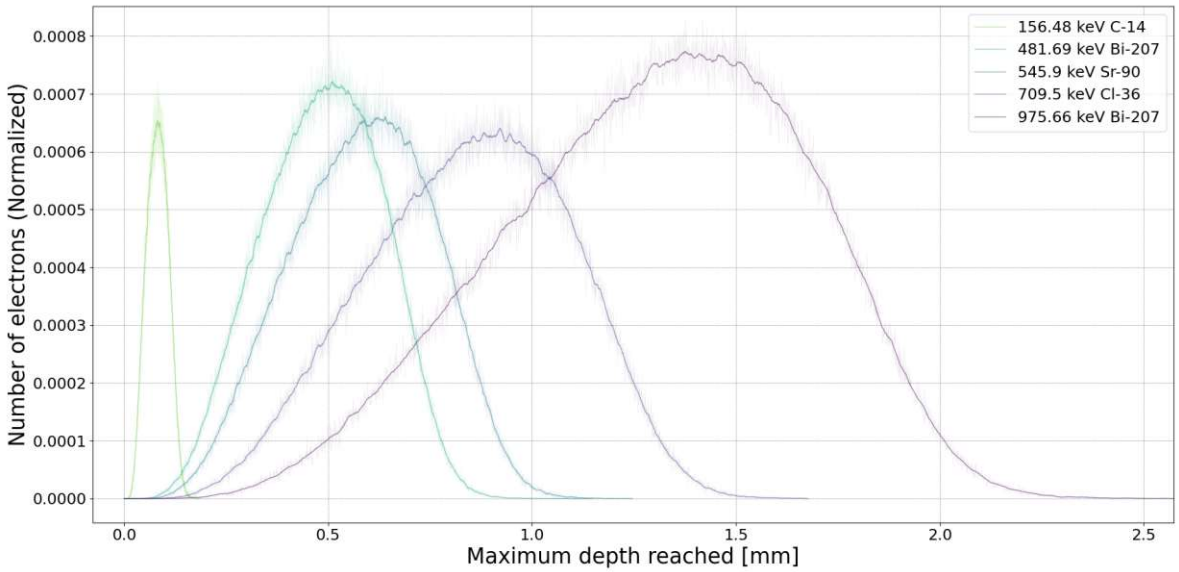

Figure 23: This graph displays the maximum depth reached by electrons in silicon covered by 20 nm of gold. The graph was created by simulating the paths of 10^5 electrons each in the program: "CASINO Monte Carlo Software" [14]. These Monte Carlo simulations also yielded backscattering coefficients of 0.083 for the lowest energy to 0.046 for 975 keV. The selected energies are either monoenergetic peaks of ^{207}Bi or the endpoint energy of the characteristic beta spectrum.

For the measurements the settings of the multichannel analyzer were adjusted to the detector. A description of all parameters is given in section 6.1. The biggest difference to scintillation detectors was the slow rise back to baseline and the higher level of noise compared to signal. The threshold level determines which pulses are noise or real counts, a higher threshold level reduces the noise but also cuts of valid pulses. To obtain a source spectrum two measurements were taken, one with source and one without source, both measurements had the same settings. The noise peak can then be subtracted to obtain the source spectrum. All measurements were made shielded from ambient light. The measurements in fig. 24 were taken in vacuum and the sample was 5.75 mm away from the surface of the detector.

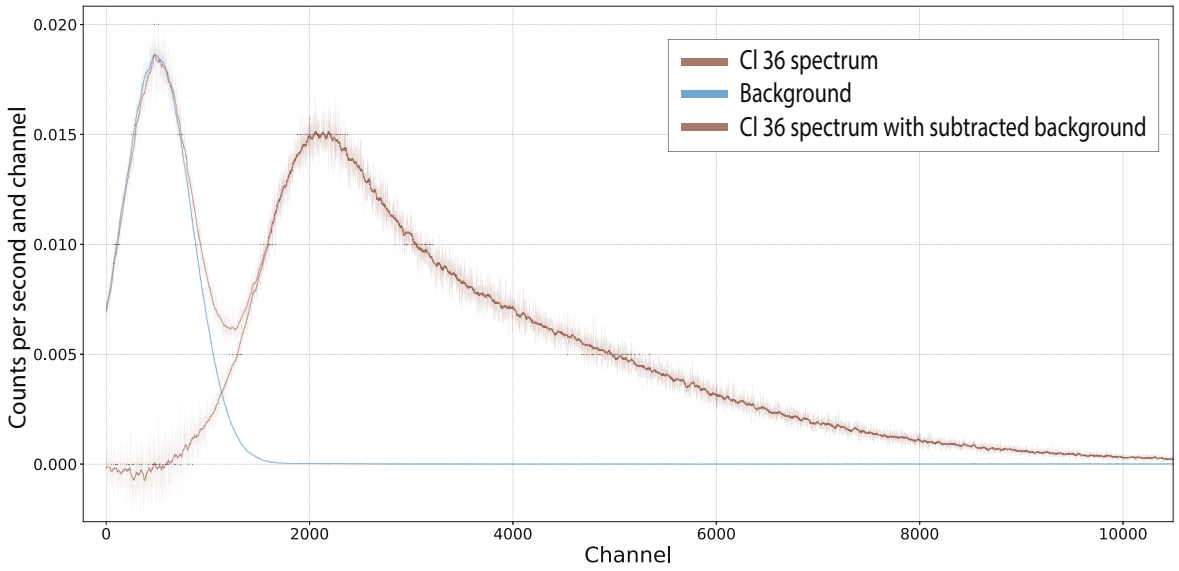

Figure 24: ^{36}Cl measured with the type 130H detector. The blue line stands for the noise. Subtracting the noise removes the leftmost peak. The noise and the sample were measured using the same settings.

The 130H amplifier and 130H detector could not be used for measurements inside the magnetic field. With a magnetic field the countrate would go down, at a certain field the measured countrate was near zero. The amplifier experienced a maximum magnetic field of 60 mT. The silicon surface barrier detector itself is not significantly influenced by a magnetic field [39]. The SA series detector in combination with the Ortec model 142 amplifier was not influenced by a magnetic field.

6.3 Results

The primary focus of this work was to characterize the effectiveness of the magnetic trap used in CREScent. This was done by measuring the number of electrons that escape the magnetic trap. The measurement setup used to achieve this consisted of the already described YSO scintillation crystal, SiPM and the MXR208A oscilloscope. The measurement setup has to be calibrated in order to determine the energy of a peak within a measured spectrum. The calibration and to what extent the measurement system is linear can be seen in section 6.3.2. Another factor that can influence the main measurement is the temperature. The temperature dependence of the scintillation crystals and the SiPMs is described in the following section.

6.3.1 Temperature Dependence of Scintillation Measurements

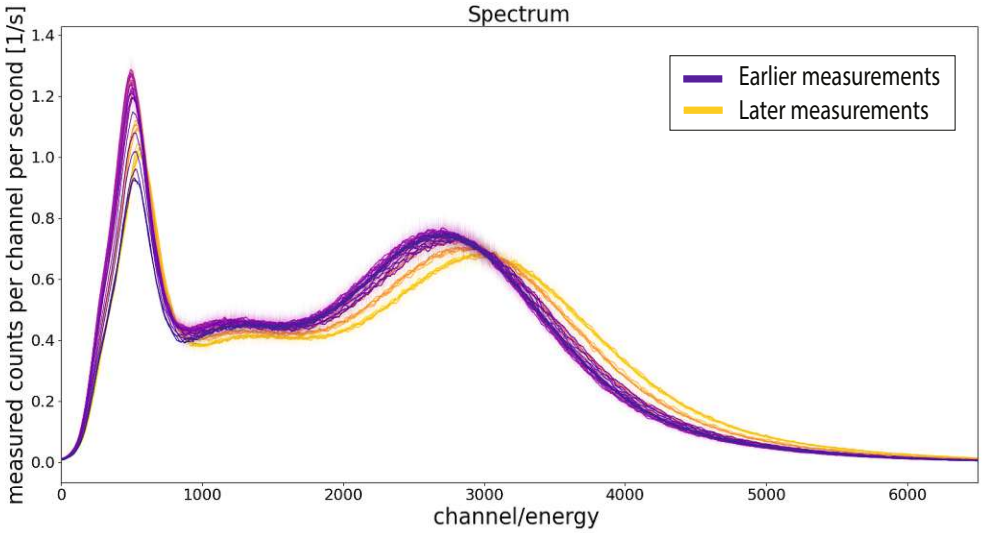

Figure 25: 40 consecutive measurements of ^{137}Cs, each measurement is 20 minutes long. The scintillation crystal is BGO. Every spectrum is colored corresponding to the time it was taken, the first spectra have a purple color which shifts to orange and ends with yellow for the final measurements. The measurement series was taken over a time of 13.3 hours. It can be seen that the spectrum changes over time. The minimum peak position of the right peak is at channel 2650, the maximum is at channel 3000.

Scintillation crystals have a temperature dependence of their light output [40]. The gain of the SiPM also depends on the temperature. In section 6.3.3 this effect is used as an explanation for the drifting spectrum. When measuring a spectrum over longer time frames it was not constant. This can be seen in a measurement series over a longer time (13h 20min) (fig. 25). To determine the exact cause behind this behavior a measurement series with spectra at different temperatures was taken. The measurement series in fig. 26 shows the changing spectrum with changing temperature. This measurement was taken by first heating the scintillation crystal together with the SiPM and then recording the spectra during the cooling back down to room temperature. Each spectrum was taken over an equal time length of two minutes. Between each recorded spectra there was a break of a few seconds. The temperature in the laboratory was not constant. The measurement in fig. 25 was taken at the ambient temperature in the laboratory.

The temperature inside the laboratory varied by as much as 2 ℃, the average temperature was 23.46 ℃. The influence of temperature can explain the originally observed drifting spectrum.

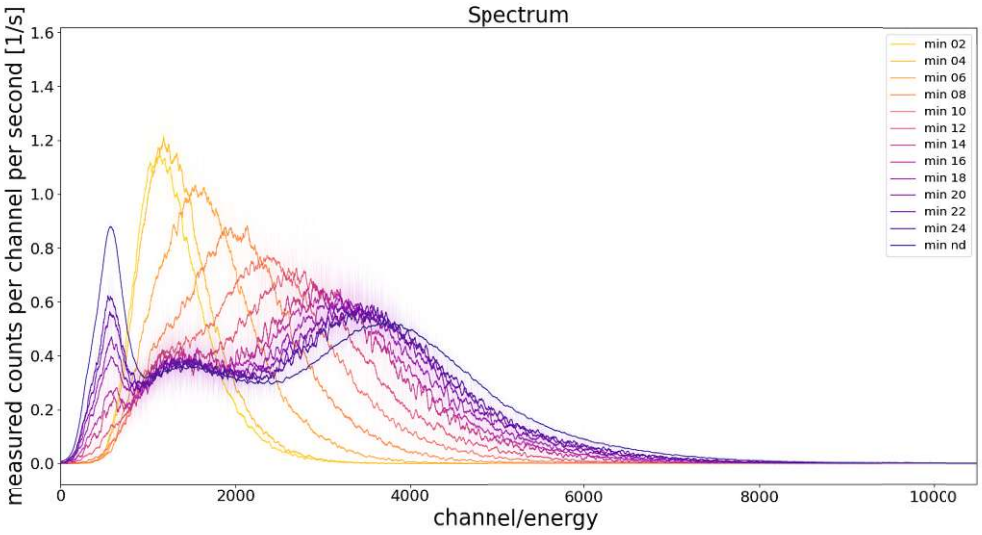

Figure 26: The changing spectrum with changing temperature. Each spectrum was taken over a time period of two minutes with a few seconds break between every recorded spectrum. The last spectrum (blue, room temperature 23.63 ℃) was recorded over a longer time frame to generate a smoother plot. All spectra were recorded using BGO as a scintillator and the GBS MCA-527 multichannel analyzer. The first spectrum yellow was recorded at an average temperature of 45.5 ℃.

To validate the results from fig. 26 the mean peak voltage after preamplification at varying temperatures was recorded using a LECROY WAVESURFER 104MXS-A 1 ghz oscilloscope (see table 5). The voltage is the mean pulse height of the full ^{137}Cs spectrum. The BGO crystal and the SiPM were heated first and the measurements were taken at specific time/temperature points during the cool down.

Temperature [℃]	Voltage [mV]
44	39
41.16	38.5
34.81	41
27.6	60
24.64	67

Table 5: The mean peak voltage from the BGO crystal and a ^{137}Cs source, measured with a LECROY WAVESURFER 104MXS-A 1 ghz oscilloscope.

Table 5 shows the same trend as fig. 26. Higher temperatures in the BGO crystal and the SiPM result in lower voltage/energy readings. To quantify the temperature behavior the energy of the ^{137}Cs peak was charted over temperature (see fig. 27).

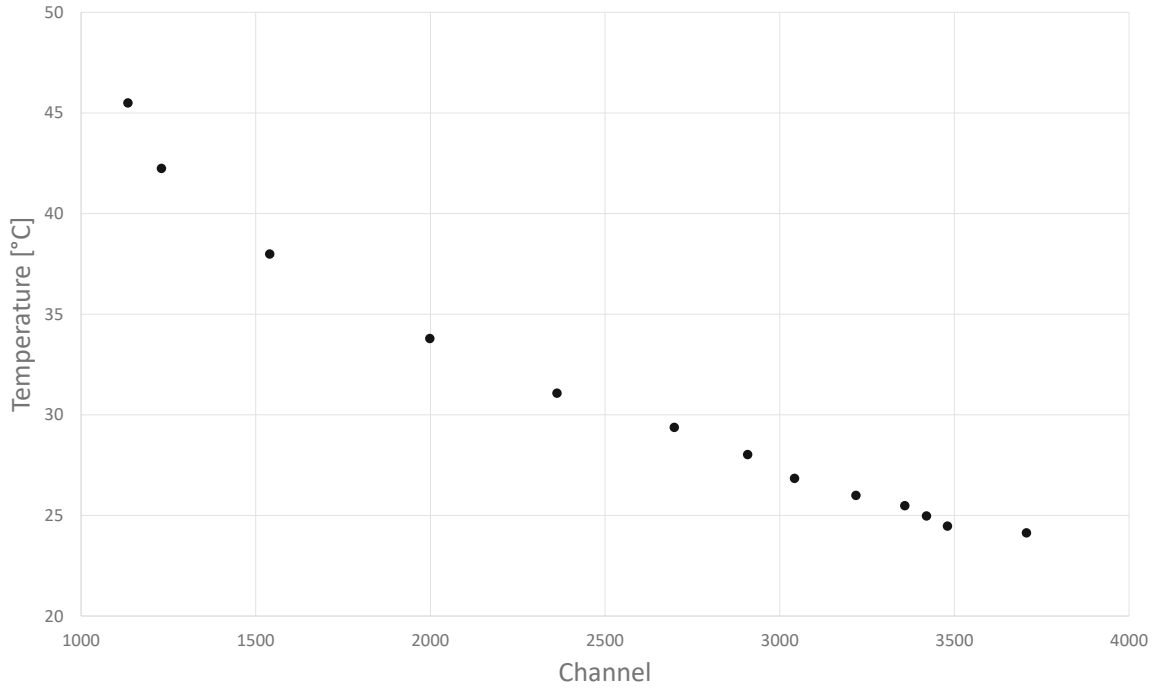

Figure 27: The position of the ^{137}Cs peak center at different temperatures. This graph is made using the same data from fig. 26. The temperature is the average between the temperature at the start and the end of a measurement. The peak position was not obtained via fitting a peak since this graph only intents to show the non quantitative behavior. Instead, only the maximum of the peak is used to serve as the peak position.

The light output and the decay times of BGO depend on the temperature [40]. From a room temperature of 23.6 ℃up to a temperature of 44 ℃a reduction of light output by 40% is typically expected [40]. The observed reduction in amplitude is higher than that, the rest of the reduction must have been from the SiPM. Since the characteristics of the SiPM also depend on the temperature [41] with higher temperatures leading to a reduction in gain. The decay times of BGO change slightly with temperature, this may have let to further distortion [42]. Unlike BGO YSO has minimal temperature drift [43]. The YSO crystal in combination with a different SiPM showed much less temperature drift. YSO was ultimately chosen to measure the spectra for determining the effectiveness of the trap.

6.3.2 Calibration of the Scintillation Measurement Setup

Birks' law is an empirical formula that describes the amount of light produced per unit distance traveled in a scintillator, based on the energy lost per unit distance by a particle moving through it. This relationship is non-linear at high rates of energy loss.

$$\frac{dL}{dx} = S\frac{\frac{dE}{dx}}{1 + kB\frac{dE}{dx}} \tag{17}$$

In the equation, $\frac{dL}{dx}$ represents the light yield per path length, $\frac{dE}{dx}$ denotes the energy loss per path length, S is the scintillation efficiency and the parameter and kB is called Birks' coefficient. The amount of light an ionizing particle produces depends on the type, doping and purity of a scintillator. It also varies with temperature and other factors. The aim of this section was to calibrate the scintillation measurement setup, in essence to measure the electron/gamma energy to energy/channel relationship. The whole system (scintillator, SiPM, amplification, readout) was calibrated. Since for example silicon photomultipliers are only linear in their response if the light level is low. Above a certain light level, the SiPM becomes saturated.

To calibrate the setup multiple different spectra with peaks of known energy were recorded. To determine the energy of a measured peak a function was fitted onto it. The fitting was done in Python, details and the various used functions are listed in appendix A.4. Ideally each spectrum has one or more well-defined peaks at different energies. It is easier to fit a function onto a well defined energy peak. But poor energy resolution meant that adjacent energy peaks were often indistinguishable. Many of the available sources listed in table 3 had multiple peaks at higher energies, the Compton edges and Compton continua would then conceal lower intensity peaks. With the available experimental setup and sources five different energy points were available to show the linearity of a crystal. Two additional points are also shown in fig. 31 but they are above the linear region of the SiPM.

As seen in fig. 28 it was not possible to fit a Gaussian distribution to a peak. ^{241}Am has no gamma peaks higher than the one shown in fig. 28 and no gamma peaks immediately below the peak at 59 keV. A skewed Gauss peak was a better fit. However, a skewed Voight profile was an even better fit especially at the relevant top of the peak. The original data was also smoothed via either a kernel regression method or a Savitzky–Golay filter.

The center of a peak fitted to the sum of a non horizontal underground and a peak is not the same as the center of a peak without underground. To determine the position of peaks within significant underground counts it can help to separate the components of the peak and the underground spectrum. In fig. 30 it was assumed that the underground spectrum is linear. Since the underground is not very steep the difference between the maximum of just the peak and the complete spectrum is minimal.

In fig. 31 all the peak/voltage references are plotted and a linear fit was applied with the additional constraint that zero energy exactly corresponds to channel zero. In this case the fitting function is: $(y(x) = k \cdot x)$, k is the slope. This linear fit was used as the energy scale on all measurements with a horizontal energy axis. A different fit without this constraint was also applied. In this case the fitting function is: $(y(x) = m \cdot x + d)$, m is the slope, d is the y intercept. Both fits line up close enough that they cannot be easily distinguished in fig. 31.

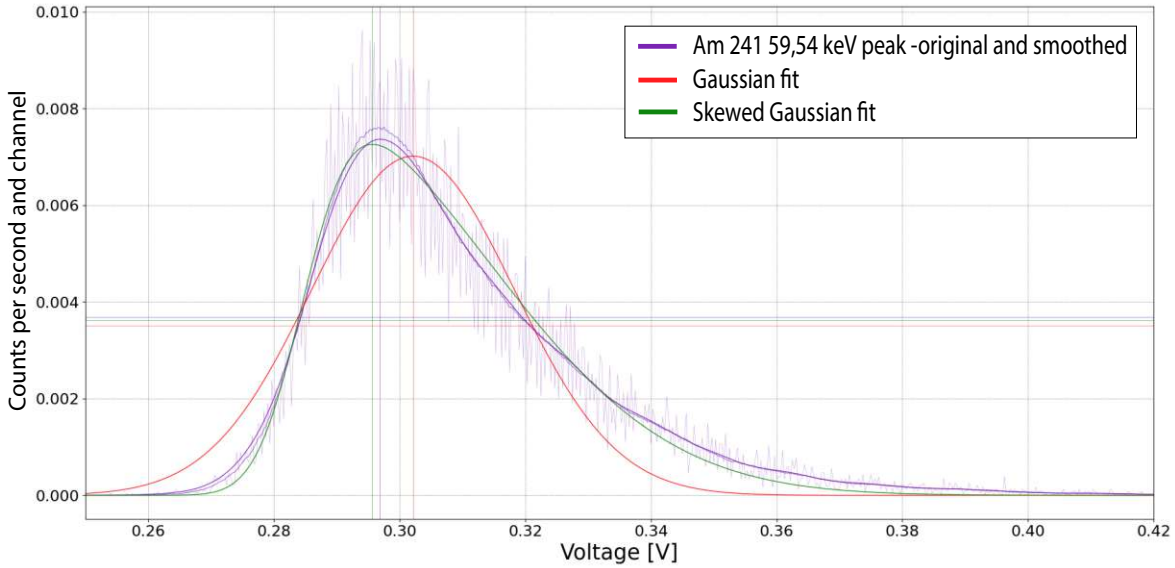

Figure 28: The ^{241}Am 59 keV gamma peak measured with the oscilloscope, YSO and the collimator. The light purple line is the original normalized peak. The smooth purple line is the peak after using kernel regression (python class: statsmodels.nonparametric.kernel regression). The slightly less smooth line is the peak after using a Savitzky–Golay filter. All of the purple lines are just the original data with various degrees of smoothing. The red lines show a Gaussian fit with the red horizontal line at half the maximum of the Gaussian. The green line shows a skewed gaussian fit. The horizontal lines are at half the maximum of a peak and the vertical lines are at the maximum of a peak. A better fit of the same peak is shown in fig. 29.

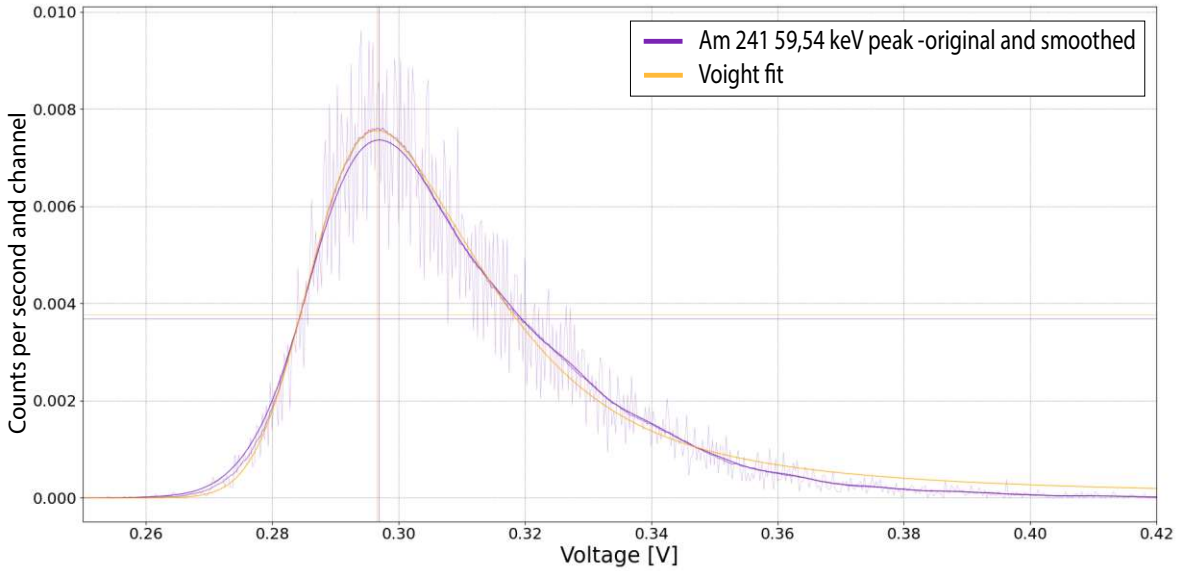

Figure 29: The same ^{241}Am peak from fig. 28 with a skewed Voight function (orange) fitted. All of the purple lines are just the original data with various degrees of smoothing. It can also be seen that two of the smoothing methods the Savitzky–Golay filter and the smooth kernel regression filter do not match up at the top of the peak. The yellow skewed Voight fit overlaps the original data after smoothing it with a Savitzky–Golay filter.

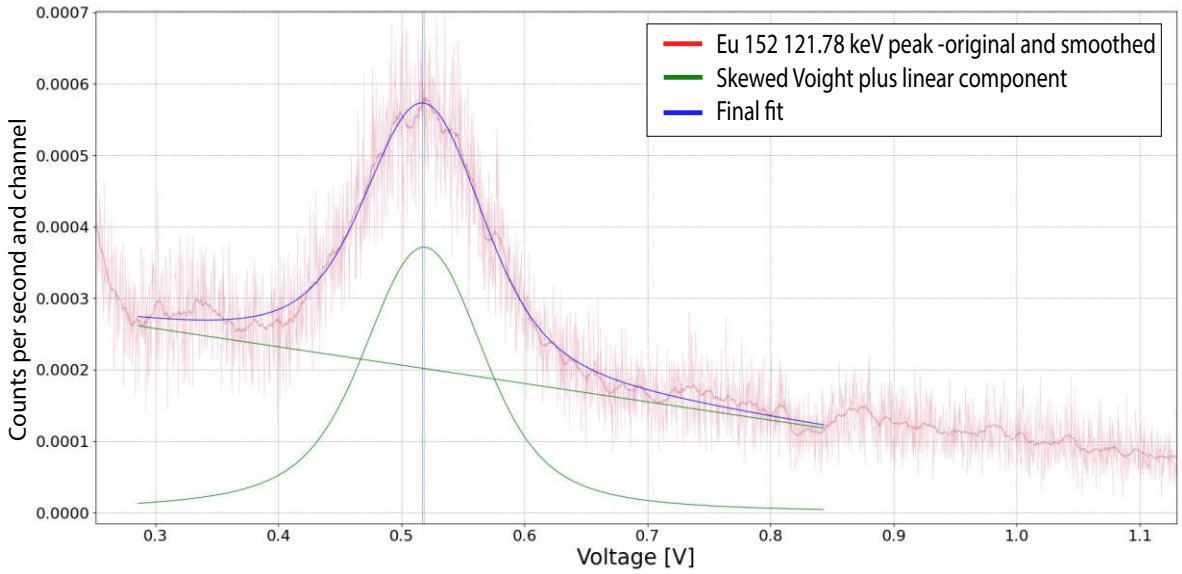

Figure 30: A section of the energy spectrum of ^{152}Eu measured with YSO, oscilloscope and collimator. The peak has an energy of 122 keV and is in the Compton continuum of higher energy peaks. The blue line is the full fit. The green lines are a linear component and a skewed Voight fit component.

The fit was performed using the least squares method. In reality the response function is not exactly linear, however the few data points and the wide standard deviations do not allow for a higher degree function to be fitted properly. In YSO the light output per unit radiation energy should not deviate by more than 10% between 100 keV and 1000 keV [28][30].

The FWHM[4] energy resolution of YSO depends on the energy, with higher energies having better energy resolution [30]. The fitted skewed Voight peak has an energy resolution of 11.35% for the 59 keV ^{241}Am peak and 10.74% for the 356 keV ^{133}Ba peak. Both of these peaks have no or no significant Compton or otherwise underground and are therefore easily analyzed.

^{198}Au produced via neutron activation from natural ^{197}Au decays via β^- emission to excited^{198}Hg which emits 412 keV gammas. This means the gamma peak is slightly concealed by the beta spectrum with an endpoint energy of 961 keV. The electrons and two low intensity higher energy gammas meant that it was not easy to identify the center of the 412 keV peak which can also be seen in the wide standard deviation of that data point.

It is expected that energies higher than a certain energy are above the linear fit line. Since at some point the SiPM gets oversaturated and no longer offers a linear gain. At this maximum voltage the same maximum voltage peak is measured independent of gamma energy. The ^{152}Eu data point in is a good example of that.

[4]Energy resolution is generally defined by the full width at half the maximum (FWHM). $FWHM \approx 2.355 \cdot \sigma$, ($\sigma$ stands for the standard deviation)

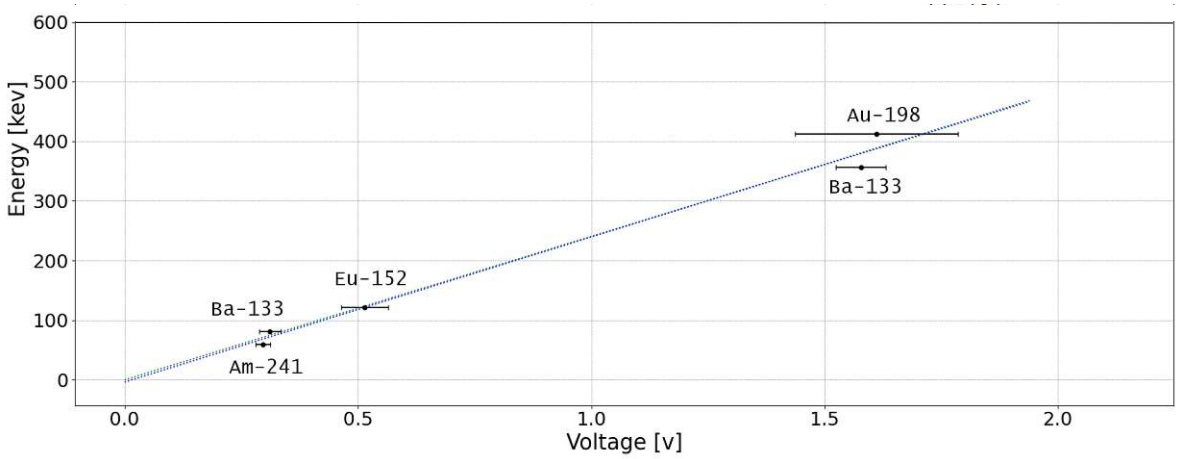

Figure 31: The energy of a peak and its corresponding voltage on the oscilloscope and YSO. The error bars show the standard deviation from the fitted curve of a peak. Two different linear fits were applied to the black data points. Both fits line up close enough that they cannot be easily distinguished.

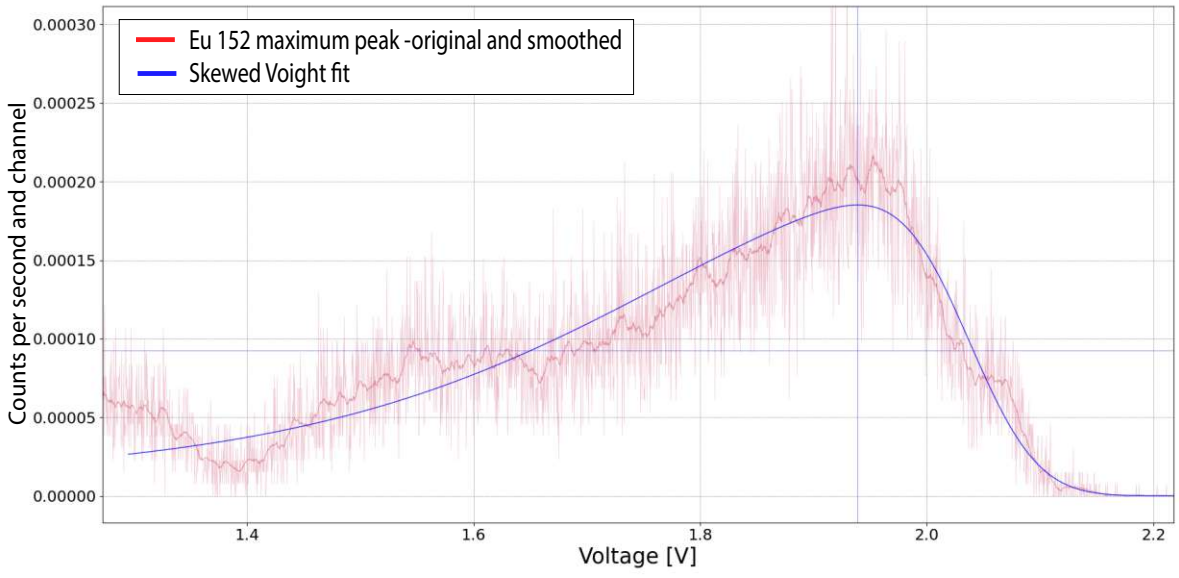

Figure 32: A section of the higher energy spectrum of ^{152}Eu measured with YSO, oscilloscope and collimator. ^{152}Eu has multiple peaks above the maximum detectable energy with this SiPM and YSO (778.9, 964.08, 1085.9, 1112.1, and 1408 keV).

6.3.3 The Influence of the Trap Field

To measure the effectiveness of the trap field a scintillation detector was positioned on one side outside of the electron trap. Electrons that escape the trap field on that side were then measured. The scintillation crystal was placed exactly in the path of the electrons, the front of the scintillation crystal was in axial direction 190 mm away from the center and pointing directly at the source. The detector was placed very close to the end of the electron trap. The reason why the detector was placed this close was the gyration radius. At for example 1 T 482 keV electrons would have a gyration radius of 3.31 mm. The electrons should therefore be within a 6.62 mm radius circle, electrons with lower pitch angles and less energy perpendicular to the magnetic field have an even smaller gyration radius. Further away from the trap at a lower magnetic field strength the electrons have a larger gyration radius and therefore potentially miss the (4 x 4) mm front of the scintillation crystal. In previous measurements it was verified that the SiPM and the rest of the setup are not influenced by the magnetic field[5].

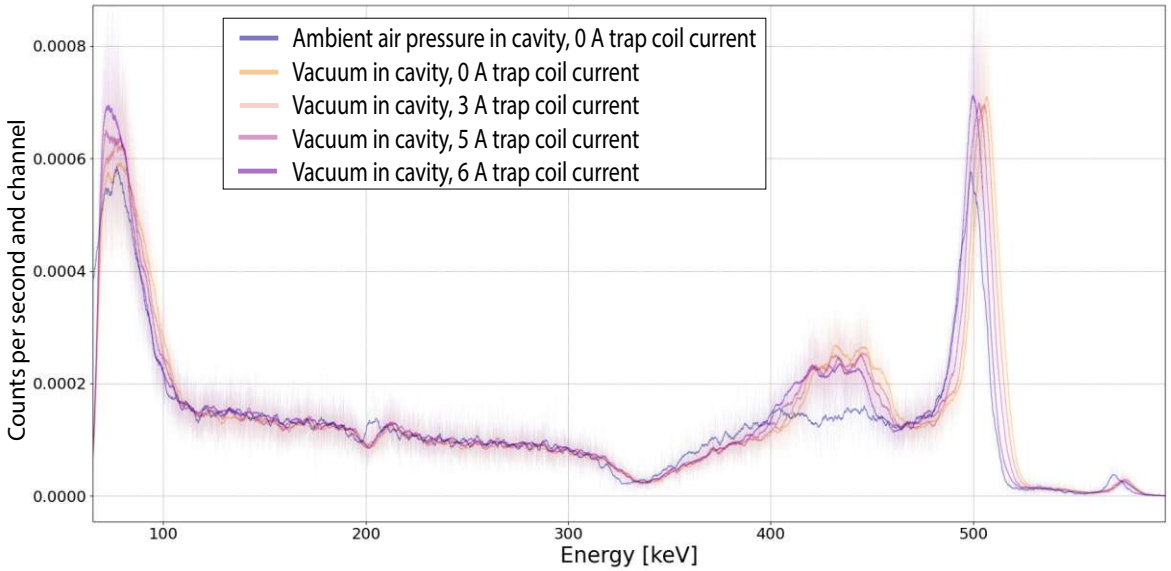

Figure 33: Measurements of ^{207}Bi inside the magnetic field (215 mT) to show the electron countrate as a function of the trap coil current and the vacuum. The spectra were measured with YSO the collimator and a MXR208A oscilloscope. The light blue spectrum was measured without any current in the trap coils and therefore no trap field, it was measured at ambient air pressure inside the cavity. All other measurements were measured with a vacuum in the cavity the trap coil currents varied from 0 A- orange, 3 A-light pink, 5 A-dark pink to 6 A-magenta. For the horizontal axis the fit from section 6.3.2 is used to show the energy.

In fig. 34 it can be seen that this peak wanders towards the left/lower energies with increasing current. Both trap coils would dissipate waste heat of 1.43 W at 3 A up to 5.73 W at 6 A. The resulting temperature increase can explain the shift in the spectra.

conversion electrons at ambient air pressure are largely absorbed before reaching the detector especially considering that in the magnetic field they travel in a spiral path. This means that the spectrum measured at ambient air pressure in fig. 33 was generated by photons. The spectra measured in a vacuum consist of both photons and electrons. The difference between vacuum and ambient air pressure spectra is the pure electron component.

[5]Theoretically the magnetic field should influence the electron spectrum as shown in section 7.1.

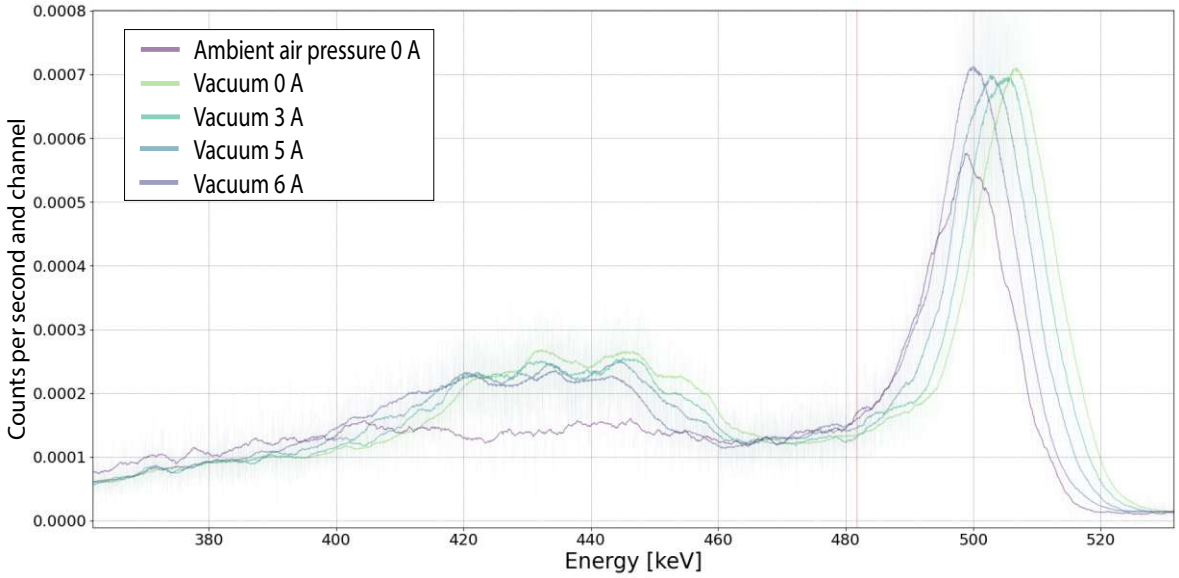

Figure 34: A magnified region of the upper energies from fig. 33. The current in the trap coils is color graded from light blue corresponding to 6 A to light green for no current. The red vertical line is at 482 keV which is the position of a higher intensity ^{207}Bi conversion electron peak table 4. It can be seen that the peak at 500 keV (and the rest of the spectrum) is on a slightly different position on every spectrum.

Focusing on just the region of the electron peak between 392 keV and 471 keV and subtracting the photon counts in that region gives an electron countrate of 5.673 cps with no current in the shim coils (and thus no trap field). At a shim coil current of 3 A 83.72% of this countrate was measured, at 5 A 77.30% and at 6 A 69.56% of the no trap countrate was measured. This relationship is again plotted in fig. 36. This suggests that the trap-field is preventing electrons from reaching the detector and is effective in trapping the electrons. Moreover, a stronger trap field confines more electrons reducing the measured electron countrate. Other measurements have shown that the countrate of the measurement setup itself is not influenced by temperature. Suggesting that the different countrates are indeed caused by the trap field. Furthermore the region between 392 keV and 471 keV is wide enough that all peaks are within it, even if they are shifted by different temperatures.

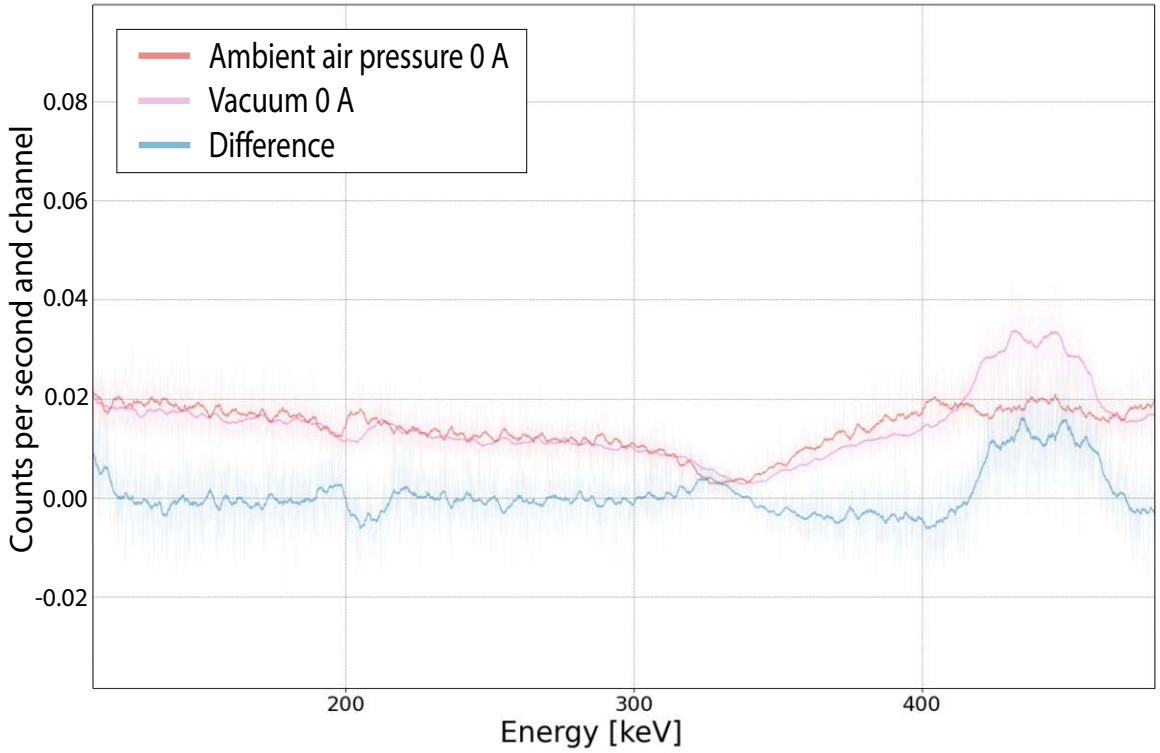

Figure 35: ^{207}Bi inside the magnetic field (215 mT), spectra measured with YSO the collimator and a MXR208A oscilloscope. The red spectrum was measured in ambient air pressure and no trap field. The pink spectrum was measured in vacuum and also without a trap field. The blue spectrum is the difference between the other two spectra. The peaks around 500 keV and 70 keV are at slightly different positions (possibly because of different temperatures, the temperatures were not known) which leads to a big peak and valley in the difference spectrum. The peak at 440 keV in the difference spectrum is from electrons and its height decreases with increasing trap field strengths.

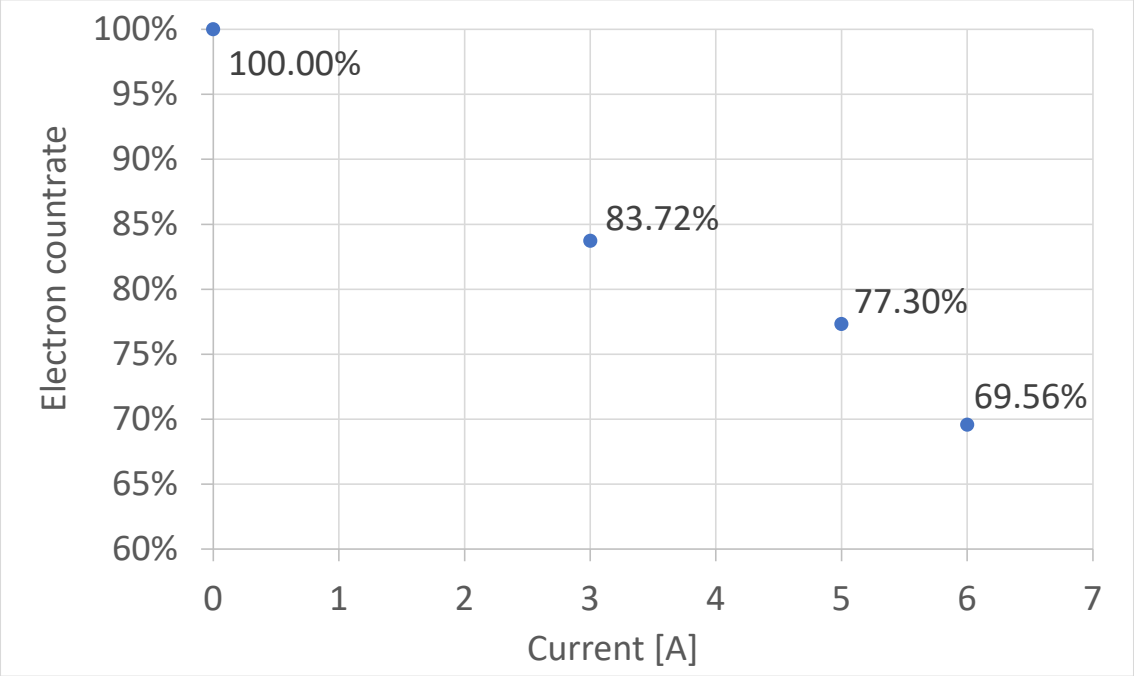

Figure 36: The electron countrate in relation to the current in the trap coils. It can be seen that a higher current in the trap coils reduces the electron countrate. The values are obtained by first subtracting the spectrum measured in ambient air pressure (photon spectrum) from each spectrum measured in vacuum. Then the counts in a region between 392 keV and 471 keV are used for the electron countrate. The electron counts at 0 A are defined at 100% the electron counts at 3 A, 5 A and 6 A are given as a percentage of the 0 A counts.

7 Discussion and Conclusions

The ^{207}Bi electron peak from fig. 34 is centered at 439 keV. This is slightly below the energy of the 482 keV conversion electron peak. This lower than expected energy can be explained by the non linearity of the measurement setup. The calibration showed that at energies of the 482 keV electron peak the measurement setup is already nonlinear and above a certain energy the measurement setup can no longer measure any higher energies. A potential explanation for this behavior is that the SiPM gets oversaturated and is therefore no longer able to count excess photons.

The peak below 100 keV in the measurements of ^{207}Bi in fig. 33 should consist of multiple X-ray photons with energies from 9 keV up to 88 keV and one higher intensity component at 74 keV. The maximum or center of this peak depends on the threshold energy since only the higher energy tail is captured. Counts below energies of about 70 keV were no longer above the threshold energy and were not included in the spectrum. The peak around 500 keV is at the maximum detectable energy with the used SiPM. It consists of all higher energy photons and electrons. In the measurements it can be seen that the intensity of the peak around 500 keV decreases in ambient air pressure suggesting that the peak in vacuum consists of both electrons and photons. A detailed description of this is given in section 6.3.3. The energy resolution of the electron peak at 439 keV was determined by fitting a skewed Voight profile to the pure electron peak. The measured energy resolution of the ^{207}Bi electron peak is 7.32% FWHM. This measured energy resolution is roughly in the same range as the expected energy resolution[6].

In the magnetic field the isotropically emitted electrons no longer move in a straight line, instead they have trajectories as described in section 1.1.5. To determine the expected countrate for electrons, eq. (15) and eq. (16) can no longer be applied. The electrons are concentrated around a central axial line. With higher distance between source and detector the countrate from electrons stays approximately constant. Without any other influences the photon countrate should decrease with approximately distance^{-2}. The measured photon countrate was higher than expected for the distance and ^{207}Bi activity. The photons are not influenced by the magnetic field but they can be scattered of the vacuum chamber walls.

Electrons confined within the trap lose energy by emitting cyclotron radiation or they may also interact with residual gas molecules. The pressure measured at the vacuum pump inlet was 10^{-6} mbar, the pressure inside the vacuum chamber was not directly measured.In chapter section 6.3.1 the influence of the temperature on the measurement setup is discussed. The temperature dependence is caused by both the scintillation crystal and the SiPM. The peaks in the measurements seen in fig. 34 do not line up. This behavior can be explained by different temperatures. With increasing current in the coils and therefore increasing temperature the peak around 500 keV gets shifted towards lower energies. This is the behavior expected with an increasing temperature (see section 6.3.1). The spectrum taken in ambient air pressure was taken without a trap field; there was no resistive heating that could have elevated the temperature. The ambient air spectrum is shifted towards lower energy values without any known temperature rise, this behavior is unexplained. It was not known what the actual temperature of the scintillation crystal and the SiPM was, since it was not possible to fit a temperature sensor on them inside the vacuum chamber.

[6]For YSO the expected energy resolution is 9.4% FWHM of the 662 keV peak [30]. The energy resolution of YSO depends on the energy, with higher energies having better energy resolution [30].

7.1 Simulating the Spectrum in the Magnetic Field

When interpreting the measured electron peak it has to be considered that the electrons in the magnetic field strike the scintillation crystal at varying incidence angles. 482 keV electrons arriving perpendicularly have a backscattering coefficient of 0.134 in YSO (see fig. 37). If however, the electrons strike at a shallow angle, the probability that an electron exits the crystal increases as seen in fig. 8. Every electron that leaves the crystal does not deposit the entire energy and will therefore show up as a lower energy count.

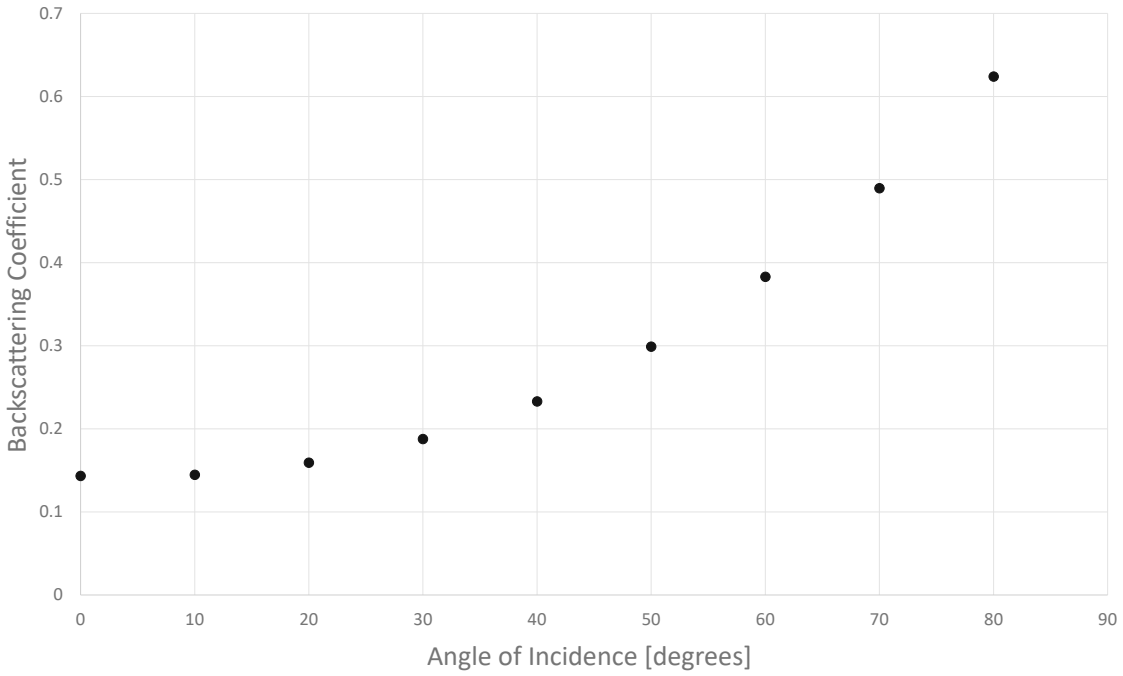

Figure 37: The backscattering coefficients of 482 keV monoenergetic electrons in YSO at different incidence angles. This graph was created by simulating the paths of 10^5 electrons per angle of incidence in the program: "CASINO Monte Carlo Software" [14]. All simulations were created without any background magnetic field. An angle of incidence of 0 means perpendicular incidence and for perpendicular incidence the backscattering coefficient is 0.143.

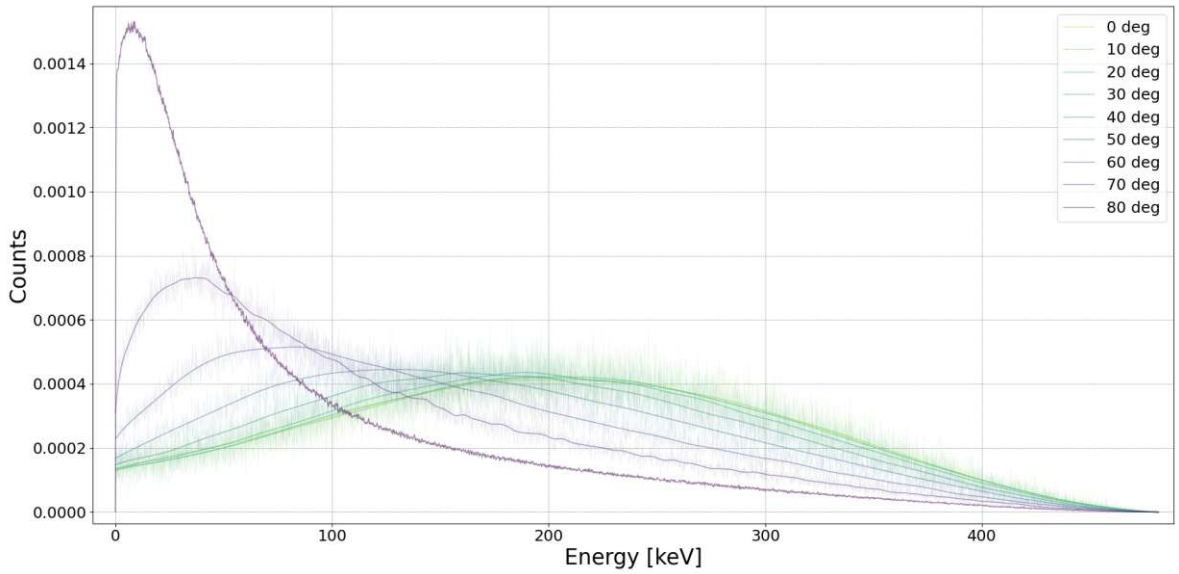

Figure 38: The energy deposited in the crystal by backscattered electrons. The data was created from the simulations of YSO for 482 keV electrons at various angles of incidence in (see fig. 37). The data is smoothed using kernel regression (python class: statsmodels.nonparametric.kernel regression). The graphs were created by simulating the paths of electrons each in the program: "CASINO Monte Carlo Software" [14].

To predict the influence of the magnetic field on the electron spectrum three things have to be known.

- The backscattering coefficient for every incidence angle. The backscattering coefficient over angle of incidence can be seen in fig. 37.
- The spectrum of the deposited energy for an incidence angle (energy deposition distribution). The energy deposition distribution of backscattered electrons can be seen in fig. 38.
- The number of electrons per incidence angle. The pitch angle for every electron changes with a changing magnetic field. The initial pitch angle distribution is seen in fig. 39 and the evolution of the pitch angles with changing magnetic field is seen in fig. 40.

The number of electrons per incidence angle is obtained by first assuming that the pitch angle is distributed as would be expected from an isotropically emitting point source. As the magnetic field changes so does the pitch angle. Electrons starting in a high magnetic field will decrease their pitch angle as they enter a lower magnetic field as seen in fig. 40.

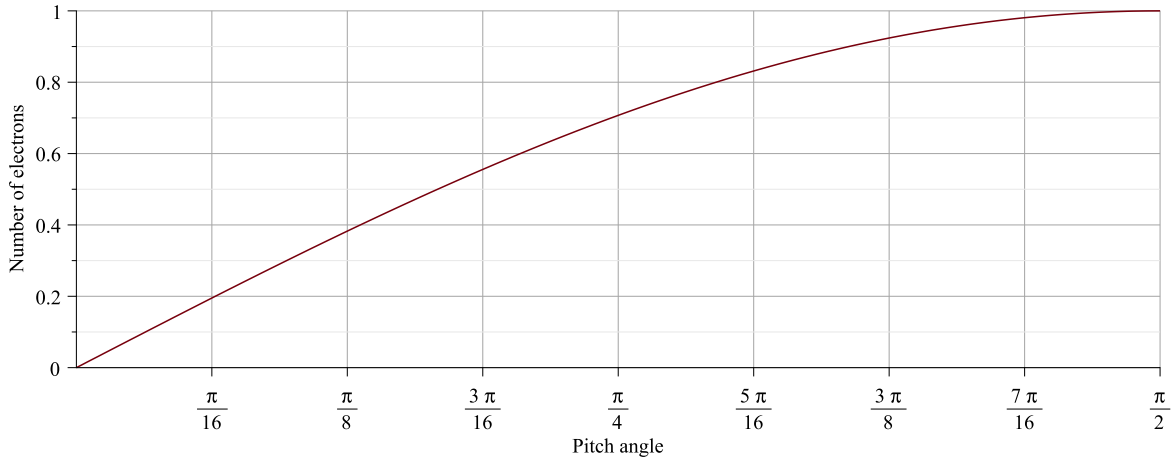

Figure 39: The initial pitch angle θ of an isotropically emitting point source. The pitch angle distribution is proportional to $sin(\theta)$. It can be seen that few electrons have a small pitch angle and the most common pitch angle is 90 degrees.

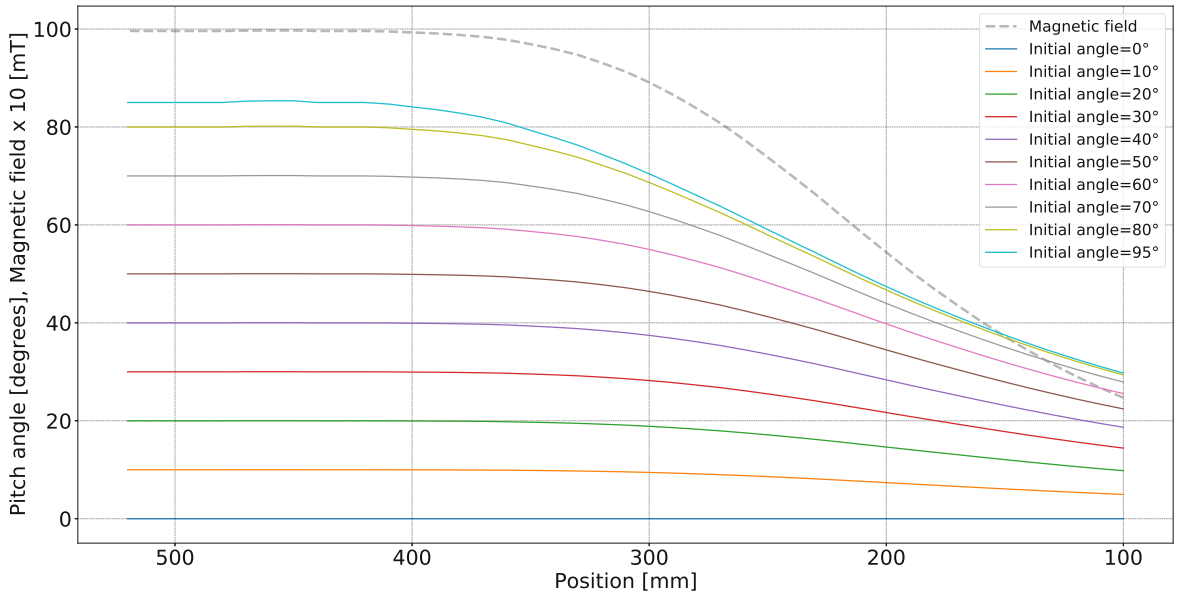

Figure 40: The pitch angles of 482 keV electrons as they change in the magnetic field. The grey dotted line represents a measurement of a background field starting at 1T and is the basis for determining the pitch angles. This graph was created using eq. (11).

To simulate the electron spectrum in the magnetic field the spectrum of the deposited energy for an incidence angle is multiplied by the number of electrons in a 10 degree pitch angle window and divided by the backscattering coefficient for that pitch angle. Then all the different 10 degree pitch angle window partial spectra are summed up for the full spectrum[7]. The partial spectra are indicated in fig. 41 by their light shade. The simulated spectrum in fig. 41 is only an approximation to simplify the process, it is assumed that one spectrum of the deposited energy and one backscattering coefficient is representative for the whole 10 degree pitch angle window. Also, the energy resolution of the detector is neglected for the backscattered fraction. The main peak of 482 keV was assumed to be Gauss shaped with an energy resolution of 9.4% (FWHM). In the simulated spectrum in fig. 41 the source and the detector are at the same magnetic field strength of 1 T. Therefore, the pitch angle is distributed as expected from an isotropically emitting point source. If the detector were in a different magnetic field than the source the changing pitch angles would have to be considered.

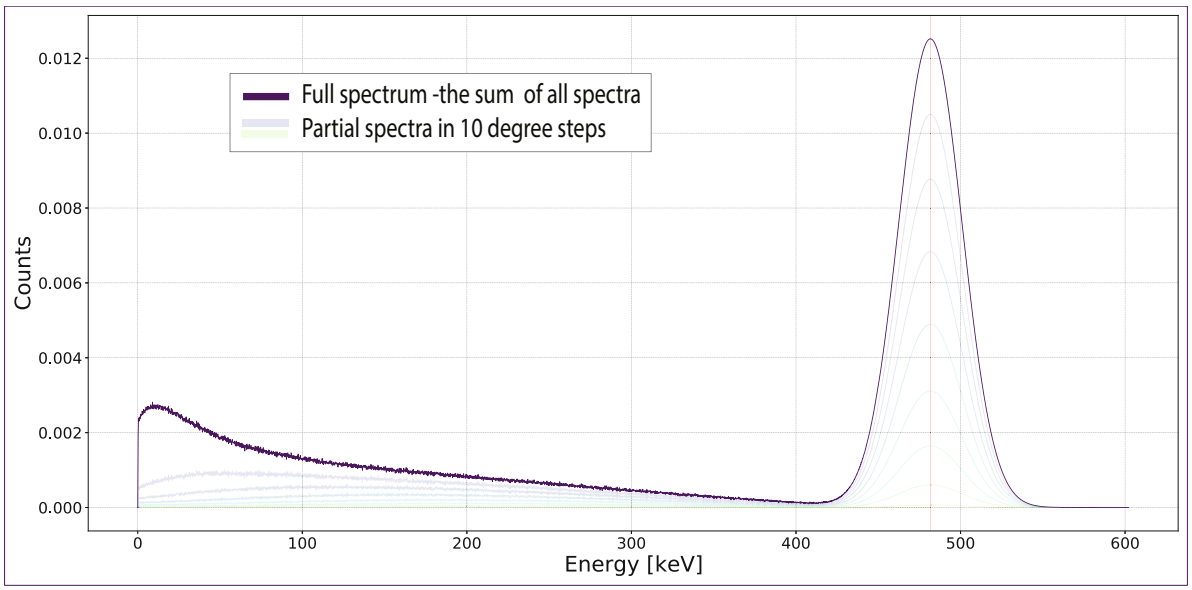

Figure 41: The expected spectrum from monoenergetic 482 keV electrons with YSO in a 1 T magnetic field. The energy resolution of 9.4% in YSO results in the main peak at 482 keV becoming Gauss shaped. 482 kev was chosen because ^{207}Bi has an electron peak at 482 keV. The lighter lines indicate the contributions of the various pitch angles starting at 10 degrees. In this graph the detector and source are at the same 1T magnetic field. This spectrum is only an approximation because the energy resolution of the detector is neglected for the backscattered fraction. And all possible incidence angles within 10 degrees are reduced to one representative angle and distribution.

In fig. 41 it can be seen that the full energy electron peak still dominates over the backscattered electrons. In the magnetic field the intensity of the main Gauss shaped peak is reduced slightly and the backscattered electrons show up as lower energy counts. Without a magnetic field only the main Gauss shaped peak at 482 keV would be visible and it would be slightly higher. In fig. 41 the scintillator is YSO, the backscattered fraction would increase for scintillators with higher density, such as BGO. The effects of backscattering on the electron spectrum are not really observed in the measurements of section 6.3.3 because of multiple reasons. First, the small contribution is eclipsed by the photon background. Secondly, in the predicted spectrum in fig. 41 the detector is placed in the same magnetic field of 1 T as the source. In this case

[7]This explanation is a simplification, in the real simulation for fig. 41 the reduction of the intensity of the main Gauss peak is also considered.

the backscattered fraction is at its maximum and the effect of a magnetic field on the spectrum is also maximized. However, all measurements in section 6.3.3 were made with the detector front face placed at a position 190 mm from the source. At this position the magnetic field and the pitch angle decrease resulting in a lower backscattered fraction and a lower influence on the spectrum.

In summary the electrons in the magnetic field hit the scintillation crystal at different incidence angles. If the electron hits the crystal at a shallow angle, the probability of the electron leaving the crystal and appearing as lower energy count increases. The resulting spectrum from this effect can be predicted using the incidence angle distribution, the backscattering coefficients for each incidence angle and the energy deposition distribution for each incidence angle. The outcome of the predicted spectrum for YSO is that main peak still dominates over backscattered electrons.

A Appendices

A.1 The Magnetic Field

The details of characterizing and homogenizing the magnetic field are discussed in a preceding work [4]. A brief overview of the "shape" of the magnetic field is given again in fig. 42.

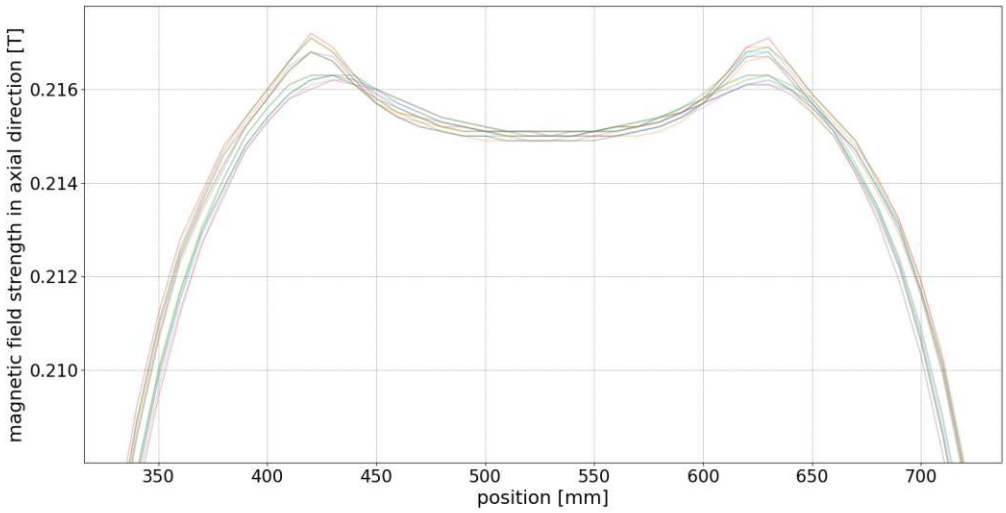

Figure 42: The axial magnetic field components at every xy-position measured with the Bell 6010 Hall Effect Gaussmeter. Measured at 215 mT with the trap field switched on. This plot intends to show the varying trap field component. The trap field increases with increasing radius from the central xy-position.

A.2 Other Surface Barrier Detectors

Additional detectors were available besides the detectors mentioned in section 4.1. However, it was not clear whether they were still functional or if they could be put back into operation. The additional surface barrier detectors were one of the following models: Ortec CR-25-450-100 serial No. 17-077H, EG&G Ortec S-A-450 serial number 29-265B. The two S-A-450 detectors were identical in construction. The two S-A 450 detectors and the CR-25-450-100 detector were part of the R Series Ruggedized Partially Depleted Silicon Detectors by Ortec (Oak Ridge Tenn., USA) and all R series detectors had an active surface area of 450 mm^2. The guaranteed maximum beta resolution of the Ortec CR-25-450-100 detector was specified at 17 keV. Besides the mentioned specifications no other specifications of the detectors were known. The detectors were over 30 years old and consultation with the manufacturer did not reveal any additional specifications. Ultimately only one detector the type 130H was fully functional. The EG&G Ortec S-A-450 serial number 29-265A was functional but the detector eventually failed. The other detectors were no longer able to produce a usable signal.

A.3 Surface Barrier Detector Setup

The measurement setup consisted of a surface barrier detector which was one of the following models: Ortec 130H or EG&G Ortec S-A-450 serial number 29-265A or a detector listed in appendix A.2. The S-A 450 detector was part of the R Series Ruggedized Partially Depleted Silicon Detectors by Ortec (Oak Ridge Tenn., USA) and had an active surface area of 450 mm^2. The 130H detector had a surface area of 104 mm^2. Besides the mentioned specifications no other specifications of the detectors were known. The detectors were over 30 years old and consultation with the manufacturer did not reveal any additional specifications. Crucially the bias voltage which determines the thickness of the depletion layer was also not known.

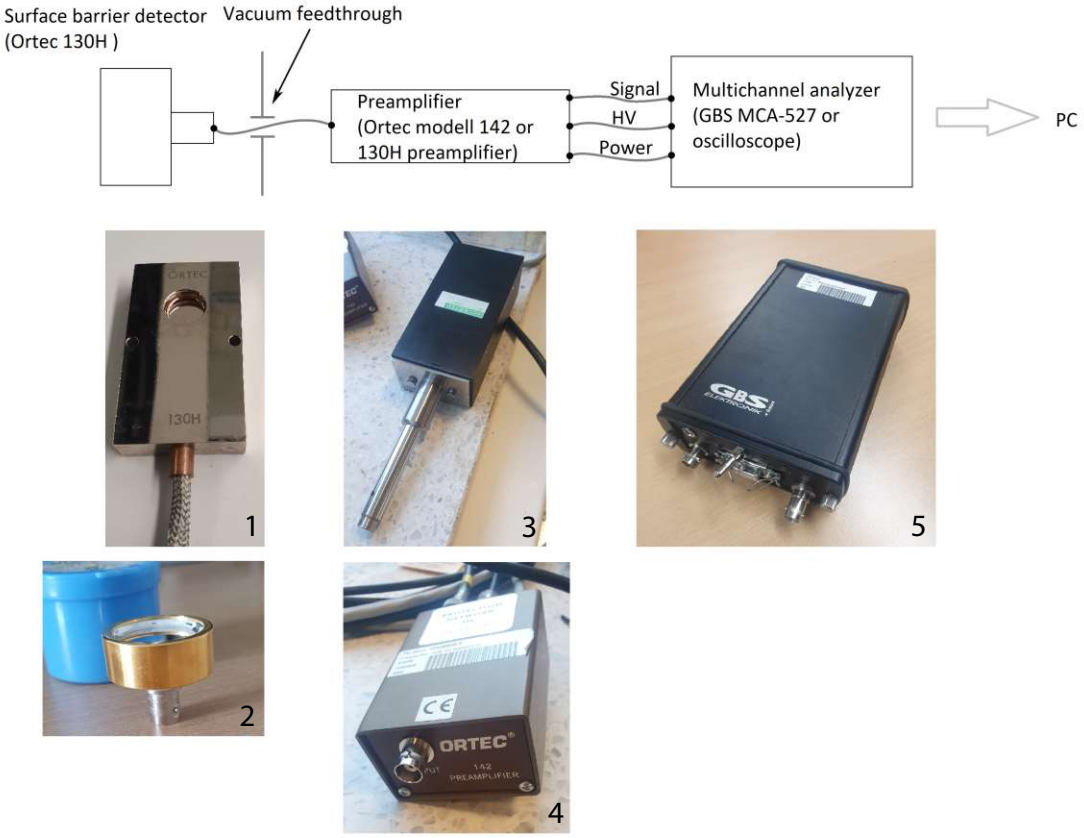

Figure 43: The surface barrier detector signal chain. Picture 1 shows the type 130 H detector. Picture 2 shows the S-A 450 detector. Picture 3 shows the 130H preamplifier. Picture 4 shows the Ortec model 142 preamplifier. Picture 5 shows the GBS MCA-527 Multichannel analyzer.

A detector inside the vacuum chamber was connected to one of two preamplifiers with a vacuum feedthrough in between. The Ortec 130H type detector was only compatible with the 130H preamplifier. All other detectors used the Ortec model 142 preamplifier. The preamplifiers were connected to the GBS MCA-527 Multichannel analyzer and for some measurements to an oscilloscope (Tektronix TDS 2024C). The GBS MCA-527 Multichannel analyzer also provided the bias voltage and power for the preamplifier. The type 130H preamplifier included an integrated vacuum feedthrough and the amplifier had to be mounted directly to the vacuum chamber wall. This meant the 130H preamplifier was in a high magnetic field on certain measurements.

A.4 Fitting Functions and Filters

In the data analysis the goal was always to determine the true position of a peak as accurately as possible. To achieve this, multiple fitting functions were used and compared. Every fitting function used is described in this chapter.

Gaussian fit function and its parameters:

$$f(x) = A \exp\left(-\frac{(x-\mu)^2}{2\sigma^2}\right) + C \tag{18}$$

where A is the amplitude, μ is the mean or center of the Gaussian, σ is the standard deviation or spread of the Gaussian and C is a constant term representing the baseline or offset of the function.

The skewed Gaussian fit function and its parameters:

$$f(x) = A \exp\left(-\frac{(x-\mu)^2}{2\sigma^2}\right)\left[1 + \operatorname{erf}\left(\frac{\alpha(x-\mu)}{\sigma\sqrt{2}}\right)\right] + C \tag{19}$$

where A is the amplitude, μ is the mean or center of the Gaussian, σ is the standard deviation or spread of the Gaussian, α represents the skewness parameter, erf denotes the error function which introduces the skewness to the Gaussian distribution and C is a constant term representing the baseline or offset of the function.

The Voigt profile is a probability distribution given by the convolution of a Cauchy-Lorentz distribution and a Gaussian distribution. The Voigt profile and its parameters:

$$f(x) = \frac{A}{\sigma\sqrt{2\pi}} \int_{-\infty}^{\infty} \exp\left(-\frac{(x-\mu')^2}{2\sigma^2}\right)\left[1 + \operatorname{erf}\left(\frac{x-\mu}{\sigma\sqrt{2}}\right)\right], \mathrm{d}x + C \tag{20}$$

where A is the amplitude, μ is the mean or center of the Gaussian component, σ is the standard deviation or spread of the Gaussian component, μ' is the center of the Lorentzian component, erf denotes the error function and C is a constant term representing the baseline or offset of the function. The integral represents the convolution of the Gaussian and Lorentzian components.

The skewed Voigt function and its parameters:

$$f(x) = \frac{A}{\sigma\sqrt{2\pi}} \int_{-\infty}^{\infty} \exp\left(-\frac{(x-\mu')^2}{2\sigma^2}\right)\left[1 + \operatorname{erf}\left(\frac{\alpha(x-\mu)}{\sigma\sqrt{2}}\right)\right], \mathrm{d}x + C \tag{21}$$

where A is the amplitude, μ is the mean or center of the Gaussian component, σ is the standard deviation or spread of the Gaussian component, μ' is the center of the Lorentzian component, α represents the skewness parameter, erf denotes the error function and C is a constant term representing the baseline or offset of the function.

Filters like kernel regression (python class: statsmodels.nonparametric.kernel regression) or the Savitzky–Golay filter are also mentioned. These filters are not used in any data analysis. They are simply used to smooth the data to make it visually more appealing or make it easier too see a peak.

A.5 Decay Schemes

In this section all the decay schemes of the mentioned isotopes are shown. The decay schemes of ^{241}Am and ^{152}Eu are not shown because both elements have many energy levels and the decay schemes would take up too many pages. Furthermore, for every mentioned isotope there is a table with all important energies listed. The tables usually also list the energies of unstable daughter nuclides. In the energy tables the column on the very right denotes the uncertainty of the intensity[8].

Decay Mode: β^-	Half-Life:(2.093E06 ± 1.5E04) d		
Radiation Type	Energy (keV)	Intensity (%)	
β^-max	156.48	100	--
β^-av	49.44		

Figure 44: All ^{14}C energies with an intensity high enough to mention it [44].

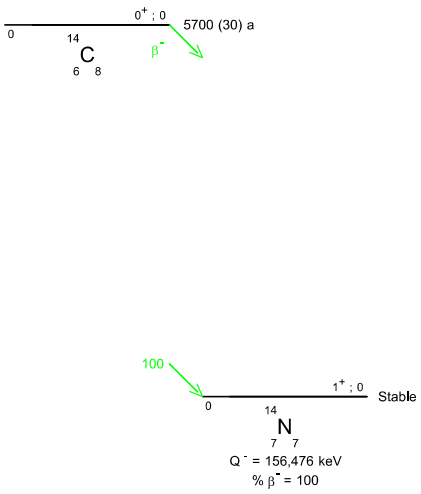

Figure 45: The decay scheme of ^{14}C [45].

[8]The format of the uncertainty illustrated by the following example: 1.2 56 = 1.2 ± 5.6

Decay Mode: β^-	Half-Life: (10523 ± 35) d		
Radiation Type	**Energy (keV)**	**Intensity (%)**	
β^-max	546	100	--
β^-av	196		

Figure 46: All energies emitted by ^{90}Sr energies with an intensity worth mentioning [44]. ^{90}Sr decays to ^{90}Y.

Decay Mode: β^-	Half-Life: (2.671 ± 0.004) d		
Radiation Type	**Energy (keV)**	**Intensity (%)**	
ec-KLMN	1742.7	0.013	7
β^-max	523.2	0.016	7
β^-av	188		
β^-max	2283.9	99.984	7
β^-av	939		

Figure 47: All energies emitted by ^{90}Y energies with an intensity worth mentioning [44].

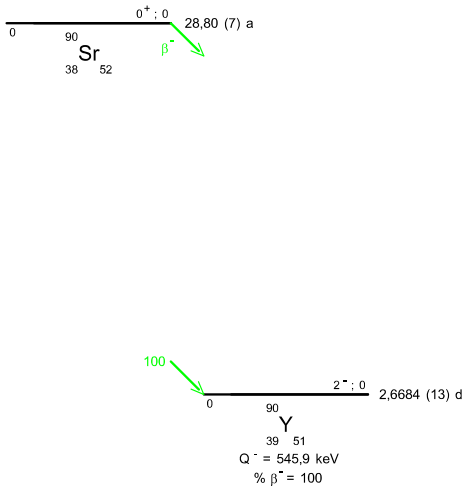

Figure 48: The decay scheme of ^{90}Sr [45]. ^{90}Sr is an isotope that decays emitting an electron with an endpoint energy of 546 keV (beta decay) into ^{90}Y. Which also decays through beta decay with an endpoint energy of 2274 keV into ^{90}Zr. The decay scheme of ^{90}Y can be seen in fig. 49.

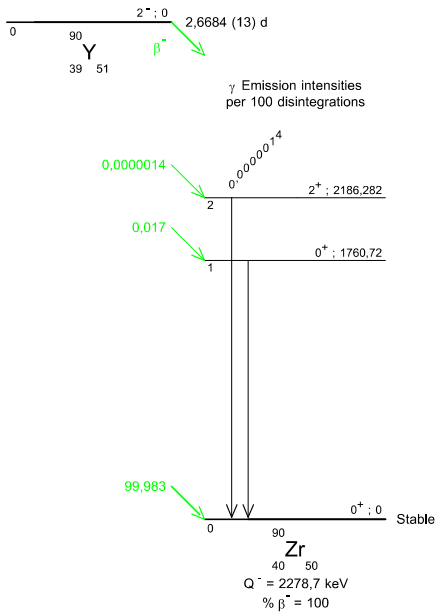

Figure 49: The decay scheme of ^{90}Y [45].

Decay Mode: β⁻, EC	Half-Life: (301000 ± 2000) y		
Radiation Type	**Energy (keV)**	**Intensity (%)**	
Auger-K	2.10	1.58	9
β⁻max	709.3	98.10	10
β⁻av	251.23		
X-ray K Σ	2.31	0.133	10

Figure 50: All energies emitted by the ^{36}Cl source energies with an intensity worth mentioning [44].$\sum$ signifies weighted mean energies and intensities, EC stands for electron capture.

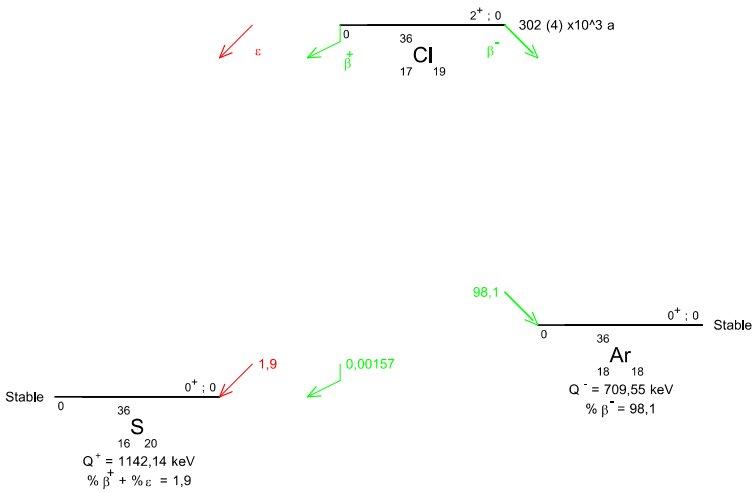

Figure 51: The decay scheme of ^{36}Cl [45]. The red arrow indicates electron capture decay.

Decay Mode: β^-		Half-Life: (11000 ± 90) d	
Radiation Type		**Energy (keV)**	**Intensity (%)**
Auger-L		2.6 - 5.9	7.28 12
Auger-K		25.31 - 37.41	0.76 4
ce-K-1		624.22	7.62 19
ce-L-1		656.0	1.42 19
ce-MN-1		661.0	0.33 1
β^-max		513.97	94.36 28
β^-av		174.3	
β^-max		1175.6	5.64 28
β^-av		416.3	
X-ray L	Σ	4.7	0.90 5
X-ray Kα	Σ	32.06	5.53 10
X-ray Kβ	Σ	36.6	1.321 27
γ	Ba-137m	661.66	85.00 20

Cs-137 with Ba-137m (half-life: 2.552 m) in equilibrium

Figure 52: All energies emitted by the ^{137}Cs source with an intensity worth mentioning [44]. ce-K-1 for example, stands for K-shell conversion electron transition 1.

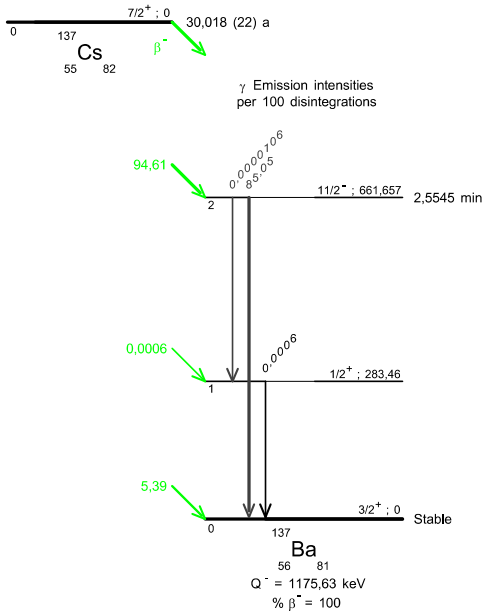

Figure 53: The decay scheme of ^{137}Cs [45].

Decay Mode: EC		Half-Life: (3848 ± 6) d		
Radiation Type		Energy (keV)	Intensity (%)	
Auger-L		3.55	133	6
Auger-K		25.5	13.8	16
ce-K-1		17.18	10.6	4
ce-K-2		43.64	3.43	16
ce-K-3		45.01	45.2	10
ce-L-1		47.45	1.45	20
ce-MNO-1		51.94	0.44	20
ce-L-2		73.91	0.54	10
ce-L-3		75.28	7.37	23
ce-MNOP-3		79.5	2.02	14
ce-K-7		266.87	0.70	6
ce-K-8		320.03	1.31	4
ce-K-9		347.87	0.154	5
ce-L-8		350.30	0.218	7
X-ray L	Σ	4.53	14.5	13
X-ray Kα	Σ	30.85	98.0	14
X-ray Kβ	Σ	35.1	23.0	5
γ		53.16	2.199	22
γ		79.62	2.62	6
γ		81.00	34.06	27
γ		160.61	0.646	8
γ		223.25	0.450	4
γ		276.40	7.164	22
γ		302.85	18.33	6
γ		356.02	62.05	19
γ		383.85	8.94	3

Figure 54: All energies emitted by the ^{133}Ba source with an intensity worth mentioning [44].

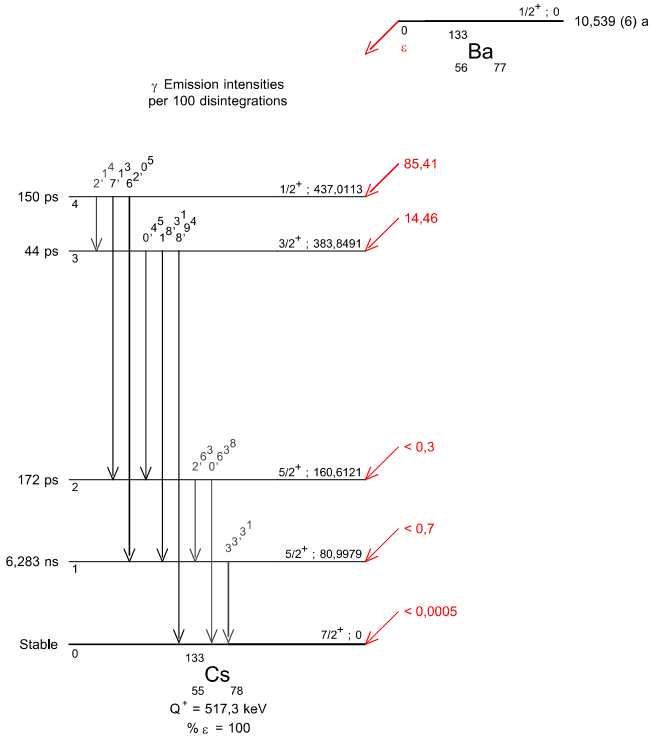

Figure 55: The decay scheme of ^{133}Ba [45].

Decay Mode: β^-		Half-Life: (1925.3 ± 0.4) d			
Radiation Type		**Energy (keV)**		**Intensity (%)**	
Auger-L		0.7	0.9	0.0392	12
Auger-K		6.26	8.32	0.0154	5
β^-max		157.8		« 0.001	--
β^-max		318.22		99.88	3
β^-av		95.77			
β^-max		665.3		« 0.001	--
β^-max		1491.4		0.12	3
β^-av		625.87			
β^-max		2823.9		« 0.001	--
X-ray L	Σ	0.74	0.94	< 0.001	--
X-ray Kα	Σ	7.46	7.48	0.0098	4
X-ray Kβ	Σ	8.26	8.27	0.00136	5
γ		347.14		0.0075	4
γ		826.10		0.0076	8
γ		1173.2		99.85	3
γ		1332.5		99.9826	6
γ		2158.8		0.0012	2
γ		2505.7		« 0.001	--

Figure 56: All energies emitted by the ^{60}Co source with an intensity worth mentioning [44].

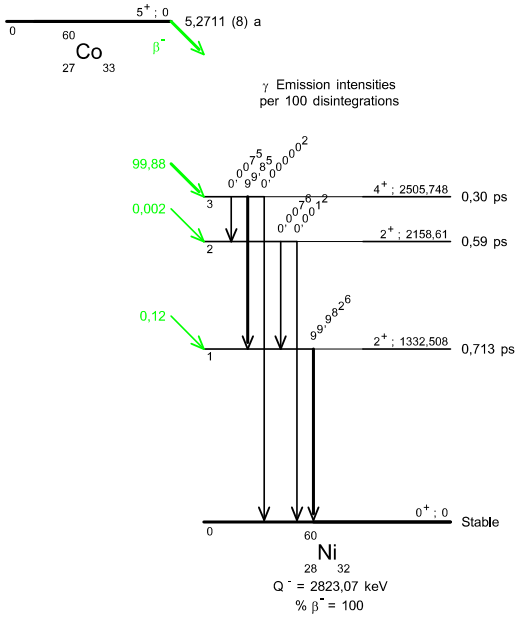

Figure 57: The decay scheme of ^{60}Co [45].

Decay Mode: β^+, EC		Half-Life: (950.5 ± 0.4) d			
Radiation Type		**Energy (keV)**		**Intensity (%)**	
Auger-L		0.02	- 0.05	19.30	20
Auger-K		0.75	- 0.81	9.19	10
β+max		545.6		89.836	11
β+ av		215.5			
β+max		1820.2		0.056	14
β+ av		835.0			
X-ray K	Σ	0.85		0.142	8
γ	Annih.	511.0		179.8	2
γ		1274.5		99.940	14

Figure 58: All energies emitted by the ^{22}Na source with an intensity worth mentioning [44].

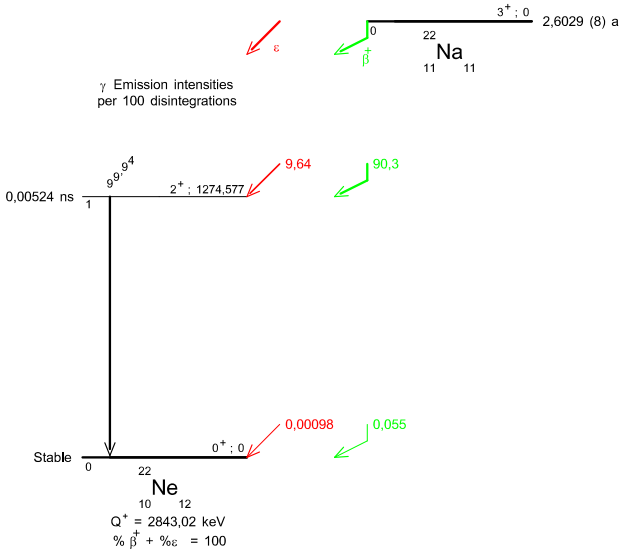

Figure 59: The decay scheme of ^{22}Na [45].

Decay Mode: β^-, α		Half-Life: (8145 ± 80) d		
Radiation Type		**Energy (keV)**	**Intensity (%)**	
Auger-L		8.15	35	4
ce-L-1		30.13	60	4
ce-M-1		42.52	14.0	9
ce-NOP-1		45.58	4.6	3
β^-max		16.5	80	2
β^-max		63.0	20	2
α		3720	« 0.001	--
X-ray L	Σ	12.4	23.4	5
γ		46.54	4.24	5
γ		671.45	1.79	6

Pb-210 with Bi-210 (half-life: 5.013 d) in equilibrium

Figure 60: All energies emitted by the ^{210}Pb source with an intensity worth mentioning [44].

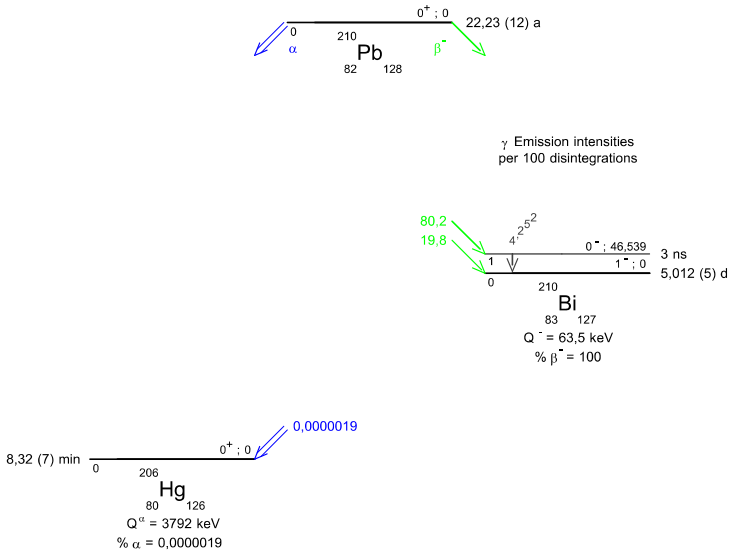

Figure 61: The decay scheme of ^{210}Pb [45].

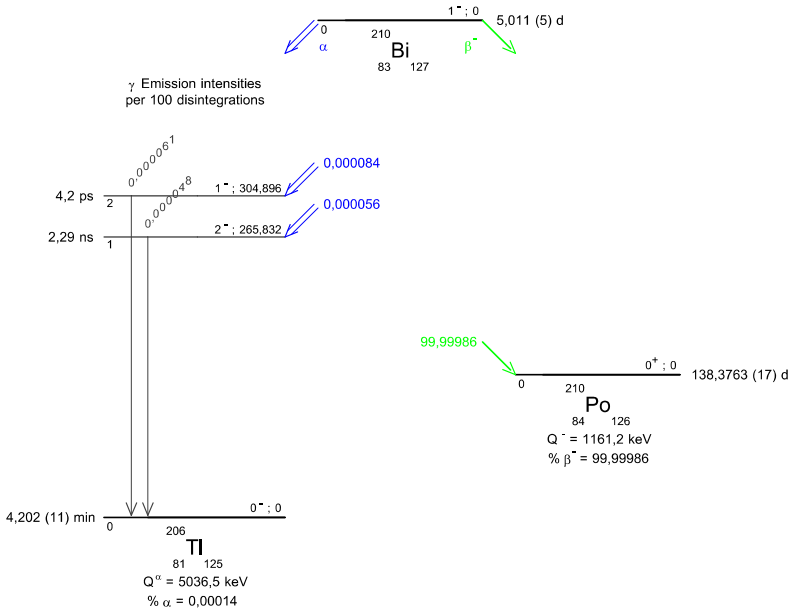

Figure 62: The decay scheme of ^{210}Bi [45].

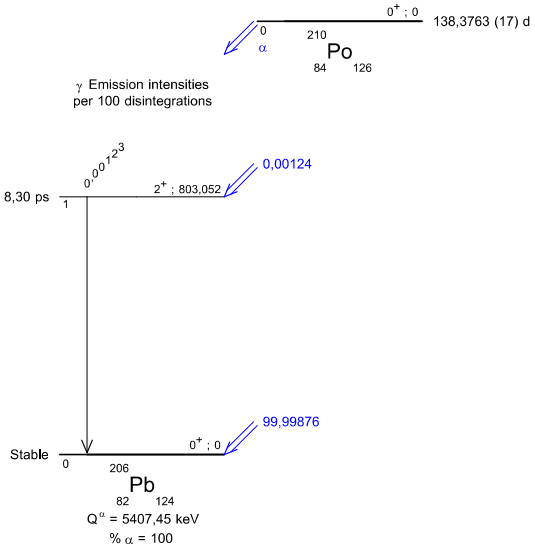

Figure 63: The decay scheme of ^{210}Po [45].

Decay Mode: α		Half-Life: (584400 ± 2600) d		
Radiation Type		**Energy (keV)**	**Intensity (%)**	
Auger-L		8.7	0.97	10
ce-K-1		87.59	0.677	23
ce-L-1		167.94	1.29	4
ce-M-1		181.52	0.345	14
ce-NOP-1		184.90	0.119	7
α		4601.7	5.94	12
α		4784.4	94.05	12
X-ray L	Σ	12.1 - 13.6	14.3	14
X-ray Kα	Σ	74.8 - 83.8	19.5	22
X-ray Kβ	Σ	87.2 - 97.9	5.62	13
γ		186.10	3.51	6
γ	Pb-214	242.0	7.12	11
γ	Pb-214	295.22	18.15	22
γ	Pb-214	351.93	35.1	4
γ	Bi-214	609.31	44.6	5
γ	Bi-214	665.45	1.46	3
γ	Bi-214	768.36	4.76	7
γ	Pb-214	785.96	1.04	2
γ	Bi-214	806.17	1.22	2
γ	Bi-214	934.06	3.07	4
γ	Bi-214	1120.3	14.7	2
γ	Bi-214	1155.2	1.63	2
γ	Bi-214	1238.1	5.78	7
γ	Bi-214	1281.0	1.43	2
γ	Bi-214	1377.7	4.00	6
γ	Bi-214	1401.5	1.27	2
γ	Bi-214	1408.0	2.15	5
γ	Bi-214	1509.2	2.08	5
γ	Bi-214	1661.3	1.15	3
γ	Bi-214	1729.6	2.92	4
γ	Bi-214	1764.5	15.1	3
γ	Bi-214	1847.4	2.11	3
γ	Bi-214	2118.6	1.17	3
γ	Bi-214	2204.2	4.98	12
γ	Bi-214	2447.9	1.55	4

γ-lines with intensity < 1.0 % omitted

X-ray and γ: Ra-226 in equilibrium with daughters up to Bi-214

Figure 64: All energies emitted by the ^{226}Ra source with an intensity worth mentioning [44].

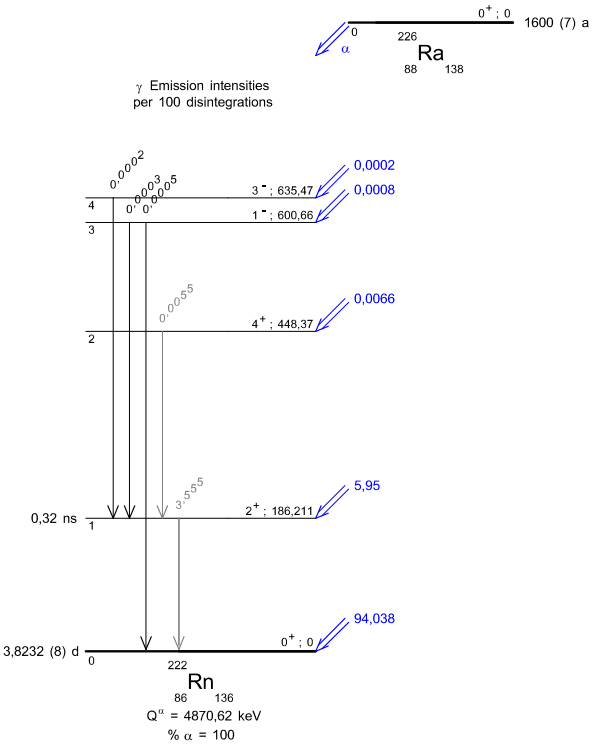

Figure 65: The decay scheme of ^{226}Ra [45]. ^{222}Rn is not stable and ^{226}Ra is just the start of a longer decay chain. To keep the size of this document short the different decay schemes are not shown.

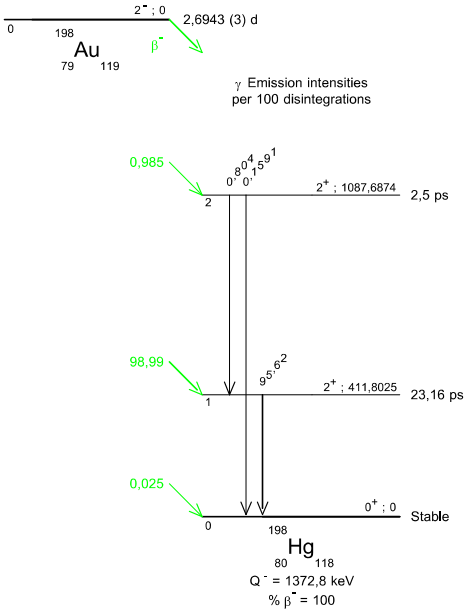

Figure 66: The decay scheme of ^{198}Au [45].

Decay Mode: EC, β^+		Half-Life: (11523 ± 1) d		
Radiation Type		**Energy (keV)**	**Intensity (%)**	
Auger-L		5.2 - 15.7	53.8	14
Auger-K		56.0 - 88.0	2.8	3
ec-K-1		481.7	1.52	2
ec-L-1		553.8 - 557.7	0.440	6
ec-M-1		565.8 - 567.2	0.15	2
ec-K-2		809.8	0.003	1
ec-K-3		975.7	7.03	13
ec-L-3		1047 - 1051	1.84	5
ec-M-3		1059 - 1061	0.54	7
ec-K-4		1682	0.02	1
β+max		806.5	0.012	2
β+av		383.4		
X-ray L	Σ	9.18 - 15.8	33.2	14
X-ray Kα	Σ	74.2	58.19	24
X-ray Kβ	Σ	84.4 - 87.6	16.22	25
γ		328.11	0.00076	8
γ	Annih	511.0	0.0024	4
γ		569.70	97.76	3
γ		897.8	0.131	6
γ		1063.7	74.58	49
γ		1442.2	0.131	2
γ		1770.2	6.87	3

Figure 67: All energies emitted by the ^{207}Bi source with an intensity worth mentioning [44].

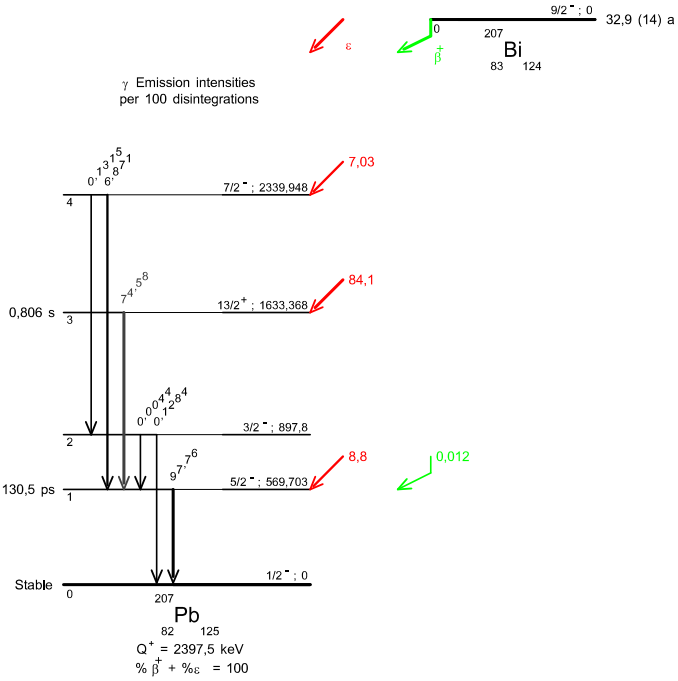

Figure 68: The decay scheme of ^{207}Bi [45].

B Acknowledgments

Special thanks go to the Stefan Meyer Institute for Subatomic Physics of the Austrian Academy of Sciences for providing scintillation equipment and also for giving extensive advice on putting the instruments into operation.

References

[1] R. G. Hamish Robertson. *KATRIN: an experiment to determine the neutrino mass from the beta decay of tritium*. 2013. arXiv: 1307.5486 [physics.ins-det].

[2] P. J. Doe et al. *Project 8: Determining neutrino mass from tritium beta decay using a frequency-based method*. 2013. arXiv: 1309.7093 [nucl-ex].

[3] Benjamin Monreal and Joseph A. Formaggio. "Relativistic cyclotron radiation detection of tritium decay electrons as a new technique for measuring the neutrino mass". In: *Physical Review D* 80.5 (Sept. 2009). ISSN: 1550-2368. DOI: 10.1103/physrevd.80.051301. URL: http://dx.doi.org/10.1103/PhysRevD.80.051301.

[4] Daniel Paulitsch. "Homogenizing the Magnetic Field of a Superconducting Dipole Magnet in Pursuit of Cyclotron Radiation Emission Spectroscopy". project thesis, Projektarbeit. June 2021.

[5] D. Dubbers et al. "A clean, bright, and versatile source of neutron decay products". In: *Nuclear Instruments and Methods in Physics Research Section A: Accelerators, Spectrometers, Detectors and Associated Equipment* 596.2 (Nov. 2008), pp. 238–247. ISSN: 0168-9002. DOI: 10.1016/j.nima.2008.07.157. URL: http://dx.doi.org/10.1016/j.nima.2008.07.157.

[6] Xiangzun Wang et al. "Design of the magnet system of the neutron decay facility PERC". In: *EPJ Web of Conferences* 219 (2019). Ed. by T. Jenke et al., p. 04007. ISSN: 2100-014X. DOI: 10.1051/epjconf/201921904007. URL: http://dx.doi.org/10.1051/epjconf/201921904007.

[7] G Konrad et al. "Neutron Decay with PERC: a Progress Report". In: *Journal of Physics: Conference Series* 340.1 (Feb. 2012), p. 012048. DOI: 10.1088/1742-6596/340/1/012048. URL: https://dx.doi.org/10.1088/1742-6596/340/1/012048.

[8] Ali Ashtari Esfahani et al. "Determining the neutrino mass with cyclotron radiation emission spectroscopy—Project 8". In: *Journal of Physics G: Nuclear and Particle Physics* 44.5 (Mar. 2017), p. 054004. ISSN: 1361-6471. DOI: 10.1088/1361-6471/aa5b4f. URL: http://dx.doi.org/10.1088/1361-6471/aa5b4f.

[9] A. Ashtari Esfahani et al. "Electron radiated power in cyclotron radiation emission spectroscopy experiments". In: *Phys. Rev. C* 99 (5 May 2019), p. 055501. DOI: 10.1103/PhysRevC.99.055501. URL: https://link.aps.org/doi/10.1103/PhysRevC.99.055501.

[10] Bernhard Weigel. Unpublished. Bachelor's thesis. Technical University of Vienna, Technische Universität Wien, 2023.

[11] D. M. Asner et al. "Single-Electron Detection and Spectroscopy via Relativistic Cyclotron Radiation". In: *Physical Review Letters* 114.16 (Apr. 2015). ISSN: 1079-7114. DOI: 10.1103/physrevlett.114.162501. URL: http://dx.doi.org/10.1103/PhysRevLett.114.162501.

[12] Xiangzun Wang. *The Free Neutron beta- Decay: A Powerful Tool for the Investigation in Particle Physics*. en. Figure 5.3. 2013.

[13] *estar stopping-power and range tables for electron*. DOI: https://dx.doi.org/10.18434/T4NC7P. URL: https://physics.nist.gov/PhysRefData/Star/Text/ESTAR.html.

[14] Dominique Drouin et al. “CASINO V2.42—A Fast and Easy-to-use Modeling Tool for Scanning Electron Microscopy and Microanalysis Users”. In: *Scanning* 29.3 (2007), pp. 92–101. DOI: https://doi.org/10.1002/sca.20000. eprint: https://onlinelibrary.wiley.com/doi/pdf/10.1002/sca.20000. URL: https://onlinelibrary.wiley.com/doi/abs/10.1002/sca.20000.

[15] Charlotte Meaker Davisson and Robley D. Evans. “Gamma-Ray Absorption Coefficients”. In: *Rev. Mod. Phys.* 24 (2 Apr. 1952), pp. 79–107. DOI: 10.1103/RevModPhys.24.79. URL: https://link.aps.org/doi/10.1103/RevModPhys.24.79.

[16] Christopher Charles Busby. “The Secondary Photoelectron Effect: Gamma Ray Ionisation Enhancement in Tissues from High Atomic Number Elements”. In: *Use of Gamma Radiation Techniques in Peaceful Applications*. Ed. by Basim A. Almayah. Rijeka: IntechOpen, 2019. Chap. 11. DOI: 10.5772/intechopen.86779. URL: https://doi.org/10.5772/intechopen.86779.

[17] “Radiation Detection and Measurement”. In: *Physics for Radiation Protection*. John Wiley and Sons, Ltd. Chap. 12, pp. 489–522. ISBN: 9783527667062. DOI: https://doi.org/10.1002/9783527667062.ch12. eprint: https://onlinelibrary.wiley.com/doi/pdf/10.1002/9783527667062.ch12. URL: https://onlinelibrary.wiley.com/doi/abs/10.1002/9783527667062.ch12.

[18] Edward Hoffman et al. “Intraoperative Probes and Imaging Probes”. In: *European journal of nuclear medicine* 26 (Sept. 1999), pp. 913–35. DOI: 10.1007/s002590050468.

[19] Gregory Choppin et al. “Chapter 9 - Detection and Measurement Techniques”. In: *Radiochemistry and Nuclear Chemistry (Fourth Edition)*. Ed. by Gregory Choppin et al. Fourth Edition. Oxford: Academic Press, 2013, pp. 239–295. ISBN: 978-0-12-405897-2. DOI: https://doi.org/10.1016/B978-0-12-405897-2.00009-4. URL: https://www.sciencedirect.com/science/article/pii/B9780124058972000094.

[20] Ortec. *Introduction to Charged-Particle Detectors*.

[21] Martin Nikl. “Scintillation detectors for x-rays”. In: 17.4 (Feb. 2006), R37–R54. DOI: 10.1088/0957-0233/17/4/r01. URL: https://doi.org/10.1088/0957-0233/17/4/r01.

[22] G. Bizarri. “Scintillation mechanisms of inorganic materials: From crystal characteristics to scintillation properties”. In: *Journal of Crystal Growth* 312.8 (2010). The 17th American Conference on Crystal Growth and Epitaxy/The 14th US Biennial Workshop on Organometallic Vapor Phase Epitaxy/The 6th International Workshop on Modeling in Crystal Growth, pp. 1213–1215. ISSN: 0022-0248. DOI: https://doi.org/10.1016/j.jcrysgro.2009.12.063. URL: https://www.sciencedirect.com/science/article/pii/S0022024809011609.

[23] G.F. Knoll. *Radiation Detection and Measurement*. Wiley, 2000. ISBN: 9780471073383. URL: https://books.google.at/books?id=HKBVAAAAMAAJ.

[24] Yuan-Chih Lin, Marco Bettinelli, and Maths Karlsson. “Unraveling the Mechanisms of Thermal Quenching of Luminescence in Ce3+-Doped Garnet Phosphors”. In: *Chemistry of Materials* 31.11 (2019), pp. 3851–3862. DOI: 10.1021/acs.chemmater.8b05300. eprint: https://doi.org/10.1021/acs.chemmater.8b05300. URL: https://doi.org/10.1021/acs.chemmater.8b05300.

[25] L. Gruber et al. "Over saturation behavior of SiPMs at high photon exposure". In: *Nuclear Instruments and Methods in Physics Research Section A: Accelerators, Spectrometers, Detectors and Associated Equipment* 737 (2014), pp. 11–18. ISSN: 0168-9002. DOI: https://doi.org/10.1016/j.nima.2013.11.013. URL: https://www.sciencedirect.com/science/article/pii/S0168900213015520.

[26] *SiPM Linearity*. Hamamatsu Photonics K.K. URL: https://www.hamamatsu.com/eu/en/resources/interactive-tools/mppc-sipm-linearity.html.

[27] Projektass. Dipl.-Ing. Andreas Doblhammer. *CREScent*.

[28] P. A. Cutler et al. "Scintillation Non-Proportionality of Lutetium- and Yttrium-Based Silicates and Aluminates". In: *IEEE Transactions on Nuclear Science* 56.3 (2009), pp. 915–919. DOI: 10.1109/TNS.2009.2016421.

[29] P. Dorenbos and C. W. E. Van Eijk, eds. *Proceedings, International Conference on Inorganic Scintillators and their Applications (SCINT 95): Delft, The Netherlands, August 28-September 1, 1995*. Delft: Delft University Press, 1996.

[30] Marcin Balcerzyk et al. "YSO, LSO, GSO and LGSO. a study of energy resolution and nonproportionality". In: *Nuclear Science, IEEE Transactions on* 47 (Sept. 2000), pp. 1319–1323. DOI: 10.1109/23.872971.

[31] J.T.M. de Haas, P. Dorenbos, and C.W.E. van Eijk. "Measuring the absolute light yield of scintillators". In: *Nuclear Instruments and Methods in Physics Research Section A: Accelerators, Spectrometers, Detectors and Associated Equipment* 537.1 (2005). Proceedings of the 7th International Conference on Inorganic Scintillators and their Use in Scientific adn Industrial Applications, pp. 97–100. ISSN: 0168-9002. DOI: https://doi.org/10.1016/j.nima.2004.07.243. URL: https://www.sciencedirect.com/science/article/pii/S0168900204017917.

[32] M. J. Weber and R. R. Monchamp. "Luminescence of Bi4 Ge3 O12 : Spectral and decay properties". In: *Journal of Applied Physics* 44.12 (1973), pp. 5495–5499. DOI: 10.1063/1.1662183. eprint: https://doi.org/10.1063/1.1662183. URL: https://doi.org/10.1063/1.1662183.

[33] Eiji Sakai. "Recent Measurements on Scintillator-Photodetector Systems". In: *IEEE Transactions on Nuclear Science* 34.1 (1987), pp. 418–422. DOI: 10.1109/TNS.1987.4337375.

[34] Saint-Gobain Crystals C. M. Rozsa. *Efficiency Calculations for Selected Scintillators*. Efficiency Calculations Brochure, Saint-Gobain Crystals,www.crystals.saint-gobain.com. URL: https://www.crystals.saint-gobain.com/.

[35] F. Ajzenberg-Selove. "Energy levels of light nuclei A = 13–15". In: *Nuclear Physics A* 523.1 (1991), pp. 1–196. ISSN: 0375-9474. DOI: https://doi.org/10.1016/0375-9474(91)90446-D. URL: https://www.sciencedirect.com/science/article/pii/037594749190446D.

[36] S.K. Basu and E.A. Mccutchan. "Nuclear Data Sheets for A = 90". In: *Nuclear Data Sheets* 165 (2020), pp. 1–329. ISSN: 0090-3752. DOI: https://doi.org/10.1016/j.nds.2020.04.001. URL: https://www.sciencedirect.com/science/article/pii/S0090375220300090.

[37] C.W. Reich. "Nuclear Data Sheets for A = 159". In: *Nuclear Data Sheets* 113.1 (2012), pp. 157–363. ISSN: 0090-3752. DOI: https://doi.org/10.1016/j.nds.2012.01.002. URL: https://www.sciencedirect.com/science/article/pii/S0090375212000038.

[38] F.G. Kondev and S. Lalkovski. "Nuclear Data Sheets for A = 207". In: *Nuclear Data Sheets* 112.3 (2011), pp. 707–853. ISSN: 0090-3752. DOI: https://doi.org/10.1016/j.nds.2011.02.002. URL: https://www.sciencedirect.com/science/article/pii/S0090375211000111.

[39] J. Byrne, F. Shaikh, and T.J.L. McComb. "Magnetic field dependence of the energy resolution of silicon surface-barrier detectors". In: *Nuclear Instruments and Methods* 122 (1974), pp. 347–350. ISSN: 0029-554X. DOI: https://doi.org/10.1016/0029-554X(74)90498-4. URL: https://www.sciencedirect.com/science/article/pii/0029554X74904984.

[40] C. L. Melcher et al. "Temperature Dependence of Fluorescence Decay Time and Emission Spectrum of Bismuth Germanate". In: *IEEE Transactions on Nuclear Science* 32.1 (1985), pp. 529–532. DOI: 10.1109/TNS.1985.4336887.

[41] Adam Nepomuk Otte et al. "Characterization of three high efficiency and blue sensitive silicon photomultipliers". In: *Nuclear Instruments and Methods in Physics Research Section A: Accelerators, Spectrometers, Detectors and Associated Equipment* 846 (Feb. 2017), pp. 106–125. ISSN: 0168-9002. DOI: 10.1016/j.nima.2016.09.053. URL: http://dx.doi.org/10.1016/j.nima.2016.09.053.

[42] M.-A. Verdier et al. "Scintillation properties of $Bi_4Ge_3O_{12}$ down to 3 K under γ rays". In: *Phys. Rev. B* 84 (21 Dec. 2011), p. 214306. DOI: 10.1103/PhysRevB.84.214306. URL: https://link.aps.org/doi/10.1103/PhysRevB.84.214306.

[43] N. Tsuchida et al. "Temperature dependence of gamma-ray excited scintillation time profile and light yield of GSO, YSO, YAP and BGO". In: *Nucl. Instrum. Meth. A* 385 (1997), pp. 290–298. DOI: 10.1016/S0168-9002(97)84721-3.

[44] *Recommended Nuclear Decay Data*. Eckert und Ziegler Strahlen- und Medizintechnik AG. URL: https://www.ezag.com/home/.

[45] M.-M. Bé et al. *Table of Radionuclides*. Vol. 8. Monographie BIPM-5. Pavillon de Breteuil, F-92310 Sèvres, France: Bureau International des Poids et Mesures, 2016. ISBN: 978-92-822-2264-5. URL: http://www.bipm.org/utils/common/pdf/monographieRI/Monographie_BIPM-5_Tables_Vol8.pdf.